

CONTROL OF NANOWIRE GROWTH BY DROPLET DYNAMICS
WITH OPTICAL APPLICATIONS

CONTROL OF NANOWIRE GROWTH BY DROPLET DYNAMICS
WITH OPTICAL APPLICATIONS

By D. PAIGE WILSON, HBSc.

A Thesis Submitted to the School of Graduate Studies in Partial Fulfilment of the
Requirements for the Degree Doctor of Philosophy

McMaster University © by D. Paige Wilson, 2022

McMaster University DOCTOR OF PHILOSOPHY (2022) Hamilton, ON (Engineering Physics)

TITLE: Control of Nanowire Growth by Droplet Dynamics with Optical Applications
AUTHOR: D. Paige Wilson, HBSc. (University of Toronto) SUPERVISOR: Dr. Ray R. LaPierre
NUMBER OF PAGES: 185

Lay Abstract

This thesis seeks to understand the growth processes behind self-catalyzed nanowire growth. Nanowires (NWs) are very thin, vertical columns of semiconducting material. Self-catalyzed growth is a method of producing these structures that uses a droplet at the top of the structure to add material to the structure over time. These structures have numerous applications. This thesis focuses on solar cells and distributed Bragg reflectors (DBRs). Experiments show how control over the droplet can improve NW yield and give significant control of the NW diameter. These experiments are supported by mathematical models. Control over the diameter is important for the applications discussed. Using numerical simulations, it is shown how control over the diameter of the structure can lead to improvements in light absorption in NW solar cells. Additionally, periodic changes to the diameter can be used to create novel NW structures such as DBRs, which is a promising new application.

Abstract

Self-catalyzed GaAs nanowires (NWs) are grown epitaxially on Si(111) substrates using molecular beam epitaxy (MBE). The dynamics of the droplet are examined to improve NW yield and to control NW morphology. Control and understanding of the NW diameter via droplet dynamics is applied to NW photovoltaics and to novel corrugated NW distributed Bragg reflectors (DBRs). At the beginning of the MBE growth, a Ga pre-deposition step, between 0 s and 500 s in duration, is introduced to improve the yield of the NW arrays. The effect of the pre-deposition time was examined for five different hole diameters and yield was increased to nearly 100% for the appropriate combination of hole diameter and pre-deposition time.

Two models were used to model the NW growth progression under different atomic flux ratios. The first model considers the contributions from direct and diffusion fluxes to the droplet and solves coupled equations for the droplet contact angle and the NW radius. The second model treats the contact angle as constant. Both models explained the accompanying experimental observations. Both models could be used to model future NW growths and the choice between the two would depend on the availability of contact angle data and whether the crystal phase must be considered.

Absorption in NWs is determined by the diameter and the HE_{1n} modes. The effectiveness of a linearly tapered inverted conical NW is demonstrated using finite element simulations. The photocurrent of an optimized inverted conical NW array is found and shown to be similar to that achieved by optical nanocones and nanowires. Diameter modulations can also be introduced into NW structures periodically to produce corrugated

NW distributed Bragg reflectors (DBRs). The tunability of the reflectance peaks is demonstrated and explained by changes to the effective refractive index of the structure.

Acknowledgements

I would like to extend my sincerest thanks to all the people who made this thesis possible. There were certainly times along the way when reaching this point seemed incredibly daunting and it was only with the continued support of these people that I was able to move forward.

Firstly, I would like to thank my research supervisor, Dr. Ray LaPierre for his patience and encouragement throughout my PhD. It was with his reassurance that I was able to stay on track, set, and accomplish goals for research. I'd also like to thank the members of my committee Dr. Adrian Kitai and Dr. Rafael Kleiman for their helpful comments on my work. A special thank you goes to Dr. Vladimir Dubrovskii and his research group for not only being excellent collaborators but also incredibly welcoming when I was living in St. Petersburg.

This work would not have been possible without the amazing support from the staff at McMaster's Centre for Emerging Device Technology. Shahram Tavakoli performed all MBE growths and provided tremendous insight and advice on the growth process itself. I am grateful to Doris Stevanovic for training me on equipment and for running such a professional cleanroom. I am incredibly grateful to staff at the Canadian Centre for Electron Microscopy, Chris Butcher for training me on the SEM and Carmen Andrei for her patience and support in training me to use the TEM. I am also thankful for Alex Tsukernik at the Toronto Nanofabrication Centre for his assistance with the EBL portions of the sample fabrication.

The past and present members of the LaPierre research group have been a great source of support throughout this process and many remain my friends today. I'd like to thank Aziz Rhaman, Brendan Wood, Mitch Robson, Paul Kuyanov, Simon McNamee, Azadeh Akhtari Zavareh, Devan Wagner, Nebile Isik-Goktas, Curtis Goosney, and Amanda Thomas for their support in getting me started, training me on equipment, sharing their ideas and knowledge, and just generally being amazing to work alongside.

I'd also like to thank NSERC CREATE TOP-SET for providing funding for this project and a great training program for young scientists. I'd also like to thank Ontario Graduate Scholarships and the Department of Engineering Physics for additional funding.

To my close friends and family, I have not enough words to fully describe my love and gratitude for you all. Thank you for showing me how proud you were of me when I could not find it in myself and for never doubting my abilities and my capacity to succeed. To my parents, I am grateful to have two amazing role models in my life who have shown me what a successful engineer and scientist look like. I am thankful to my siblings for providing me with laughter and an outlet to talk about anything other than my research when I needed it. Thank you to my grandmother for her continued love and support and for reminding me that I come from generations of intelligent, determined women. To all my friends, thank you for being there for me, keeping me sane, and showing me that I am not alone.

I could not have reached this point without the support of so many people and for that I am humbled.

To Mom, Dad, my friends, and my family

Table of Contents

Lay Abstract	iii
Abstract.....	iv
Acknowledgements	vi
Table of Figures	xii
Symbols and Abbreviations.....	xx
Declaration of Academic Achievement.....	xxiii
1. Introduction	1
1.1. Nanowires	1
1.2. Nanowire Applications	4
1.3. Thesis Statement	7
1.4. References	9
2. Theory	16
2.2. Nanowire Nucleation.....	16
2.3. Nanowire Growth	20
2.4. Nanowire Optical Properties.....	24
2.5. References	29
3. Experimental and Simulation Methods.....	36
3.1. Sample Preparation	36
3.2. Molecular Beam Epitaxy.....	38
3.3. Characterization	40
3.3.1. Scanning Electron Microscopy	40
3.3.2. Transmission Electron Microscopy	41
3.4. Finite Element Method.....	42
3.5. References	45
4. Effect of Ga Pre-Deposition on Nanowire Yield and Diameter	47

4.1.	Summary	47
4.2.	Introduction	48
4.3.	Experimental Details	49
4.4.	Results and Discussion.....	51
4.4.1.	Effect of Ga Pre-Deposition on Yield	51
4.4.2.	Effect of Ga Pre-deposition on Morphology.....	54
4.4.3.	Model	57
4.5.	Conclusions.....	61
4.6.	Supplementary Materials.....	62
4.7.	References	64
5.	Modeling the Nanowire Diameter Progression During Growth.....	68
5.1.	Summary	68
5.2.	Introduction	69
5.3.	Model	71
5.4.	Results and Discussion.....	76
5.5.	References	83
6.	MBE Grown Photovoltaic Light Funnel Using Droplet Dynamics	88
6.1.	Summary	88
6.2.	Introduction	89
6.3.	Experimental Details.....	92
6.4.	Results	93
6.4.1.	NW Growth.....	93
6.4.2.	Light Absorption Model.....	103
6.5.	Conclusions.....	107
6.6.	References	108
7.	Optimizing Tapered Nanowires for Photovoltaic Applications	115

7.1.	Summary	115
7.2.	Introduction	116
7.3.	Methods.....	119
7.4.	Results and Discussion.....	121
7.5.	Conclusions.....	129
7.6.	Supplementary Materials.....	130
7.7.	References	139
8.	Corrugated Nanowires for Distributed Bragg Reflectors	147
8.1.	Summary	147
8.2.	Introduction	147
8.3.	Methods.....	150
8.4.	Results and Discussion.....	152
8.5.	Conclusions.....	160
8.6.	References	161
9.	Conclusions and Future Work	166
9.1.	Thesis Summary	166
9.2.	Future Work	169
9.2.1.	Conical NW Photovoltaics.....	169
9.2.2.	NW Modelling and Databases	171
9.2.3.	Corrugated NWs for DBRs, FP Cavities, and VCSELs	172
9.3.	References	173
10.	Appendix	174
10.1.	Setting Up COMSOL 5.3A Optical Models for Periodic NW Arrays	174
10.2.	Setting up a batch file.....	183
10.3.	Setting power	184
10.4.	References	184

Table of Figures

Figure 1.1. (a) A schematic of a small area of a NW array showing hexagonally faceted GaAs NWs (the vertical is in the $\langle 111 \rangle$ direction) on a Si(111) substrate with a SiO_x mask. (b) An SEM image of a NW array with 600 nm pitch. Scale bar is 1 μm 2

Figure 2.1. A heterostructure consisting of a substrate and epitaxial layer with different lattice constants. The strain is relaxed in (a) plastically, through the formation of a misfit dislocation and in (b) elastically..... 19

Figure 2.2. Possible adatom fluxes for NWs in an MBE chamber. The MBE supplies a direct flux of material at an angle θ with respect to the vertical. Neighboring NWs can shadow the substrate and sidewalls from this direct flux. The group III adatoms can diffuse along both the substrate and sidewalls of the NW and collect in the droplet reservoir at the top of the NW. Arrows show the direction of diffusion as upwards, towards the droplet, but the diffusion occurs in multiple directions. Group III atoms may even diffuse into or out of the droplet. Group V adatoms tend not to diffuse and only interact if they encounter a group III atom either in the droplet reservoir or on the NW sidewalls for VS growth. The inset shows the geometry at the top of the NW where D is the diameter, β is the contact angle with respect to the horizontal, and θ is the beam angle with respect to the vertical. 23

Figure 2.3: (a) Solutions of the eigenvalue equation for the HE_{11} and HE_{12} modes as the intercepts of the left- and right-hand sides of the eigenvalue equation for $V = 8$. (b) The normalized propagation constant, $b = 1 - u^2/V^2$, versus V for the HE_{11} and HE_{12} modes. The limits of the refractive index, in the core and in the cladding, are indicated on the right-hand side. 26

Figure 2.4. The electric field vectors in the transverse plane for (a) the HE_{11} mode and (b) the HE_{12} mode..... 28

- Figure 3.1.** Wafer preparation prior to MBE growth. Preparation begins with (a) a clean, Si(111) wafer, followed by (b) growing a SiO_x oxide layer by PE-CVD. The wafer is then spin coated with a positive e-beam resist and (c) patterned with a series of dots via EBL before (d) being developed to remove the resist from the patterned regions. Lastly, (e) holes are etched into the oxide mask via RIE and the remaining resist is removed. 37
- Figure 3.2.** SEM images of etched holes in the oxide layer with a pitch of 360 nm where (a) was given a low e-beam dosage and (b) a high dose. Pinhole defects are also visible in the oxide layer. The scale bar is 100 nm. 38
- Figure 3.3.** (a) The MBE chamber at McMaster University’s Centre for Emerging Device Technologies. (b) A labelled schematic of the same system. 39
- Figure 3.4.** Basic schematic of the simulation geometry, showing perfectly matched layers (PMLs) at the top and bottom of the simulation geometry. Period boundary conditions are specified in pairs labelled (1) and (2) and apply to the outer sides. A port boundary is placed above the NW but below the uppermost PML and directs a plane wave downwards on the NW. The pitch, P , defines the size of the unit cell. 44
- Figure 4.1.** 20° tilted SEM images of NWs with (a, d) 0 s, (b, e) 250 s, and (c, f) 500 s of Ga pre-deposition. Pattern pitch was 520 nm and hole diameter was (a-c) 57 nm and (d-f) 101 nm. Scale bars are 1 μm 51
- Figure 5.1.** Experimental data (symbols) and best fit (lines) of the contact angle (upper panel) and radius (lower panel) dynamics in a single self-catalyzed GaAs NW. The fit is obtained using the parameters given in Table 5.1 to find the solution. The alternating blocks of white and shaded background indicate changes in the V/III ratio as shown in table 5.1. The values of β_{max} and β_{min} are 137° and 100° , respectively, as indicated by dashed lines. The values of φ_w and φ_n are -8° and 55° , respectively, as measured from the images of Ref. [5.19]. The diagrams in the bottom panel show the NW shape and crystal phase. Transitions from the WZ to the ZB phase occur when the contact angle

becomes larger than $\beta_c = 125^\circ$, with vertical NW sidewalls and truncated top above this value, or smaller than $\beta_{min} = 100^\circ$, with tapered NW morphology and flat top below this value [5.19]. 75

Figure 5.2. TEM images of a GaAs NW with Ga droplet on top corresponding to section B where the droplet contact angle gradually decreases under high As/Ga flux ratio. (a) Large droplet with $\beta > 125^\circ$, yielding a truncated growth interface and pure ZB phase. (b) Small droplet with β approaching 100° , yielding planar growth interface with vertical sidewalls. The crystal phase is pure WZ far below the droplet, with stacking faults appearing immediately below the droplet near the transition from WZ to ZB phase. 77

Figure 5.3. The solutions from solving the equations with χ dependent on β as compared to using constant χ values. The solution shown for variable χ is the same as that in Fig. 5.1. Both solutions use the parameters given in Table 3. The constant value of χ_3 and χ_5 were set to 0.808 and 1.132, respectively, corresponding to $\beta = 110^\circ$. We choose 110° because it falls in the middle of the range of contact angles present in this study. While the plots are similar for β , small differences compound as L increases which results in the plots of R diverging from one another. 79

Figure 5.4. The relationship between the inverted V/III ratios numerically determined for the solved parameters and the V/III flux ratios as presented in Ref. [19]. Both the V/III ratios and the V/III ratios with reverse diffusion are shown. 81

Figure 6.1. (a) 20° tilted SEM image of NW array from sample A with a V/III flux ratio of 2 throughout growth. Pitch is 520 nm. Scale bar is 1 μm . (b) 30° tilted SEM image of NW array from sample B with a V/III flux ratio that was reduced from 2 to 1 after 25 min of GaP stem growth. Pitch is 1000 nm. Scale bar is 1 μm . Inset shows a magnified cross-sectional SEM view with a scale bar of 100 nm. (c) 30° tilted SEM image of NW array from sample C with a V/III flux ratio that was reduced from 2 to 1 after 10 min of GaP stem growth. Pitch is 520 nm. Scale bar is 1 μm 95

Figure 6.2. STEM image of NW from (a) sample A and (b) sample B, with three marker layers indicated by arrows. Scale bars are 50 nm.	96
Figure 6.3. (a) P and As flux for sample B. The red dashed line indicates the time when the V/III flux ratio was changed from 2 to 1. (b) Progression of parameter A with time. (c) Progression of parameter B with time.....	101
Figure 6.4. Model prediction of the NW diameter versus time. The red dashed line indicates the time when the V/III flux ratio was changed from 2 to 1.	102
Figure 6.5. Theoretical absorptance in straight NWs (solid lines) and tapered NWs (dashed lines) due to consecutive 500 nm segments. ‘500 nm’ represents the segment at the top of the NW and ‘2000 nm’ represents the segment at the base of the NW. The total absorptance and reflectance is also indicated.	105
Figure 6.6. Generation rate in (a) straight and (b) inverse-tapered NWs.....	106
Figure 7.1. (a-c) Definition of NW morphologies. (b) Schematic of source, reflection and transmission planes.....	120
Figure 7.2. Absorptance spectra for NWs with a base diameter of 100 nm and a length of 2000 nm. The NW top diameter is given above each plot. Insets in the 50 nm and 290 nm panels illustrate a typical NW profile. The spectra have been subdivided into the contributions to absorptance from incremental segments of 500 nm length where A is the top 500 nm and D is the bottom 500 nm. The absorptance spectrum of a thin film is also shown.	123
Figure 7.3. (a) The total reflectance and (b) total transmittance versus top diameter for each of the NW morphologies, as well as a thin film. The legend indicates the NW base diameter. Dashed lines represent NWs with length of 1000 nm and solid lines indicate those with length of 2000 nm.	125
Figure 7.4. Photocurrent versus top diameter generated in each of the NW morphologies. The legend indicates the NW base diameter. Dashed lines represent NWs with length of 1000 nm and solid lines indicate those with length of 2000 nm. .	128
Figure 7.5. Electric field profiles for a nearly cylindrical nanowire with 90 nm top diameter, 100 nm base diameter, and 2000 nm length. The exciting wavelength	

is 525 nm. The norm of the electric field is shown in (a) for a planar slice at a depth of 250 nm from the top of the nanowire as indicated by the arrow in (e). Subplots (b) and (e) show the E_z component of the electric field while (c) and (d) show E_x and E_y , respectively. The arrow plots show the direction of the field in the plane. The red dotted circle represents the edge of the nanowire at the given depth..... 130

Figure 7.6. Electric field profiles for a nearly cylindrical nanowire with 170 nm top diameter, 100 nm base diameter, and 2000 nm length. The exciting wavelength is 455 nm. The norm of the electric field is shown in (a) for a planar slice at a depth of 400 nm from the top of the nanowire as indicated by the arrow in (e). Subplots (b) and (e) show the E_z component of the electric field while (c) and (d) show E_x and E_y respectively. The arrow plots show the direction of the field in the plane. The red dotted circle represents the edge of the nanowire at the given depth..... 131

Figure 7.7. Absorptance spectra for NWs with a base diameter of 50 nm and a length of 2000 nm. The NW top diameter is given above each plot. The spectra have been subdivided into the contributions to absorptance from incremental segments of 500 nm length where A is the top 500 nm and D is the bottom 500 nm. The absorptance spectrum of a thin film is also shown..... 132

Figure 7.8. Absorptance spectra for NWs with a base diameter of 200 nm and a length of 2000 nm. The NW top diameter is given above each plot. The spectra have been subdivided into the contributions to absorptance from incremental segments of 500 nm length where A is the top 500 nm and D is the bottom 500 nm. The absorptance spectrum of a thin film is also shown..... 133

Figure 7.9. Absorptance spectra for NWs with a base diameter of 50 nm and a length of 1000 nm. The NW top diameter is given above each plot. The spectra have been subdivided into the contributions to absorptance from incremental segments of 500 nm length where A is the top 500 nm and B is the bottom 500 nm. The absorptance spectrum of a thin film is also shown..... 134

Figure 7.10. Absorptance spectra for NWs with a base diameter of 100 nm and a length of 1000 nm. The NW top diameter is given above each plot. The spectra have been subdivided into the contributions to absorptance from incremental segments of 500 nm length where A is the top 500 nm and B is the bottom 500 nm. The absorptance spectrum of a thin film is also shown..... 135

Figure 7.11. Absorptance spectra for NWs with a base diameter of 200 nm and a length of 1000 nm. The NW top diameter is given above each plot. The spectra have been subdivided into the contributions to absorptance from incremental segments of 500 nm length where A is the top 500 nm and B is the bottom 500 nm. The absorptance spectrum of a thin film is also shown..... 136

Figure 7.12. Absorptance for inverted cone NWs (base diameter of 50 nm and 100 nm, and top diameter of 210 nm), a cone NW (base diameter of 200 nm and a top diameter of 110 nm), and a 2000 nm thick film (according to the Beer-Lambert model and assuming perfect anti-reflection coating)..... 137

Figure 7.13. The electric field norm at 735 nm for (a) a NW with 210 nm top diameter and 50 nm base diameter, (b) a NW with 210 nm top diameter and 100 nm base diameter, (c) a cylindrical NW of 210 nm diameter, (d) a thin film. In (d) the reflectance is very large resulting in a small field inside the film. No modes are excited in (d). In (a), (b), and (c), various HE_{1n} modes are excited. The fields within the NW change as the diameter changes, concentrating in different locations. The absorptance in the NWs in (a), (b), and (c) are 0.83, 0.98, and 0.81 while the reflectance is 0.14, 0.02, and 0.06, respectively. The thickness is 2000 nm in all cases. 138

Figure 8.1. Geometry of the corrugated NWs..... 151

Figure 8.2. Reflectance from arrays of cylindrical NWs with pitches of 400 nm and 800 nm and diameter of 165 nm (solid lines) or 245 nm (dashed lines.) 153

Figure 8.3. Reflectance for corrugated NW DBRs with an inner diameter of 165 nm and corrugation depths of 5 nm, 10 nm, 25 nm and 40 nm. The period, Λ , is 400

	nm and repeats 10 times for a total corrugated length of 4000 nm. Three pitches are shown: (a) 400 nm, (b) 600 nm, and (c) 800 nm.	155
Figure 8.4.	Electric field norm for NWs with $P = 400$ nm and wavelength corresponding to maximum reflectance λ_B as shown in Figure 8.3 (a). The corrugation depth is (a) 5 nm, (b) 10 nm, (c) 25 nm, and (d) 40 nm. The incident wavelength is (a) 805 nm, (b) 825 nm, (c) 865 nm, and (d) 900 nm.	156
Figure 8.5.	The reflectance spectra of a corrugated NW DBR with 3, 5, or 10 periods. The period length is $\Lambda = 400$ nm. The pitch is 400 nm and the corrugation depth is (a) 5 nm and (b) 40 nm.	156
Figure 8.6.	Reflectance spectrum for an array of corrugated NWs with 800 nm pitch, 165 nm inner diameter, and 5 nm corrugation depth. The period, Λ , of the corrugation is given in the legend.	158
Figure 8.7.	The transverse field in a corrugated NW at an incident wavelength of 915 nm with inner diameter $d_1 = 165$ nm, period $\Lambda = 700$ nm, and corrugation depth $h = 5$ nm. Field vectors correspond to the transverse field components E_x and E_y	158
Figure 8.8.	(a) The E_y field in the yz plane at an incident wavelength of 915 nm in a corrugated NW with $d_1 = 165$ nm, $\Lambda = 700$ nm, and $h = 5$ nm. (b) The norm of the transverse field down the centre line of the NW.	159
Figure 8.9.	The reflectance (solid lines) and absorptance (dashed lines) spectra for corrugated NW arrays with a pitch of 400 nm, inner diameter of 165 nm, period Λ of 400 nm, 10 periods, and non-zero imaginary component of the complex refractive index. Corrugation depth is given in the legend.	160
Figure 9.1.	(a) 20° tilted SEM images of tapered NW arrays grown without a shell layer. Inset shows a higher magnification and is tilted 30° . (b) 20° tilted SEM images of NW arrays grown with the same core parameters as (a) but with the addition of 15 min of VS $\text{Al}_{0.8}\text{Ga}_{0.2}\text{As}$ shell growth after the core has been grown. Pitch is 1000 nm. Scale bars are 100 nm.	170

Figure 10.1. The (a) unit cell geometry and (b) mesh used to simulate an array of tapered NWs in COMSOL Multiphysics 5.3A. The NW and substrate have been highlighted in (a). Certain faces have been hidden in (b) in order to see the dense mesh on the NW domain more clearly. 180

Symbols and Abbreviations

Symbol	Definition	Chapter Reference
A	absorptance	3
a	core radius of optical fiber	2
α	beam angle	4, 5, 6
$\alpha(R)$	fraction of atoms available for growth at radius R	4
\vec{B}	magnetic induction	2
b	normalized propagation constant	2
β	droplet contact angle	2, 5, 9
β	propagation constant	2, 8
C	concentration factor	8
$\chi_{3,5}$	geometric function for group III and V materials	5
D, d	diameter	2, 8
\vec{D}	electric field displacement	2
\vec{E}	electric field	2, 3, 7, 8
e	fundamental charge	7
ϵ	permittivity	2, 3, 7
\vec{H}	magnetic field	2
h	corrugation depth	8
\hbar	reduced Plank's constant	7
H_{hole}	hole depth	4
\vec{j}	electric current density	2
J	photocurrent density	3, 7
J_3	direct flux of group III material	6
$J_{3,5}^{eff}$	effective flux of group III or V material	6
J_q	Bessel function of the first kind	2
k	wavevector	2, 3
k_B	Boltzmann constant	6
K_q	modified Bessel function of the second kind	2
κ	extinction coefficient	2, 3, 7

L	length	5
l	corrugated section length	8
Λ	corrugation period	8
λ	wavelength	2, 3, 8
λ	diffusion length	4, 5, 6
m	Bragg order	8
μ	magnetic permeability	2
$\mu_{3,5}$	chemical potential	6
$N_{3,5}$	number of group III or V atoms in droplet	5, 6
n	refractive index	2, 3, 7, 8
$n_{s,l,f}$	group III adatom concentrations on the substrate, liquid phase, or sidewall facers	5
$\Omega_{L,S}$	elementary volume per atom (atomic pair) in liquid (solid)	5, 6
ω	angular frequency	2
$\phi_{n,w}$	narrowing or widening facet angle	5
θ	beam angle	2
$\theta_{l,s}$	group III activity in liquid and on sidewalls	6
θ_{sf}, θ_{lf}	ratio between adatom concentrations (substrate/sidewall and liquid/sidewall)	5
u	normalized transverse phase constant	2
v	deposition rate of Ga	4
$v_{3,5}$	direct flux of group III or V material	5
v_l	reverse diffusion flux	5
V	V parameter	2
V	volume	3, 4, 7, 8
P	pitch	3, 4, 7, 8
$P_{ref,inc}$	reflected or incident power	7
R	reflectance	3
R	radius	4, 5, 6
ρ	free charge	2
σ	conductivity	2
T	transmittance	3
T	temperature	6
t	time	2, 4, 6

	w	normalized transverse attenuation coefficient	2
	y	yield	4
Abbreviation	Definition		
	BHF	buffered hydrofluoric	
	DBR	distributed Bragg reflector	
	DF	dark field	
	EBL	electron beam lithography	
	FEM	finite element method	
	FP	Fabry-Perot	
	GS-MBE	gas source molecular beam epitaxy	
	HAADF	high angle annular dark field	
	IPA	isopropyl alcohol	
	LED	light emitting diode	
	LMR	leaky mode resonance	
	MBE	molecular beam epitaxy	
	NW	nanowire	
	PECE	predict-evaluate-correct-evaluate	
	PE-CVD	plasma enhanced chemical vapor deposition	
	PML	perfectly matched layer	
	PV	photovoltaic	
	RIE	reactive ion etching	
	SEM	scanning electron microscopy	
	SOP	standard operating procedure	
	STEM	scanning transmission electron microscopy	
	TEM	transmission electron microscopy	
	VCSEL	vertical cavity surface emitting laser	
	VLS	vapor-liquid-solid	
	VS	vapor-solid	
	VSVO	variable-step variable-order	
	WZ	wurtzite	
	ZB	zinc-blende	

Declaration of Academic Achievement

The work presented in this thesis provides a thorough description of self-catalyzed nanowire (NW) growth and control over the NW diameter. It describes how to optimize the diameter and yield to achieve high performance of NW photovoltaics and presents novel NW structures which are expected to lead to new applications. Numerous NW samples were prepared and characterized by this author in order to demonstrate the growth techniques physically. Finite element method simulations were performed and the data was interpreted by this author. Collaborative work was also undertaken in order to present a fuller picture of the topics discussed herein by developing mathematical models to describe the physics. The contributions of each author involved in these collaborations is described in the summary at the beginning of Chapters 4, 5, 6, 7, and 8.

1. Introduction

1.1. Nanowires

The description of what a nanowire (NW) is may vary depending on application and fabrication method. In the most general sense, it is a structure with a diameter on the nanometre scale and with a length much greater than the width. This results in a structure which approaches a 1D case. Such a simplistic description though is vague and does not provide the reader with many details. For example, it does not specify whether the NW lies on its side, horizontal to the substrate, or whether it is positioned vertically, or at any other angle. It does not specify the material or cross-sectional shape, nor the fabrication method or application. The field of NWs is incredibly vast and as the field expands so too do the number of structures included under the “nanowire” umbrella. The community seeks to alter the simplest NW structure to fit an ever-growing number of applications – from biology to quantum information processing.

The work presented in this thesis will focus on one subgroup of NWs. These are NWs grown by the vapor-liquid-solid and self-assisted catalyst methods. These terms will become more familiar later. These methods are applicable to most III-V semiconductors but GaAs will be the primary focus. The GaAs NWs are grown in periodic arrays and are vertical with respect to the substrate. The substrate used is Si. A schematic of a small portion of a GaAs NW array is presented in Figure 1.1(a) and an SEM image of a NW array is shown in Figure 1.1(b).

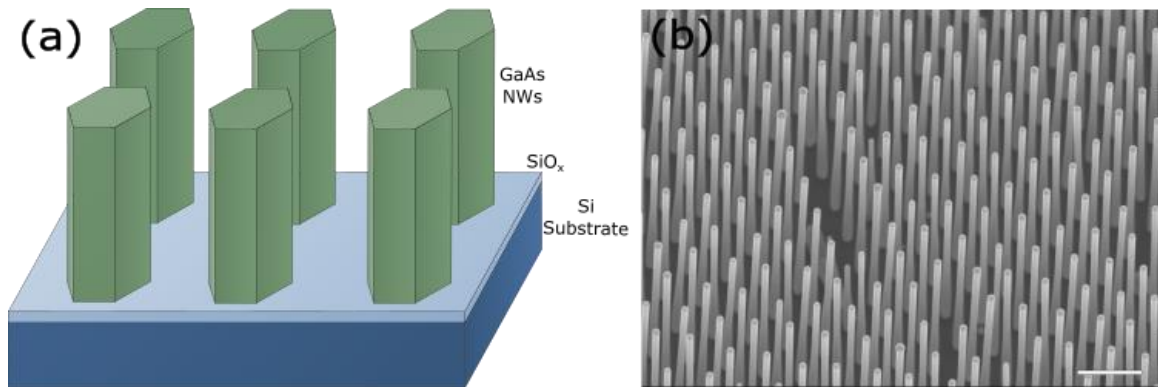


Figure 1.1. (a) A schematic of a small area of a NW array showing hexagonally faceted GaAs NWs (the vertical is in the $\langle 111 \rangle$ direction) on a Si(111) substrate with a SiO_x mask. (b) An SEM image of a NW array with 600 nm pitch. Scale bar is 1 μm .

The well-known paper by Wagner and Ellis [1.1] is often pointed to as one of the first to describe the mechanism behind NW growth. They described the vapor-liquid-solid method, where a liquid, metallic reservoir acts as a sink for vapor particles to collect and then precipitate out as solid crystal. These types of structures, at this point in time, ranged in diameter but were often on the scale of microns [1.2, 1.3] and were generally referred to as “whiskers” rather than the term nanowire used today. These whiskers were described as being either ribbon-like or needle-like with the former being larger and the latter being narrower and exhibiting the more familiar aspects of today’s VLS grown NWs (growth in the $\langle 111 \rangle$ direction, hexagonal faceting, and submicron diameters [1.3–1.5].)

Originally, NW growth resulted in random positioning of the NWs on the substrate; i.e., growth was unordered. Through the VLS method, a solid crystalline structure grows below the droplet as material precipitates out of the liquid. In these early experiments, a variety of liquid catalysts were used including Au, Pt, Pd, Ni, and Ga [1.3, 1.6]. Of these,

Au has remained a popular choice of catalyst for Si, Ge, or III-V NWs. Ga, or other group III materials, is useful for the growth of III-V NWs. Over time, methods of increasing the density and order of NWs emerged. NWs can now be grown at random or in periodic arrays. A simple method for forming nucleation sites is to apply a thin layer of Au then anneal so that the Au layer coalesces into a randomly sized collection of droplets [1.1]. To produce ordered arrays of NWs where each NW is grown at a pre-determined location, methods of selective area epitaxy (SAE) must be implemented. The most common methods of applying the catalyst to the substrate are nano-imprint lithography [1.7] and electron beam lithography [1.8–1.11]. While Au catalysts are advantageous in some areas, this catalyst can be difficult to remove at the end of growth. Au has also been known to form energy states within the bandgap in Si and III-Vs which can have a negative impact on the electrical properties of the material [1.12]. Au catalysts can produce point defects in III-V NWs [1.13]. The diameter of the NW grown with Au catalysts also remains constant since the volume of catalyst remains relatively unchanged throughout the growth process with minimal loss in volume due to surface diffusion and incorporation in the III-V structure.

An alternative to the popular Au catalyst is to grow NWs using the self-catalyzed method. For III-V compounds the group III material acts as a liquid reservoir on top of the NW and the group V material entering the droplet in much lower amounts facilitates the layer-by-layer formation of a solid crystal through precipitation. This technique allows for greater control over the diameter of the NW as the droplet volume can be increased or decreased throughout the growth process. Changing droplet diameter throughout growth

provides much greater control over the optical properties of the NW and allows more complex and precise NW structures to be grown.

1.2. Nanowire Applications

NWs have a wide range of applications in many fields [1.14]. Their optical properties are of particular interest for this work due to their direct relation to the diameter of the NW. The NWs are shown to support the HE_{1n} family of modes. These modes result in improved absorption above the energy gap of the NW. The absorption peaks are seen to shift to longer wavelengths as the diameter of the NW increases [1.15, 1.16]. The tunability of the absorption peaks due to the HE_{1n} modes have made NW arrays valuable for a variety of applications.

One such application is solar cells, with the goal being to position the peaks in the absorption spectra appropriately so that the maximum amount of energy from the solar spectrum may be absorbed. By absorbing a portion of the visible spectrum, the colour of a NW array can also be changed since the reflected spectrum is altered [1.17]. Absorption for solar materials utilizes wide diameter NWs (on the order of 100 nm and greater) with pitches about twice as large. The diameter/pitch combination serves to maximize the absorption at the correct wavelength range while minimizing the reflectance from the tops of the NWs. The diameter/pitch combination which is found to be most efficient for solar absorption in GaAs NWs is around 180 nm in diameter and 360 nm in pitch [1.18, 1.19].

The current record holding solar cell made of GaAs NWs on Si has an efficiency of 7.7% [1.20] while GaAs NWs on GaAs substrates have been able to achieve a record of

15.3% [1.21]. This was grown with a p-i-n “axial” junction oriented in the direction of growth. The other possible p-i-n junction orientation is “radial” and is grown by changing the growth temperature so that conformal layers are grown around the NW core through the vapor-solid method instead of via the metal catalyst [1.22–1.25].

A major improvement in the performance of solar cells was seen after the n-type shell surrounding the axial p-i-n structure was removed [1.17]. Such parasitic shells are inevitable in MBE-grown NWs and have been observed in multiple instances [1.7, 1.26]. These shells are formed through vapor-solid (VS) growth on the NW sidewalls. This shell can affect the NW morphology by widening the NW non-uniformly. Near the top of the NW, the droplet acts as a preferential sink for group III materials. Thus, within a diffusion length of the droplet, Ga will be captured by the droplet and unavailable for VS growth.

Shadowing effects can also impact VS growth in dense NW arrays with sufficiently long NWs [1.27]. Depending on the application, this shell can either be negligible, modifying the NW diameter slightly, or hamper the device performance significantly, for example by electrical shorting of a p-n junction [1.20].

Additional applications have included photodetectors which aim to generate a photocurrent upon the absorption of a certain wavelength of light. When using NWs for this application, the diameter is altered to absorb the desired wavelengths based on the NW material and the application. For example, Ref. [1.28] observed spectral shifting in the mid-wavelength infrared range by simulating the absorptance in InSb NW arrays. The pitch and NW length were optimized to achieve an absorptance of over 60% at approximately 3.7 μm with a NW diameter of 700 nm. The required NW diameter increases for applications

in the long-wavelength infrared. The tunable absorptance is also useful for multispectral imaging. Multispectral imaging devices constructed from NWs have been demonstrated in the visible and near-infrared regions using a grid array of Si NWs ranging from 80 nm to 160 nm in diameter [1.29, 1.30]

On the other extreme, minimizing NWs to extremely thin diameters has applications in quantum information processing. NWs on the order of 10s of nanometres in diameter exhibit quantum confinement and are applicable for single photon emitters [1.31, 1.32]. Ultra-thin NWs have been produced as thin as 2 nm using a Au droplet catalyst [1.33].

NWs for use as lasers presents an interesting class as both the NW diameter and length play an important role. When the length is properly selected, the NW forms a resonant Fabry-Perot cavity which can be used for lasing [1.34]. The Fabry-Perot cavity effect is present in NWs grown on substrates, particularly substrates consisting of another material than the NW itself. This results in some additional oscillations observable in the absorption spectrum as light become trapped within the NW cavity [1.35]. The effect is more prominent when the NW is removed from the surface of the substrate since the NW end facet to air boundary provides higher reflectance and thus greater longitudinal confinement [1.36, 1.37]. The diameter of the NW for these structures remains important since the proper choice can improve lateral confinement as well as the reflectivity at the ends of the NW [1.37]. In some instances, the NW can be made of multiple layers of material forming a distributed Bragg reflector [1.38] which can provide an alternative source of reflectance.

These applications represent only a small fraction of possible NW applications. The applications discussed so far mostly focus on the optical properties of NWs which are akin to classical optical fibers. However, they are also of interest for applications in thermoelectrics [1.39] for their thermal properties and betavoltaics [1.40] for their interaction with nuclear materials.

In all these cases, it is the shape of the NW that plays the characteristic role in determining its properties and thus its effectiveness in a certain application. Control over the NW diameter is therefore an important part of NW technology development.

1.3. Thesis Statement

This thesis focuses on altering the shape of NWs via droplet dynamics for self-catalyzed GaAs NWs grown on Si substrates using molecular beam epitaxy (MBE) and the VLS method. It explores how changing the diameter can be accomplished experimentally and indicates that it can be used to improve yield on lattice mismatched substrates such as Si. Additionally, simulations are used to explore the implications of changing the diameter for device performance. This is first explored using solar cell technologies as the motivation. In the final chapters, it is shown how modulating the diameter can be used to produce novel NW structures with applications in sensors and lasers.

Chapter 2 covers the theory instrumental to this work. It begins by covering some basics of NW nucleation, where growth begins. It discusses the experimental processes behind preparing bare Si substrates for NW growth in MBE. Following this section is a more detailed overview of the VLS method of NW growth. It describes the direct, scattered,

and diffused fluxes of Ga and As and how they combine in the liquid phase Ga droplet atop the NW to precipitate solid layers of GaAs underneath. The third section of this chapter will cover the optical properties of NWs, the modes they support and how morphology and other physical properties can alter the optical properties. Closing the chapter is an explanation of the finite element simulation techniques used, a discussion of the model used and the theory behind the finite element method itself.

The remaining chapters cover the results of the experimental and simulation work performed. Chapter 3 covers work previously published in *Nanotechnology* [1.41]. It focuses on the effect of a Ga pre-deposition step before NW growth and shows its impact on NW yield with respect to pitch (NW spacing) and substrate hole diameter. It gives reasons for why yield may either increase or decrease depending on pitch, hole diameter and the presence of a Si oxide layer remaining on the surface of the substrate. Chapter 4 outlines a model which describes the changing diameter of a NW in terms of the droplet volume and the contact angle that the droplet reservoir makes with the NW sidewalls. The model is fit against data collected by researchers at CNRS (France) and the results have been previously published in *Nanotechnology* as well [1.42]. Chapter 5 gives experimental evidence that the NW diameter can be directly and controllably changed while maintaining a high yield by altering the flux of Ga during the growth process. Inverted conical NWs are formed and their possible applications are described in terms of photovoltaics. This chapter presents a slightly different model for mapping NW growth which does not rely so heavily on knowing the contact angle of the NW. These results were previously published in *IEEE Journal of Photovoltaics* [1.43]. Chapter 6 continues to look at these inverted

conical NWs with a focus on photovoltaic applications. Simulations are performed to show how performance changes as the top diameter, base diameter, and length of the inverted conical NW is changed. Reflectance, transmittance, and photocurrent is calculated and discussed in terms of the NW morphology. The results were previously published in *Optics Express* [1.44]. Chapter 7 explores a novel NW structure. Corrugated NWs have diameters which are modulated periodically. This creates a distributed Bragg reflector (DBR) type of structure which can be tuned by altering the morphology of the corrugation and produces reflection bands. This novel structure has applications in sensors and lasers.

This work provides theoretical and experimental insight into the growth of GaAs NWs on Si substrates. It provides a framework for growing NW arrays with a high yield and excellent control over the diameter. The results presented are widely applicable to any NW grown by the self-catalyzed method. Possible applications for these techniques include NW array solar cells and NW distributed Bragg gratings using a corrugated structure. The work has potential to be built upon extensively. The final chapter discusses future work that could be undertaken to expand on the work done in this thesis. It provides suggestions for future projects and new routes that this work could take.

1.4. References

- [1.1] R. S. Wagner and W. C. Ellis, "Vapor-liquid-solid mechanism of single crystal growth," *Appl. Phys. Lett.*, vol. 4, no. 5, pp. 89–90, 1964.
- [1.2] Y. Nannichi, "Formation of silicon whiskers on a sublimating surface," *Appl. Phys. Lett.*, vol. 3, no. 8, pp. 139–142, 1963.

- [1.3] R. L. Barns and W. C. Ellis, "Whisker crystals of gallium arsenide and gallium phosphide grown by the vapor - liquid - solid mechanism," *J. Appl. Phys.*, vol. 36, no. 7, pp. 2296–2301, 1965.
- [1.4] E. S. Greiner, J. A. Gutowski, and W. C. Ellis, "Preparation of silicon ribbons," *J. Appl. Phys.*, vol. 32, no. 11, pp. 2489–2490, 1961.
- [1.5] R. S. Wagner and R. G. Treuting, "Morphology and growth mechanism of silicon ribbons," *J. Appl. Phys.*, vol. 32, no. 11, pp. 2490–2491, 1961.
- [1.6] E. I. Givargizov, "Periodic instability in whisker growth," *J. Cryst. Growth*, vol. 20, no. 3, pp. 217–226, 1973.
- [1.7] A. M. Munshi et al., "Position-controlled uniform GaAs nanowires on silicon using nanoimprint lithography," *Nano Lett.*, vol. 14, no. 2, pp. 960–966, 2014.
- [1.8] T. Fukui et al., "Growth characteristics of GaAs nanowires obtained by selective area metal–organic vapour-phase epitaxy," *Nanotechnology*, vol. 19, no. 26, 2008, Art. no. 265604.
- [1.9] P. Kuyanov, J. Boulanger, and R. R. LaPierre, "Control of GaP nanowire morphology by group V flux in gas source molecular beam epitaxy," *J. Cryst. Growth*, vol. 462, pp. 29–34, 2017.
- [1.10] S. Plissard, G. Larrieu, X. Wallart, and P. Caroff, "High yield of self-catalyzed GaAs nanowire arrays grown on silicon via gallium droplet positioning," *Nanotechnology*, vol. 22, no. 27, 2011, Art. no. 275602.

- [1.11] Q. Gao et al., “Simultaneous Selective-Area and Vapor-Liquid-Solid Growth of InP Nanowire Arrays,” *Nano Lett.*, vol. 16, no. 7, pp. 4361–4367, 2016.
- [1.12] Y. A. Du, S. Sakong, and P. Kratzer, “As vacancies, Ga antisites, and Au impurities in zinc blende and wurtzite GaAs nanowire segments from first principles,” *Phys. Rev. B - Condens. Matter Mater. Phys.*, vol. 87, no. 7, 2013, Art. no. 075308.
- [1.13] M. Bar-Sadan, J. Barthel, H. Shtrikman, and L. Houben, “Direct imaging of single Au atoms within GaAs nanowires,” *Nano Lett.*, vol. 12, no. 5, pp. 2352–2356, 2012.
- [1.14] R. Yan, D. Gargas, and P. Yang, “Nanowire photonics,” *Nat. Photonics*, vol. 3, no. 10, pp. 569–576, 2009.
- [1.15] K. M. Azizur-Rahman and R. R. LaPierre, “Wavelength-selective absorptance in GaAs, InP and InAs nanowire arrays,” *Nanotechnology*, vol. 26, no. 29, 2015, Art. no. 295202.
- [1.16] N. Anttu, “Absorption of light in a single vertical nanowire and a nanowire array,” *Nanotechnology*, vol. 30, no. 10, 2019 Art. no. 104004.
- [1.17] P. M. Wu, N. Anttu, H. Q. Xu, L. Samuelson, and M. E. Pistol, “Colorful InAs nanowire arrays: From strong to weak absorption with geometrical tuning,” *Nano Lett.*, vol. 12, no. 4, pp. 1990–1995, 2012.
- [1.18] Y. Hu, R. R. LaPierre, M. Li, K. Chen, and J. J. He, “Optical characteristics of

GaAs nanowire solar cells,” *J. Appl. Phys.*, vol. 112, no. 10, 2012, Art. no. 104311.

- [1.19] A. H. Trojnar, C. E. Valdivia, R. R. LaPierre, K. Hinzer, and J. J. Krich, “Optimizations of GaAs nanowire solar cells,” *IEEE J. Photovoltaics*, vol. 6, no. 6, pp. 1494-1501, 2016.
- [1.20] A. Mukherjee, D. Ren, P. E. Vullum, J. Huh, B. O. Fimland, and H. Weman, “GaAs/AlGaAs Nanowire array solar cell grown on Si with ultrahigh power-per-weight ratio,” *ACS Photonics*, vol. 8, no. 8, pp. 2355–2366, 2021.
- [1.21] I. Åberg et al., “A GaAs nanowire array solar cell with 15.3% efficiency at 1 sun,” *IEEE J. Photovoltaics*, vol. 6, no. 1, pp. 185–190, 2016.
- [1.22] T. J. Kempa et al., “Coaxial multishell nanowires with high-quality electronic interfaces and tunable optical cavities for ultrathin photovoltaics,” *Proc. Natl. Acad. Sci. U. S. A.*, vol. 109, no. 5, pp. 1407–1412, 2012.
- [1.23] J. P. Boulanger et al., “Characterization of a Ga-Assisted GaAs nanowire array solar cell on Si substrate,” *IEEE J. Photovoltaics*, vol. 6, no. 3, pp. 661–667, 2016.
- [1.24] J. V. Holm, H. I. Jørgensen, P. Krogstrup, J. Nygård, H. Liu, and M. Aagesen, “Surface-passivated GaAsP single-nanowire solar cells exceeding 10% efficiency grown on silicon,” *Nat. Commun.*, vol. 4, 2013, Art. no. 1498.
- [1.25] S. K. Kim et al., “Tuning light absorption in core/shell silicon nanowire photovoltaic devices through morphological design,” *Nano Lett.*, vol. 12, no. 9, pp.

4971–4976, 2012.

- [1.26] H. Küpers et al., “Diameter evolution of selective area grown Ga-assisted GaAs nanowires,” *Nano Res.*, vol. 11, no. 5, pp. 2885–2893, 2018.
- [1.27] E. S. Koivusalo, T. V. Hakkarainen, M. D. Guina, and V. G. Dubrovskii, “Sub-poissonian narrowing of length distributions realized in Ga-catalyzed GaAs nanowires,” *Nano Lett.*, vol. 17, no. 9, pp. 5350–5355, 2017.
- [1.28] K. M. Azizur-Rahman and R. R. LaPierre, “Optical design of a mid-wavelength infrared InSb nanowire photodetector,” *Nanotechnology*, vol. 27, no. 31, 2016, Art. no. 315202.
- [1.29] H. Park and K. B. Crozier, “Multispectral imaging with vertical silicon nanowires,” *Sci. Rep.*, vol. 3, 2013, Art. no. 2460.
- [1.30] H. Park et al., “Filter-free image sensor pixels comprising silicon nanowires with selective color absorption,” *Nano Lett.*, vol. 14, no. 4, pp. 1804–1809, 2014.
- [1.31] W. Kim et al., “Bistability of Contact Angle and Its Role in Achieving Quantum-Thin Self-Assisted GaAs nanowires,” *Nano Lett.*, vol. 18, no. 1, pp. 49–57, 2018.
- [1.32] M. E. Reimer et al., “Bright single-photon sources in bottom-up tailored nanowires,” *Nat. Commun.*, vol. 3, 2012, Art. no. 737.
- [1.33] G. Zhang, K. Tateno, H. Sanada, T. Tawara, H. Gotoh, and H. Nakano, “Synthesis of GaAs nanowires with very small diameters and their optical properties with the radial quantum-confinement effect,” *Appl. Phys. Lett.*, vol. 95, no. 12, 2009, Art.

no. 123104.

- [1.34] B. Hua, J. Motohisa, Y. Ding, S. Hara, and T. Fukui, “Characterization of Fabry-Pérot microcavity modes in GaAs nanowires fabricated by selective-area metal organic vapor phase epitaxy,” *Appl. Phys. Lett.*, vol. 91, no. 13, 2007, Art. no. 131112.
- [1.35] B. C. P. Sturmberg et al., “Modal analysis of enhanced absorption in silicon nanowire arrays,” *Opt. Express*, vol. 19, no. S5, pp. A1067–A1081, 2011.
- [1.36] D. Saxena et al., “Optically pumped room-temperature GaAs nanowire lasers,” *Nat. Photonics*, vol. 7, no. 12, pp. 963–968, 2013.
- [1.37] A. V. Maslov and C. Z. Ning, “Reflection of guided modes in a semiconductor nanowire laser,” *Appl. Phys. Lett.*, vol. 83, no. 6, pp. 1237–1239, 2003.
- [1.38] I. Friedler et al., “Efficient photonic mirrors for semiconductor nanowires,” *Opt. Lett.*, vol. 33, no. 22, 2008, Art no. 2635.
- [1.39] A. Ghukasyan and R. R. LaPierre, “Modelling thermoelectric transport in III–V nanowires using a Boltzmann transport approach: a review,” *Nanotechnology*, vol. 32, no. 4, 2021, Art. no. 042001.
- [1.40] S. McNamee, D. Wagner, E. M. Fiordaliso, D. Novog, and R. R. LaPierre, “GaP nanowire betavoltaic device,” *Nanotechnology*, vol. 30, no. 7, 2019, Art. no. 075401.
- [1.41] D. P. Wilson, V. G. Dubrovskii, and R. R. LaPierre, “Improving the yield of GaAs

nanowires on silicon by Ga pre-deposition,” *Nanotechnology*, vol. 32, no. 26, 2021, Art. no. 265301.

[1.42] D. P. Wilson, A. S. Sokolovskii, R. R. LaPierre, F. Panciera, F. Glas, and V. G. Dubrovskii, “Modeling the dynamics of interface morphology and crystal phase change in self-catalyzed GaAs nanowires,” *Nanotechnology*, vol. 31, no. 48, 2020, Art. no. 485602.

[1.43] D. P. Wilson, A. S. Sokolovskii, N. I. Goktas, V. G. Dubrovskii, and R. R. LaPierre, “Photovoltaic Light Funnels Grown by GaAs Nanowire Droplet Dynamics,” *IEEE J. Photovoltaics*, vol. 9, no. 5, pp. 1225–1231, 2019.

[1.44] D. P. Wilson and R. R. LaPierre, “Simulation of optical absorption in conical nanowires,” *Opt. Express*, vol. 29, no. 6, pp. 9544-9552, 2021.

2. Theory

2.2. Nanowire Nucleation

Vapor-liquid-solid (VLS) growth of self-catalyzed III-V nanowires (NWs) in molecular beam epitaxy (MBE) consists of a vapor phase provided by the MBE beams, a liquid droplet of the group III material which acts as a reservoir for the collection of the vapor phase, and the solid phase which forms layer-by-layer by precipitation of solid material from the supersaturated droplet [2.1]. The perimeter of the NW top is known as the triple phase line and is the interface at which all three phases meet. Nucleation that occurs at this phase line results in WZ crystal structure and ZB if nucleation occurs at the liquid-solid interface [2.2]. Nucleation is dependent on the Gibbs free energy of the system [2.3, 2.4]. Self-catalyzed VLS growth of GaAs in an MBE chamber is always As limited [2.5]. The Ga reservoir must be refilled with enough As before a new layer can be precipitated. This is known as nucleation anti-bunching, where there is a finite amount of time between nucleation events [2.4].

Epitaxial NW growth of III-V material begins with the formation of a droplet reservoir at the substrate surface. The substrate is typically III-V or Si. If the self-catalyzed method is being used, then Ga or other group III material is deposited on the surface. The Ga must accumulate into a droplet and the surface must be prepared in such a way that droplets form rather than liquid islands. Ga collects in etch pits or pin holes in the surface oxide of the substrate which are more energetically favorable for droplet collection [2.6]. Alternatively, if the surface of the substrate contains nonuniformities or defects, then these can also act as nucleation sites. Self-catalyzed NWs have been observed growing on

roughened surfaces such as at scratches and defects in III-V thin films [2.7] and along the cleaved edges of substrates [2.8]. An oxide layer, commonly SiO_x , is used to assist in the formation of nucleation sites. Ga has been observed etching back oxides such as SiO_x on the surface of substrates to form etch pits [2.9]. The etching back of the oxide layer is important since removing enough of the oxide layer allows the droplet to contact the crystalline substrate beneath it and for the NW to grow epitaxially as a result.

A patterned array can be created by etching holes into the oxide layer. First a SiO_x oxide layer is grown and then the array is patterned using electron-beam lithography and a combination of dry and wet etching [2.10]. This produces openings in the oxide surface down to the substrate layer into which Ga or other group III materials can diffuse.

The filling of these holes with a liquid volume of Ga becomes important for determination of the NW yield (i.e., whether a NW will result at a particular location or not). In the ideal case, the droplet will wet the oxide hole symmetrically and will not overflow it. Whether a nucleation event successfully produces a vertical NW depends on the droplet orientation and its interaction with the oxide layer. Reference [2.3] examined the relationship between the droplet contact angle and its position inside an oxide hole. For an underfilled hole with no residual oxide present, small droplets will tend to fill the hole entirely. This mechanism results in even wetting of the hole at all sides. If the hole is overfilled the droplet contact angle and oxide thickness becomes more important. The atomic composition of the oxide layer can change the contact angle for Ga droplets when it sits on top of the oxide layer. Larger contact angles ($> 90^\circ$) in this configuration are more

likely to result in vertical NWs. If the droplet overfills the hole unevenly, a crystallite or a kinked NW may be the preferred orientation [2.3].

The exact thickness of the oxide required for NW growth varies between studies. Usually the oxide thickness is at most around 30 nm or less [2.5, 2.11]. Oxide layers that are too thick have been shown to prevent NW growth [2.5]. Conversely, although growth of NWs without the presence of an oxide has been demonstrated [2.12], it is considered less ideal as it is often reported that crystallites or thin films are more likely to be grown on oxide-free substrates [2.5].

The substrate chosen also has an impact on the NW growth. $\langle 111 \rangle$ is a preferred growth direction for III-V NWs as well as Si and Ge NWs. The crystal orientation of the substrate controls the angle of growth with respect to the substrate surface [2.13]. For example, on a (100) oriented substrate, NWs are observed growing at a tilt angle of 35° with respect to the substrate surface [2.9]. Since vertical NWs are preferable for a variety of applications, a $\langle 111 \rangle$ substrate orientation is often chosen. Even though the 90° vertical angle is the most likely growth orientation, GaAs NWs on Si(111) substrates may also grow at an angle of 19.5° [2.13]. The latter orientation is thought to be due to the crystal mismatch between the substrate and the NW lattice.

The crystal lattice constant of the substrate is particularly important if the substrate and the NW are different materials. Two crystalline materials of different crystal lattice constant become strained due to the deformation of the crystal structure at the interface. For the case of GaAs and Si, this difference in lattice constants amounts to 4.1%. In a thin film, the energy to deform the material is a function of the thickness. At some critical

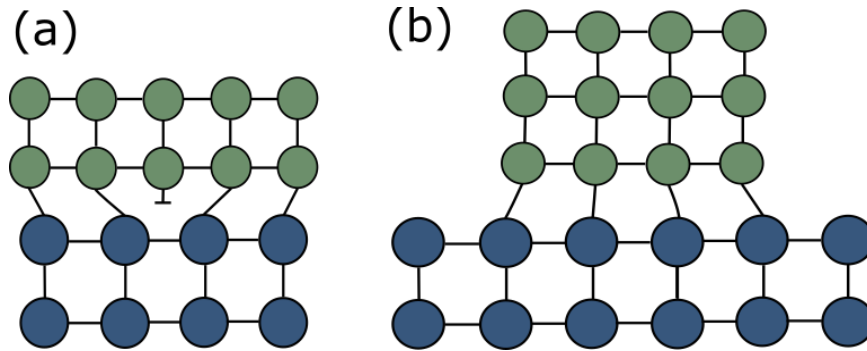


Figure 2.1. A heterostructure consisting of a substrate and epitaxial layer with different lattice constants. The strain is relaxed in (a) plastically, through the formation of a misfit dislocation and in (b) elastically.

thickness, the elastic volume strain energy is equal to the energy required to relax strain through the formation of dislocations. At and above this critical thickness, dislocations will form within the crystal lattice [2.14]. The formation of “misfit” dislocations is known as plastic relaxation and is demonstrated in Figure 2.1 (a). Misfit dislocations provide trap states for charge carriers and can be detrimental to the electrical properties of the structure. Dislocations can also be present in NWs; however, the NW structure presents a significant advantage in this regard over the thin film. In this case, the strain may be relaxed elastically towards the NW sidewalls [2.15] as shown in Figure 2.1 (b). Due to the relatively small epitaxial area that the NW makes with the substrate, it is possible to grow NWs without dislocations. For a given lattice mismatch, the critical thickness will increase as the NW diameter decreases. For some diameter, the critical thickness approaches infinity [2.16]. Below this critical diameter, the NW can accommodate all strain elastically. This diameter is dependent on the degree of lattice mismatch between materials. Larger mismatches

require small NW footprints to accommodate the strain sufficiently. For the combination of GaAs on Si(111) substrates, the critical diameter has been estimated to be below 110 nm [2.17].

2.3. Nanowire Growth

Molecular beam epitaxy (MBE) is just one of the possible ways of growing NWs. In an MBE chamber the pressures are less than 10^{-10} Torr. Atomic precursors are supplied by effusion cells placed around the edge of the growth chamber. The sample sits at the centre of the chamber on a rotating holder [2.18].

Once the droplet has nucleated on the surface, the NW may begin to grow. Arsenic (As) has a much higher vapor pressure than Ga. In the MBE chamber, under high vacuum, Ga either coalesces into the liquid droplet or diffuses along the surface for some finite distance. The As atoms on the other hand are quickly desorbed from the surface. The Ga droplet acts as a reservoir into which As atoms can collect over time [2.12, 2.19]. Once the concentration of As within the Ga reservoir is sufficiently high, a new layer will nucleate and form. This process occurs rapidly, with the formation of an island at the triple phase line which then spreads across the top facet of the NW [2.20–2.22]. When there is a limited amount of material present, as is true for the As adatoms in self-catalyzed GaAs growth, this process leads to nucleation anti-bunching where the droplet takes a finite time to refill with atomic constituents before a new monolayer can form [2.4, 2.23].

The pathways of collecting adatoms in the droplet are direct impingement, diffusion along the NW sidewalls, or scattering [2.24]. The diffusion pathway is unavailable for As

adatoms due to their high vapor flux [2.25] but is a particularly important pathway for the Ga adatoms in self-catalyzed systems. A diffusion-dominated growth will have a growth rate proportional to $1/r^p$ where r is the radius and p is between 0.5 and 2 [2.26]. As the NW grows, shadowing effects can be present due to the angle of the Ga beam in the MBE chamber [2.24]. This angle can reduce the area along the NW sidewalls accessible to the direct flux of adatoms. For dense NW arrays with small pitches, this can lower the amount of adatoms that contribute to vapor-solid (VS) growth along the NW sidewalls [2.27]. Additionally, NW arrays with a small pitch can have lower effective flux rates compared to the effective flux rates of NWs in sparse arrays due to competition for adatom collection between NWs [2.28]. The diffusion length of a group III adatom is the average length that it can travel before desorption or incorporation. For NW pitches smaller than the diffusion length on the substrate, a single group III adatom may be collected by one of several neighboring NWs. Similarly, an adatom on the sidewall must be within a diffusion length to reach the droplet and contribute to axial NW growth.

As mentioned previously, in addition to the VLS growth mechanism, the vapor-solid (VS) method is also present. In this mechanism, As atoms combine directly with a Ga atom on the sidewalls of the GaAs NW. In some NW designs, this type of growth may be undesired (particularly if dopants are present) but is difficult to avoid. VS growth has been observed occurring in combination with VLS growth, widening the bottom portion of the NW [2.29]. This widening of the base is most prominent for short NWs with wide pitches where shadowing is minimal. On the other extreme, where the array is dense and the NWs are long, shadowing may reduce the amount of VS growth at the very bottom of the NW and

the NW may instead appear wider in the middle [2.27]. The diffusion length of a group III adatom decreases with decreasing temperature making VS growth more likely since the Ga adatoms spend a longer time on the sidewalls of the NW [2.30]. Lowering the temperature can make the VS growth method dominate and is often done to grow “core-shell” NWs. In this technique, the VLS method is used to grow NW cores of the desired length first before the temperature is lowered to grow a shell around the core by VS growth [2.31, 2.32]. This technique is useful for “radial” doping strategies and passivation [2.33, 2.34].

The possible adatom pathways are indicated in Figure 2.2. The inset shows important angles and geometry. The diameter of the NW is directly related to the volume and shape of the droplet on its top. The contact angle, β , is the angle the droplet makes with the sidewalls of the NW and is taken with respect to the horizontal by convention regardless of any faceting at the NW top. The angle, θ , is the angle that the beams make with respect to the vertical. This quantity is specific to the MBE system and may vary depending on the setup.

A III-V NW takes either the zinc-blende (ZB) or the wurtzite (WZ) crystal structure. The distinction between the two crystal lattices is known to depend on the contact angle on the top of the NW. For large contact angles (generally reported above 125°) and very small contact angles (generally reported below 100°), the crystal phase is ZB; otherwise it takes on the WZ orientation [2.35–2.37]. The dependence on the contact angle also indicates how the NW diameter changes. It is ZB when the top of the NW has non-vertical sidewalls, which must be present if the NW is to widen or narrow. The WZ phase is only seen to occur for vertical NW sidewalls [2.36, 2.37].

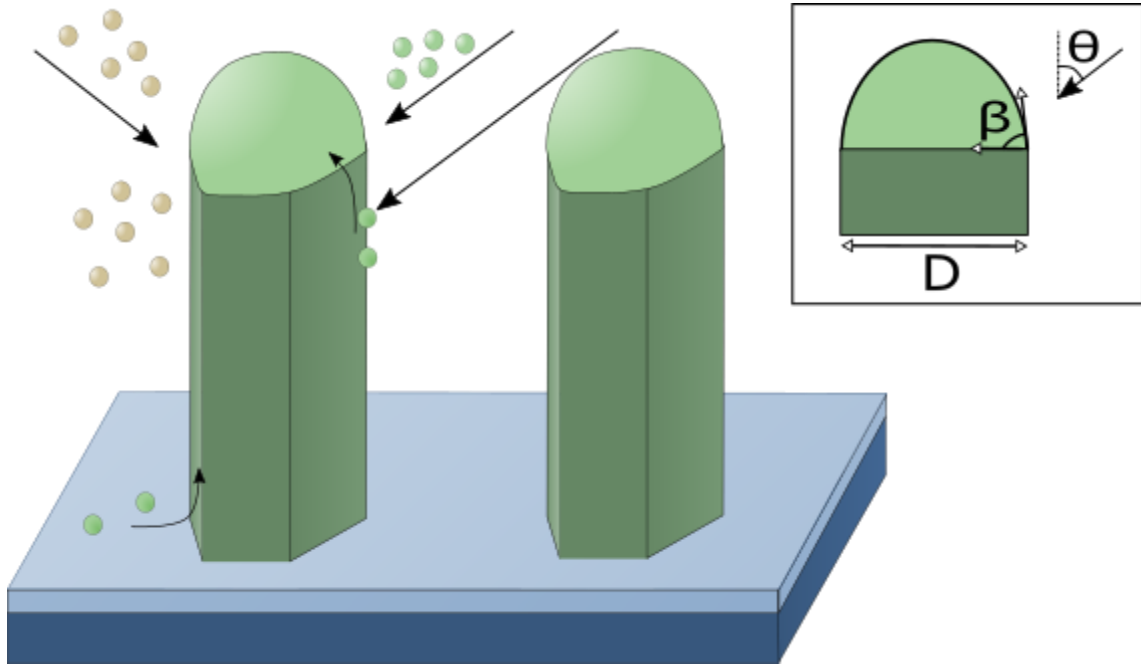


Figure 2.2. Possible adatom fluxes for NWs in an MBE chamber. The MBE supplies a direct flux of material at an angle θ with respect to the vertical. Neighboring NWs can shadow the substrate and sidewalls from this direct flux. The group III adatoms can diffuse along both the substrate and sidewalls of the NW and collect in the droplet reservoir at the top of the NW. Arrows show the direction of diffusion as upwards, towards the droplet, but the diffusion occurs in multiple directions. Group III atoms may even diffuse into or out of the droplet. Group V adatoms tend not to diffuse and only interact if they encounter a group III atom either in the droplet reservoir or on the NW sidewalls for VS growth. The inset shows the geometry at the top of the NW where D is the diameter, β is the contact angle with respect to the horizontal, and θ is the beam angle with respect to the vertical.

2.4. Nanowire Optical Properties

NW optical properties can be described in the terms associated with cylindrical optical fibers with the most obvious caveat being that NWs are of finite length and smaller diameter. In a simple step index optical fiber, a cylindrical core material of some refractive index, n_1 , is surrounded by a cladding material of index n_2 where $n_1 > n_2$. Light entering the fiber at angles less than the critical angle can undergo total internal reflection and are guided along the length of the fiber without loss of power.

The behaviour of electromagnetic waves in a medium is governed by Maxwell's equations:

$$\nabla \times \vec{E} = -\frac{\partial \vec{B}}{\partial t} \quad (2.1)$$

$$\nabla \times \vec{H} = \vec{J} + \frac{\partial \vec{D}}{\partial t} \quad (2.2)$$

$$\nabla \cdot \vec{D} = \rho \quad (2.3)$$

$$\nabla \cdot \vec{B} = 0 \quad (2.4)$$

where \vec{E} is the electric field and \vec{H} is the magnetic field. These quantities are related to the electric field displacement, $\vec{D} = \epsilon \vec{E}$, the magnetic induction, $\vec{B} = \mu \vec{H}$, and the electric current density, $\vec{J} = \sigma \vec{E}$. The permittivity, ϵ , of the dielectric material describes its susceptibility to polarization. μ is the magnetic permeability. It is usually easier to discuss the permittivity and susceptibility in terms of the relative quantities: $\epsilon_r = \epsilon/\epsilon_0$ and $\mu_r = \mu/\mu_0$ where ϵ_0 and μ_0 refer to the values in free space. The relative permittivity is related to the complex refractive index by $\epsilon_r = n^2$. For non-magnetic materials the relative

magnetic permeability, μ_r , is equal to 1. The conductivity is given by σ , and the free charge is given by ρ . For a dielectric, σ and ρ can usually be taken to be 0 since perfect dielectrics do not carry free charge and thus do not conduct current.

The equation for a plane wave can be derived from Maxwell's equations. It takes the form:

$$\vec{E} = \vec{E}_0 \exp(-i(\beta z - \omega t)) \quad (2.5)$$

where the wave travels in the direction \hat{z} . Only the steady state will be considered here and the time dependence, $\exp(-i\omega t)$, will be dropped in future expressions. The propagation constant, β , is the component of the wavevector in the direction of propagation.

The eigenvalue equation for cylindrical step-index optical fibers is given as [38]:

$$\left[\frac{J'_q(u)}{uJ_q(u)} + \frac{K'_q(w)}{wK_q(w)} \right] \left[\frac{n_1^2}{n_2^2} \frac{J'_q(u)}{uJ_q(u)} + \frac{K'_q(w)}{wK_q(w)} \right] = q^2 \left(\frac{1}{u^2} + \frac{1}{w^2} \right) \left(\frac{n_1^2}{n_2^2} \frac{1}{u^2} + \frac{1}{w^2} \right) \quad (2.6)$$

with:

$$u = a\sqrt{n_1^2 k^2 - \beta^2} \quad (2.7)$$

$$w = a\sqrt{\beta^2 - n_2^2 k^2} \quad (2.8)$$

where u is the normalized transverse phase constant and w is the normalized transverse attenuation coefficient. Additionally, a is the radius of the fiber core, n_1 is the refractive index in the core, n_2 is the refractive index in the cladding, β is the propagation constant (axial component of the wavevector), and k is the wavevector and is equal to $2\pi/\lambda_0$ where λ_0 is the wavelength in free space. Both u and w are used to define the V parameter:

$$V = \sqrt{u^2 + w^2} = ak_0\sqrt{n_1^2 - n_2^2} \quad (2.9)$$

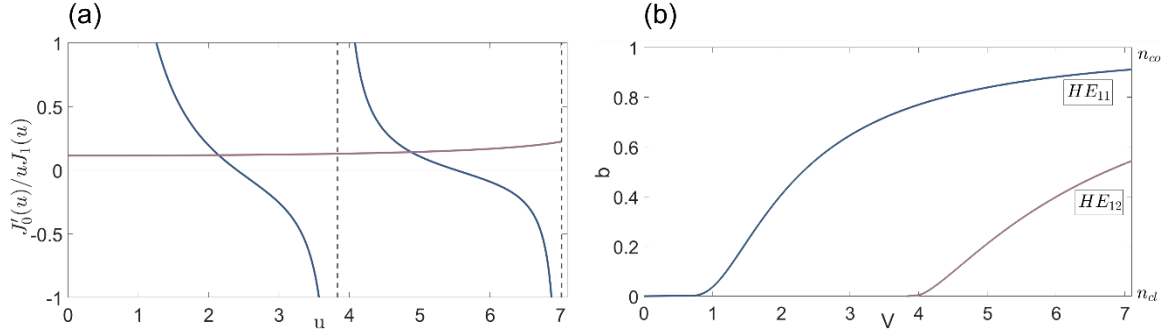


Figure 2.3: (a) Solutions of the eigenvalue equation for the HE₁₁ and HE₁₂ modes as the intercepts of the left- and right-hand sides of the eigenvalue equation for $V = 8$. (b) The normalized propagation constant, $b = 1 - u^2/V^2$, versus V for the HE₁₁ and HE₁₂ modes. The limits of the refractive index, in the core and in the cladding, are indicated on the right-hand side.

The functions J_q and K_q are Bessel functions of the first kind and modified Bessel functions of the second kind, respectively. The prime indicates the first order derivative and q is the azimuthal order.

The eigenvalue equation describes the allowed solutions of Maxwell's equations for the boundary conditions of a step-index optical fiber. At any given wavelength and fiber core diameter, the propagation constant can be solved. This is demonstrated in Figure 2.3(a) by finding the intercepts of the left- and right-hand sides of the eigenvalue equation for the HE modes. Figure 2.3(a) also demonstrates the discrete nature of the bound modes.

The solutions of the eigenvalue equation gives rise to several classifications of modes. When the z-component of the electric field is zero then the fields are said to be

transverse electric (TE) since the electric field is entirely confined to the transverse plane. Likewise, the transverse magnetic (TM) mode occurs when the magnetic field component along \hat{z} is zero. The hybrid classification (either EH or HE) maintains a non-zero z-component. Each mode in a family is given an index (TE_{0n}, TM_{0n}, EH_{mn}, and HE_{mn}). The index m is the azimuthal order and the index n is the radial order. The normalized propagation constant $b = 1 - u^2/V^2$ is shown in Figure 2.3(b) for the HE₁₁ and HE₁₂ modes on the main y-axis. The limits of the effective refractive index of the mode, defined as $n_{eff} = \beta/k$, are indicated in Figure 2.3(b), ranging from between n_{cl} to n_{co} . The fundamental HE₁₁ mode does not exhibit a cutoff and the waveguide is single-mode, supporting only the fundamental mode below $V = 2.405$ [2.39]. Above this value, the waveguide is multi-mode.

The complete electromagnetic field is described as a set of orthonormal bound and radiation modes. Bound modes are confined within the core of the optical fiber, while unbound radiation modes extend into the cladding. Each type of mode is characterized by the range into which its propagation constant falls. For bound modes, we have $kn_2 < \beta \leq kn_1$. The value of β is given by the eigenvalue equation of the system. For unbound radiation modes, the propagation constant forms a continuous set with values ranging from $0 \leq \beta < kn_2$. When β is imaginary, the modes are evanescent and exhibit exponential decay away from the core [2.40].

One additional type of mode is extremely useful for describing the behaviour of power in an optical fiber. Leaky modes meet the requirement for transverse resonance within the optical fiber but

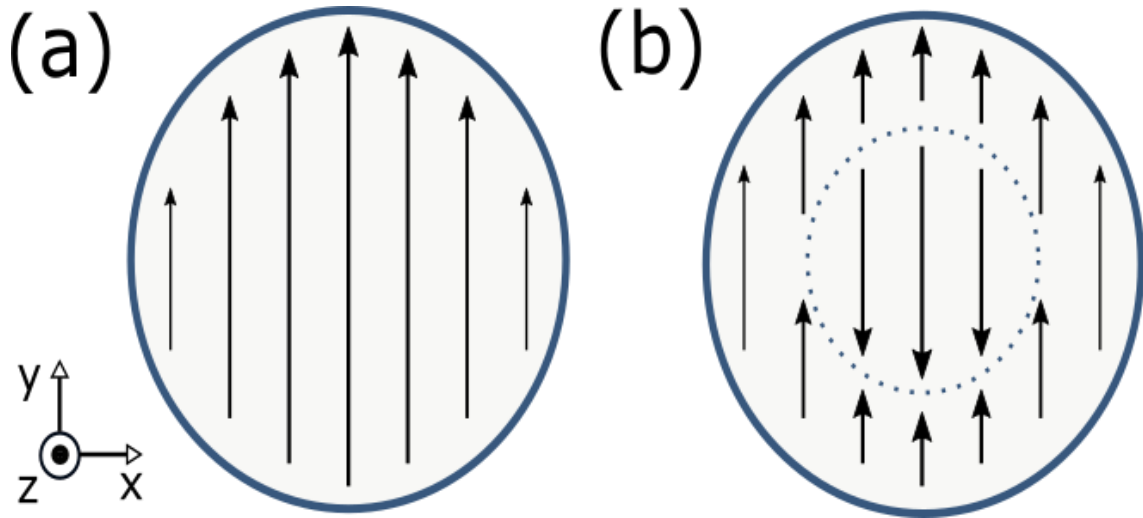


Figure 2.4. The electric field vectors in the transverse plane for (a) the HE_{11} mode and (b) the HE_{12} mode.

some power is lost into the surrounding material as the mode propagates down the axis of the waveguide [2.38]. In the cross-section of the plane, more power is found at larger distances away from the core as z increases due to this power leakage [2.38, 2.41]. The propagation constant of a leaky mode is complex.

NWs exhibit leaky modes with HE_{1n} ($n \geq 1$) character. Only the HE_{1n} modes are excited since they match the symmetry of the linearly polarized light that is used to illuminate the NWs [2.42]. The field patterns in the transverse plane of the fundamental HE_{11} mode and the HE_{12} mode are shown in Figure 2.4.

An additional power loss mechanism is through absorption. Absorption of a photon generates an electron-hole pair in a semiconductor when the energy of the incoming light is above the bandgap of the semiconducting material. For GaAs, this bandgap is 1.42 eV at 300 K, or 872 nm. No absorption occurs for wavelengths above 872 nm. Absorbing

materials have a complex refractive index: $\bar{n} = n + i\kappa$. Here, n is the real part of the refractive index and κ is the imaginary component and is known as the extinction coefficient.

Above the bandgap of the NW semiconducting material, the NWs exhibit peaks in the absorptance spectrum attributable to the confinement of the HE_{1n} modes. The field strength inside the NW core is enhanced by the confinement of these modes, which produces an increase in the absorption [2.43, 2.44]. The absorption peak red-shifts as the diameter of the NW increases [2.42, 2.44–2.46]. The increase in absorption is larger than what would normally be attributable to light incident on the end facet of the NW. In this case the absorption cross-section exceeds the geometric cross-section [2.44, 2.45]. The absorption cross-section has been observed to increase without bound for sparse NW arrays as the length is increased [2.47].

Additionally, since NWs are positioned in arrays, near field coupling can occur. This results in a change to the local effective refractive index, which can be accounted for in the dispersion equation [2.48]. An increasingly dense array of NWs will cause stronger near-field coupling and a decrease in the local effective refractive index. This decrease in n_{eff} will cause the peaks in the absorptance spectrum to blue-shift [2.49].

2.5. References

- [2.1] P. C. McIntyre and A. Fontcuberta i Morral, “Semiconductor nanowires: to grow or not to grow?,” *Mater. Today Nano*, vol. 9, 2020, Art. no. 100058.
- [2.2] G. E. Cirlin et al., “Self-catalyzed, pure zincblende GaAs nanowires grown on

- Si(111) by molecular beam epitaxy,” *Phys. Rev. B - Condens. Matter Mater. Phys.*, vol. 82, no. 3, 2010, Art. no. 035302.
- [2.3] F. Matteini et al., “Impact of the Ga Droplet Wetting, Morphology, and Pinholes on the Orientation of GaAs Nanowires,” *Cryst. Growth Des.*, vol. 16, no. 10, pp. 5781–5786, 2016.
- [2.4] F. Glas and V. G. Dubrovskii, “Energetics and kinetics of monolayer formation in vapor-liquid-solid nanowire growth,” *Phys. Rev. Mater.*, vol. 4, no. 8, 2020, Art. no. 083401.
- [2.5] C. Colombo, D. Spirkoska, M. Frimmer, G. Abstreiter, and A. Fontcuberta i Morral, “Ga-assisted catalyst-free growth mechanism of GaAs nanowires by molecular beam epitaxy,” *Phys. Rev. B - Condens. Matter Mater. Phys.*, vol. 77, 2008, Art. no. 155326.
- [2.6] J. Tersoff, D. E. Jesson, and W. X. Tang, “Decomposition controlled by surface morphology during Langmuir evaporation of GaAs,” *Phys. Rev. Lett.*, vol. 105, no. 3, 2010, Art. no. 035702.
- [2.7] J. R. Arthur and J. J. LePore, “GaAs, GaP, and GaAs_xP_{1-x} epitaxial films grown by molecular beam deposition,” *J. Vac. Sci. Technol.*, vol. 6, pp. 545–548, 1969.
- [2.8] F. Jabeen, V. Grillo, S. Rubini, and F. Martelli, “Self-catalyzed growth of GaAs nanowires on cleaved Si by molecular beam epitaxy,” *Nanotechnology*, vol. 19, no. 27, 2008, Art. no. 275711.
- [2.9] A. Fontcuberta I Morral, C. Colombo, G. Abstreiter, J. Arbiol, and J. R. Morante, “Nucleation mechanism of gallium-assisted molecular beam epitaxy growth of

- gallium arsenide nanowires,” *Appl. Phys. Lett.*, vol. 92, no. 6, 2008, Art. no. 063112.
- [2.10] S. J. Gibson, J. P. Boulanger, and R. R. LaPierre, “Opportunities and pitfalls in patterned self-catalyzed GaAs nanowire growth on silicon,” *Semicond. Sci. Technol.*, vol. 28, no. 10, 2013, Art. no. 105025.
- [2.11] J. Vukajlovic-Plestina et al., “Fundamental aspects to localize self-catalyzed III-V nanowires on silicon,” *Nat. Commun.*, vol. 10, no. 1, 2019, Art. no. 869.
- [2.12] S. Plissard et al., “Gold-free growth of GaAs nanowires on silicon: Arrays and polytypism,” *Nanotechnology*, vol. 21, no. 38, 2010, Art. no. 385602.
- [2.13] S. A. Fortuna and X. Li, “Metal-catalyzed semiconductor nanowires: A review on the control of growth directions,” *Semicond. Sci. Technol.*, vol. 25, no. 2, 2010, Art. no. 024005.
- [2.14] U. W. Pohl, *Epitaxy of Semiconductors: Physics and Fabrication of Heterostructures*, 2nd ed. Springer Nature, 2020.
- [2.15] E. Ertekin, P. A. Greaney, D. C. Chrzan, and T. D. Sands, “Equilibrium limits of coherency in strained nanowire heterostructures,” *J. Appl. Phys.*, vol. 97, no. 11, 2005, Art. no. 114325.
- [2.16] F. Glas, “Critical dimensions for the plastic relaxation of strained axial heterostructures in free-standing nanowires,” *Phys. Rev. B - Condens. Matter Mater. Phys.*, vol. 74, no. 12, 2006, Art. no. 121302.
- [2.17] G. E. Cirlin et al., “Critical diameters and temperature domains for MBE growth of III-V nanowires on lattice mismatched substrates,” *Phys. Status Solidi - Rapid Res.*

- Lett., vol. 3, no. 4, pp. 112–114, 2009.
- [2.18] J. Orton and T. Foxon, “Machine Technology,” in *Molecular Beam Epitaxy: A Short History*, New York: Oxford University Press, 2015, pp. 75–111.
- [2.19] V. G. Dubrovskii, “Refinement of Nucleation Theory for Vapor-Liquid-Solid Nanowires,” *Cryst. Growth Des.*, vol. 17, no. 5, pp. 2589–2593, 2017.
- [2.20] F. Glas, J. C. Harmand, and G. Patriarche, “Why does wurtzite form in nanowires of III-V zinc blende semiconductors?,” *Phys. Rev. Lett.*, vol. 99, no. 14, 2007, Art. no. 146101.
- [2.21] C.-Y. Wen et al., “Periodically Changing Morphology of the Growth Interface in Si, Ge, and GaP Nanowires,” *Phys. Rev. Lett.*, vol. 107, no. 2, 2011, Art. no. 025503.
- [2.22] A. D. Gamalski, C. Ducati, and S. Hofmann, “Cyclic supersaturation and triple phase boundary dynamics in germanium nanowire growth,” *J. Phys. Chem. C*, vol. 115, no. 11, pp. 4413–4417, 2011.
- [2.23] F. Glas, J. C. Harmand, and G. Patriarche, “Nucleation antibunching in catalyst-assisted nanowire growth,” *Phys. Rev. Lett.*, vol. 104, no. 13, 2010, Art. no. 135501.
- [2.24] S. J. Gibson and R. R. LaPierre, “Model of patterned self-assisted nanowire growth,” *Nanotechnology*, vol. 25, no. 41, 2014, Art. no. 415304.
- [2.25] J. R. Arthur, “Interaction of Ga and As₂ molecular beams with GaAs surfaces,” *J. Appl. Phys.*, vol. 39, no. 8, pp. 4032–4034, 1968.
- [2.26] V. G. Dubrovskii and Y. Y. Hervieu, “Diffusion-induced growth of nanowires:

- Generalized boundary conditions and self-consistent kinetic equation,” *J. Cryst. Growth*, vol. 401, pp. 431–440, 2014.
- [2.27] N. V. Sibirev, M. Tchernycheva, M. A. Timofeeva, J. C. Harmand, G. E. Cirlin, and V. G. Dubrovskii, “Influence of shadow effect on the growth and shape of InAs nanowires,” *J. Appl. Phys.*, vol. 111, no. 10, 2012, Art. no. 104317.
- [2.28] M. H. Madsen et al., “Experimental determination of adatom diffusion lengths for growth of InAs nanowires,” *J. Cryst. Growth*, vol. 364, pp. 16–22, 2013.
- [2.29] H. Küpers et al., “Diameter evolution of selective area grown Ga-assisted GaAs nanowires,” *Nano Res.*, vol. 11, no. 5, pp. 2885-2893, 2018.
- [2.30] X. L. Chen, Y. C. Lan, J. Y. Li, Y. G. Cao, and M. He, “Radial growth dynamics of nanowires,” *J. Cryst. Growth*, vol. 222, no. 3, pp. 586–590, 2001.
- [2.31] A. C. E. Chia et al., “Electrical transport and optical model of GaAs-AlInP core-shell nanowires,” *J. Appl. Phys.*, vol. 111, no. 9, 2012, Art. no. 094319.
- [2.32] J. P. Boulanger et al., “Characterization of a Ga-Assisted GaAs Nanowire Array Solar Cell on Si Substrate,” *IEEE J. Photovoltaics*, vol. 6, no. 3, pp. 661–667, 2016.
- [2.33] B. M. Kayes, H. A. Atwater, and N. S. Lewis, “Comparison of the device physics principles of planar and radial p-n junction nanorod solar cells,” *J. Appl. Phys.*, vol. 97, no. 11, 2005, Art. no. 114302.
- [2.34] N. Huang and M. L. Povinelli, “Design of passivation layers on axial junction GaAs nanowire solar cells,” *IEEE J. Photovoltaics*, vol. 4, no. 6, pp. 1511–1517, 2014.

- [2.35] T. Rieger, M. I. Lepsa, T. Schapers, and D. Grützmacher, “Controlled wurtzite inclusions in self-catalyzed zinc blende III-V semiconductor nanowires,” *J. Cryst. Growth*, vol. 378, pp. 506–510, 2013.
- [2.36] F. Panciera et al., “Phase Selection in Self-catalyzed GaAs Nanowires,” *Nano Lett.*, vol. 20, no. 3, pp. 1669–1675, 2020.
- [2.37] V. G. Dubrovskii, N. V. Sibirev, N. N. Halder, and D. Ritter, “Classification of the Morphologies and Related Crystal Phases of III–V Nanowires Based on the Surface Energy Analysis,” *J. Phys. Chem. C*, vol. 123, no. 30, pp. 18693–18701, 2019.
- [2.38] J. A. Buck, *Fundamentals of Optical Fibers*, 2nd ed. Hoboken: John Wiley & Sons, Inc., 2004.
- [2.39] A. Yariv, *Optical Electronics*. Philadelphia: Saunders College Publishing, 1991.
- [2.40] A. W. Snyder and J. D. Love, *Optical Waveguide Theory*. New York: Chapman and Hall, 1983.
- [2.41] D. Marcuse, *Theory of Dielectric Optical Waveguides*, 2nd ed. San Diego: Academic Press Inc., 1991.
- [2.42] B. Wang and P. W. Leu, “Tunable and selective resonant absorption in vertical nanowires,” *Opt. Lett.*, vol. 37, no. 18, 2012, Art. no. 3756.
- [2.43] L. Cao, J. S. White, J. S. Park, J. A. Schuller, B. M. Clemens, and M. L. Brongersma, “Engineering light absorption in semiconductor nanowire devices,” *Nat. Mater.*, vol. 8, no. 8, pp. 643–647, 2009.
- [2.44] P. Krogstrup et al., “Single-nanowire solar cells beyond the Shockley–Queisser

- limit,” *Nat. Photonics*, vol. 7, no. 4, pp. 306–310, 2013.
- [2.45] S. K. Kim et al., “Tuning light absorption in core/shell silicon nanowire photovoltaic devices through morphological design,” *Nano Lett.*, vol. 12, no. 9, pp. 4971–4976, 2012.
- [2.46] K. M. Azizur-Rahman and R. R. LaPierre, “Wavelength-selective absorptance in GaAs, InP and InAs nanowire arrays,” *Nanotechnology*, vol. 26, no. 29, 2015, Art. no. 295202.
- [2.47] N. Anttu, “Absorption of light in a single vertical nanowire and a nanowire array,” *Nanotechnology*, vol. 30, no. 10, 2019, Art. no. 104004.
- [2.48] B. C. P. Sturmberg et al., “Optimizing Photovoltaic Charge Generation of Nanowire Arrays: A Simple Semi-Analytic Approach,” *ACS Photonics*, vol. 1, no. 8, pp. 683–689, 2014.
- [2.49] K. T. Fountaine, W. S. Whitney, and H. A. Atwater, “Resonant absorption in semiconductor nanowires and nanowire arrays: Relating leaky waveguide modes to Bloch photonic crystal modes,” *J. Appl. Phys.*, vol. 116, no. 15, 2014, Art. no. 153106.

3. Experimental and Simulation Methods

3.1. Sample Preparation

Nanowire (NW) samples begin with a 3-inch Si(111) wafer which is p-type doped with boron at a doping $> 2 \times 10^{19} \text{ cm}^{-3}$. The doping is necessary to produce photovoltaic devices but is not required for basic NW growth. The substrates are prepared for MBE growth by first growing a SiO_x layer using plasma-enhanced chemical vapor deposition (PE-CVD). The layer was generally in the range of 30 nm thick or less. The substrates then undergo an electron beam lithography (EBL) step. The wafer is first cleaned by sonicating in acetone and then IPA. The Si wafer is then spin-coated with AR-P 6200.3/Anisole 1:1 positive e-beam resist. The pattern transferred to the resist is a series of square pads composed of a triangular pattern of dots. The arrays of dots have pitches of 360 nm, 440 nm, 520 nm, 600 nm and 1000 nm. The diameters of the dots are controlled by the e-beam dosage, but final hole diameter will also depend on the etching conditions. The probe current and dosage combinations used are 500 pA and $10,000 \mu\text{Ccm}^{-2}$, 1 nA and $10,000 \mu\text{Ccm}^{-2}$, 5 nA and $10,000 \mu\text{Ccm}^{-2}$, 25 nA and $13,000 \mu\text{Ccm}^{-2}$, and 25 nA and $25,000 \mu\text{Ccm}^{-2}$. The final hole diameters have been measured as 57 nm, 57 nm, 71 nm, 87 nm and 101 nm, respectively, corresponding to the EBL parameters listed previously. This creates 25 different combinations of pitch and hole diameter. The positive resist allows for the pattern to be developed while the surrounding resist remains as a barrier to etching. After EBL is performed the pattern is etched into the oxide using reactive ion etching (RIE). This is performed under a CF_4 flow of 10 sccm and at a power of 100 W for 75 s. This is sufficient to remove the 30 nm oxide layer from the region of the holes (exposed pattern in the resist).

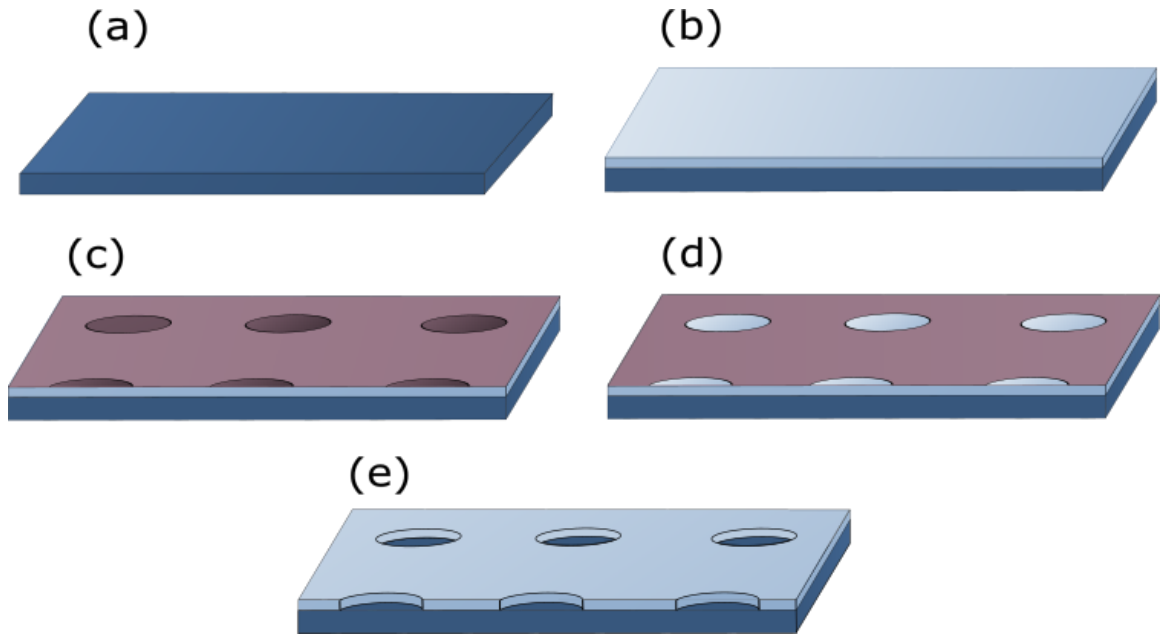


Figure 3.1. Wafer preparation prior to MBE growth. Preparation begins with (a) a clean, Si(111) wafer, followed by (b) growing a SiO_x oxide layer by PE-CVD. The wafer is then spin coated with a positive e-beam resist and (c) patterned with a series of dots via EBL before (d) being developed to remove the resist from the patterned regions. Lastly, (e) holes are etched into the oxide mask via RIE and the remaining resist is removed.

RIE is used as opposed to a wet etch at this stage because it produces anisotropic sidewalls as it removes oxide material. The remaining resist is then removed, and the wafer is cleaned a final time with acetone and IPA. The steps for producing a patterned wafer are shown schematically in Figure 3.1.

Once the substrate has been prepared the sample can be transferred to the MBE chamber for growth. Prior to loading the sample, the wafer is gently agitated in a 1% buffered hydrofluoric (BHF) solution for 25 s to remove any native oxide formed on the Si

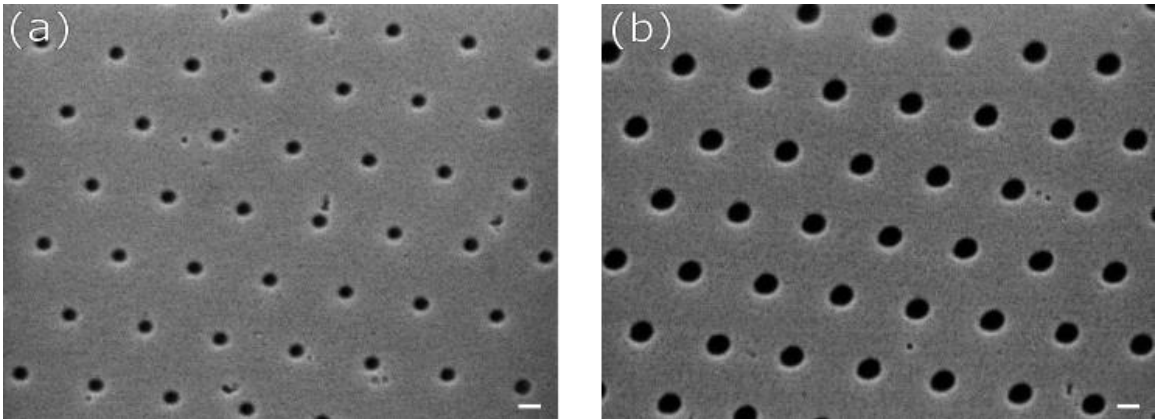


Figure 3.2. SEM images of etched holes in the oxide layer with a pitch of 360 nm where (a) was given a low e-beam dosage and (b) a high dose. Pinhole defects are also visible in the oxide layer. The scale bar is 100 nm.

at the bottom of the holes. It is then rinsed twice in DI water and immediately transferred to the MBE chamber. In the MBE chamber, the sample is degassed at 300°C and then undergoes an additional inductively coupled hydrogen plasma clean at 675°C. SEM images of the oxide holes are shown in Figure 3.2.

3.2. Molecular Beam Epitaxy

Molecular beam epitaxy (MBE) is a growth technique that uses beams consisting of atomic or molecular constituents to grow thin films. Effusion cells are used to evaporate materials, such as Ga at high temperatures. In a gas-source MBE system, As₂ and P₂ atoms are supplied from gas sources (AsH₃ and PH₃). The gases are cracked at a high temperature to produce predominantly dimers of the group V material. The rate of deposition can be controlled by the temperature of the cell or by opening and closing the shutter on the atomic

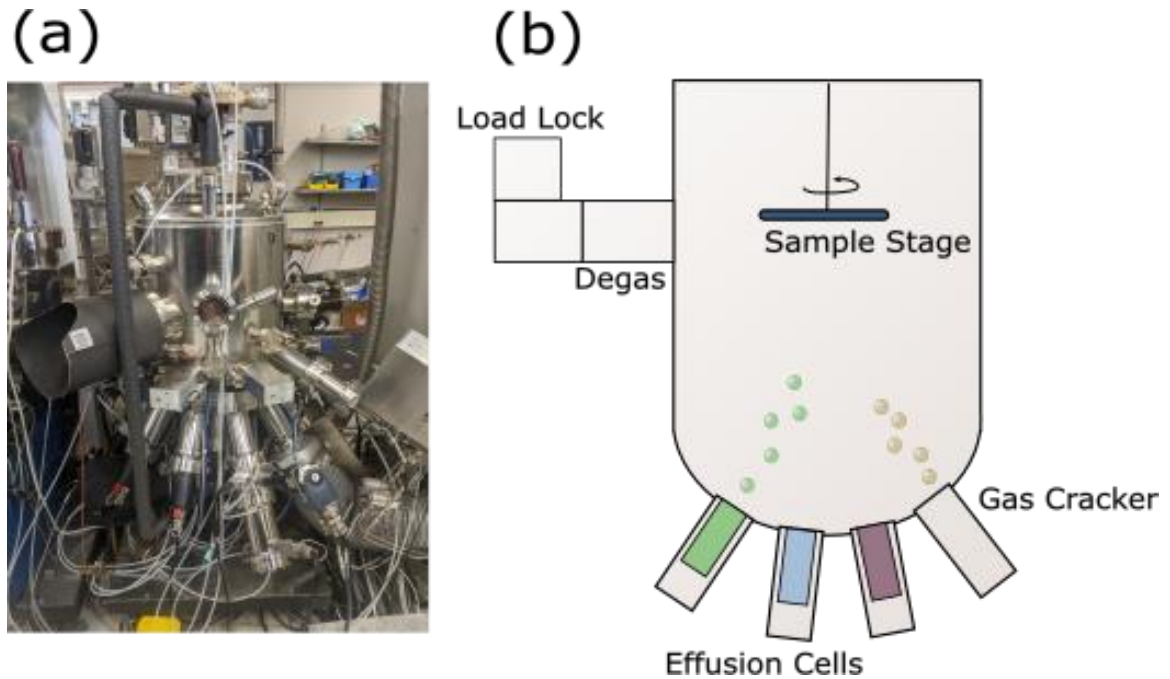


Figure 3.3. (a) The MBE chamber at McMaster University's Centre for Emerging Device Technologies. (b) A labelled schematic of the same system.

beams. Note that traditional growth of GaAs crystalline thin films tends to be As rich and Ga limited [3.1], whereas self-catalyzed NW growth is always Ga rich and As limited. A photo of the MBE system at McMaster University is shown in Figure 3.3 (a) and a labelled diagram of the system is shown in Figure 3.3 (b).

NW growth begins with the formation of a Ga droplet inside the oxide holes. This step can be assisted by first only opening the Ga shutter so that Ga may collect at the bottom of the hole and form droplets without the presence of As_2 . During MBE growth, the Ga rate is kept at a constant 2D equivalent growth rate of $0.125 \mu\text{m/h}$ while the As_2 flux is altered to produce different V/III flux ratios. This allows for NW diameter control. The droplet can be consumed at the end of the growth process by shuttering the Ga cell and

only allowing As₂ to enter the chamber. These growth conditions will be explored in later chapters of this thesis.

3.3. Characterization

3.3.1. Scanning Electron Microscopy

Scanning electron microscopy (SEM) is an imaging technique capable of nanometer spatial resolution. A current is applied to an atomically sharp Schottky field emission gun which strips electrons from the tip of the probe and forms a beam which is focused on the object. The beam is scanned, or rastered, across the surface of the sample. The electron beam interacts with the sample to produce two main classes of electrons: backscattered electrons and secondary electrons. Backscattered electrons have a higher energy and are produced when the incident beam is scattered due to interactions with the atomic nuclei of the sample. Secondary electrons are produced when the atoms of the sample are ionized. These secondary electrons are collected at a detector and provide a high resolution image of the surface of the sample [3.2].

Samples were analyzed in a JEOL7000F scanning electron microscope. Due to the conduction properties of semiconducting materials, they do not normally need to be coated with a conductive material to be adequately imaged. Samples were mounted to aluminum stubs. The JEOL7000F has a maximum tilt angle of 70°. For cross-sectional SEM images, the sample was first cleaved down the centre so that NWs are close to the edge for easy visualization. The sample is then mounted to the stub at 90° and secured with a conductive nickel paste.

3.3.2. Transmission Electron Microscopy

Transmission electron microscopy (TEM) offers higher resolution than SEM. The electron beam is transmitted through the sample. Samples must be very thin and dispersed on a grid so that the beam can pass through. The technique can be used to see features in greater detail or can be used to gather information on a sample's atomic composition.

Scanning transmission electron microscopy (STEM) focuses the electron beam and rasters it across a small portion of the sample like SEM. The sample can be imaged in bright field (BF) mode where the transmitted beam is detected, or dark field (DF) mode where the transmitted beam is removed from the image. An annular dark field detector is used to collect scattered electrons. High angle annular dark field (HAADF) imaging is particularly useful for identifying elements of the sample. The relative contrast in the image will vary with the atomic Z-number in this mode [3.3].

Sample preparation for TEM involved cleaving off a desired portion of the NW sample. This portion was then placed in a small vial and covered with isopropyl alcohol (IPA). The vial was then placed in a beaker of deionized water (small enough to keep it upright) and sonicated for at least 3 min. This broke the NWs off the substrate and suspended them in the IPA. Using a pipette, droplets of the solution were dropped onto a holey carbon grid. This was done one droplet at a time and the solution of IPA was allowed to evaporate before subsequent droplets were placed on the grid. A gentle flow of nitrogen could be used to speed up the evaporation process. Between 20 and 30 droplets were usually applied. The number of droplets applied depended on the yield of the sample with

more droplets being needed to transfer a useful number of NWs to the grid. A JEOL 2010F microscope was used for TEM imaging as well as HAADF STEM imaging.

3.4. Finite Element Method

The finite element method (FEM) is a numerical approach to solving partial differential equations. The geometry of the problem is discretized using a mesh and the solutions to the equations are solved at the nodes of the mesh.

The basic model used in this thesis is similar to that used in Ref. [3.4]. However, it has been updated to work with the RF module of COMSOL 5.3A simulation software [3.5]. A standard operating procedure (SOP) describing the setup and tips for performing these simulations can be found in the Appendix.

The main equation which must be satisfied on the geometric domain is the wave equation:

$$\nabla^2 \times \vec{E} - k_0^2 n^2 \vec{E} = 0 \quad (3.1)$$

where \vec{E} is the electric field vector, k_0 is the vacuum wavevector ($k_0 = 2\pi/\lambda$), and n is the complex refractive index of the material. The complex refractive index is wavelength dependent and is interpolated from data found in Ref. [3.6]. The incident light source is simulated using a periodic port boundary placed above the vertical NW structure. The light propagates parallel to the axis of the NW. The port power is set to 1 W when only the relative amount of absorption, reflectance, and transmittance is desired. When calculations of photocurrent are needed, the incident power is set based on the irradiance of the AM1.5D solar spectrum. The data for this spectrum can be found in Ref. [3.7].

The boundary conditions are set to have “Floquet” periodicity to simulate an infinite array of NWs. This boundary is applied in the x and y directions to simulate a square array of NWs. Although a triangular array is used in experimental work to provide close packing of the NWs, the square array is easier to set-up for the simulations and is justified since small changes in the NW pitch or packing of the array is not expected to change the outcome of the simulation significantly. Likewise, the simulations are performed on cylindrically symmetric NWs for ease of set-up instead of hexagonally faceted NWs. In simulations designed to observe the absorption in the NW arrays, the cross-sectional area of the NW plays the most important role regardless of the shape. A change in the cross-sectional shape will result in a minimal change to the cross-sectional area and is only expected to shift the absorption spectra a small amount [3.4, 3.8]. Different NW cross-sectional shapes can be represented as circular with an equivalent cross-sectional area.

At the bottom and top of the simulation space, perfectly matched layers (PMLs) are placed. These PMLs act like absorbing layers that absorb all incident light with minimal reflection, particularly for normally incident waves. These layers prevent reflection from the base and the top of the domain geometry. The simulation geometry is shown in Figure 3.4.

The reflectance, transmittance, and absorptance are the main quantities of interest in these simulations. Reflectance and transmittance are calculated by integrating the Poynting vector, the power flow, over a boundary plane. The integration for reflectance is done over a plane directly below the uppermost PML layer and above the port boundary.

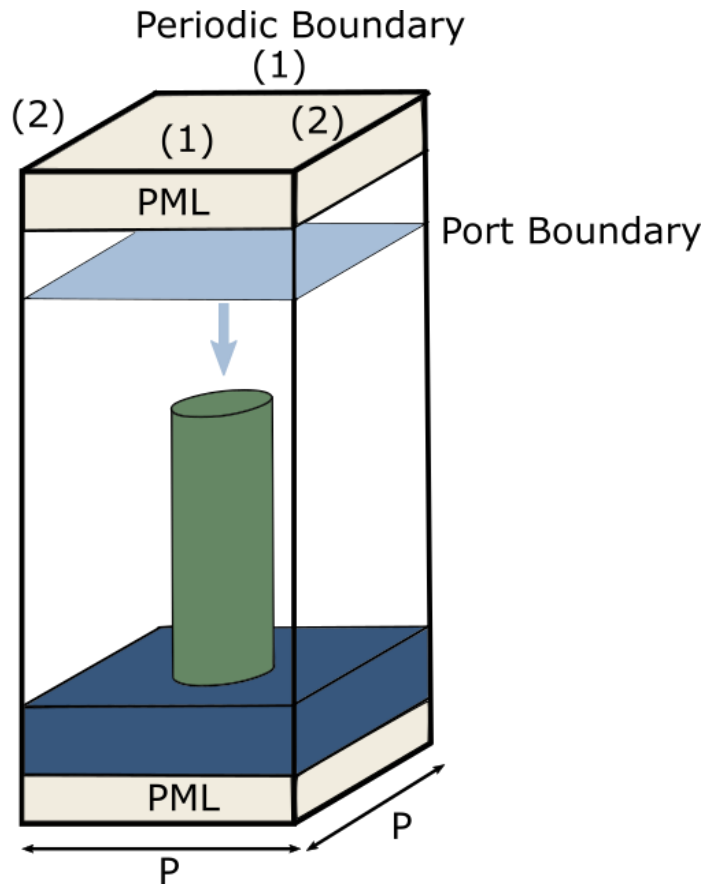


Figure 3.4. Basic schematic of the simulation geometry, showing perfectly matched layers (PMLs) at the top and bottom of the simulation geometry. Period boundary conditions are specified in pairs labelled (1) and (2) and apply to the outer sides. A port boundary is placed above the NW but below the uppermost PML and directs a plane wave downwards on the NW. The pitch, P , defines the size of the unit cell.

The integration for transmission is performed at the top of the bottommost PML if the total is needed, or at the top of the substrate if only the contribution from the NW absorption is needed. If the incoming power is normalized to 1 then the absorptance can be calculated as:

$$A = 1 - R - T \quad (3.2)$$

where A is the absorptance, R is the reflectance through the top boundary, and T is the transmittance through the bottom boundary.

For simulations where the incoming light has power weighted to the solar spectrum, a volume integral over the NW can be performed to obtain the photocurrent according to:

$$J = \frac{e}{P^2} \int \frac{\epsilon_0}{\hbar} |\vec{E}|^2 nk dV \quad (3.3)$$

where e is the fundamental charge, P is the pitch, ϵ_0 is the permittivity of free space, \vec{E} is the electric field, n and k are the real and imaginary components of the refractive index, and dV is the volume element.

A description of the model setup is provided in the Appendix.

3.5. References

- [3.1] J. Orton and T. Foxon, “4. Fundamentals,” in *Molecular Beam Epitaxy: A Short History*, 2015.
- [3.2] W. Zhou, R. Apkarian, Z. L. Wang, and D. Joy, “Fundamentals of scanning electron microscopy,” in *Scanning Microscopy for Nanotechnology: Techniques and Applications*, W. Zhou and Z. L. Wang, Eds. New York: Springer, 2007, pp. 1–40.
- [3.3] S. J. Pennycook et al., “Scanning transmission electron microscopy for nanostructure characterization,” in *Scanning Microscopy for Nanotechnology: Techniques and Applications*, W. Zhou and Z. L. Wang, Eds. New York: Springer, 2007, pp. 152–190.

- [3.4] K. M. Azizur-Rahman, “Simulation of III-V Nanowires for Infrared Photodetection,” McMaster University, 2016.
- [3.5] COMSOL Inc., “RF Module: User’s Guide.” COMSOL, pp. 1–224, 2017.
- [3.6] E. D. Palik, Handbook of Optical Constants of Solids. Washington: Academic Press Inc., 1985.
- [3.7] National Renewable Energy Laboratory (NREL), “Reference Air Mass 1.5 Spectra.” [Online]. Available: <https://www.nrel.gov/grid/solar-resource/spectra-am1.5.html>. [Accessed: 01-Jan-2021].
- [3.8] A.-L. Henneghien, B. Gayral, Y. Désières, and J.-M. Gérard, “Simulation of waveguiding and emitting properties of semiconductor nanowires with hexagonal or circular sections,” J. Opt. Soc. Am. B, vol. 26, no. 12, pp. 2396–2403, 2009.

4. Effect of Ga Pre-Deposition on Nanowire Yield and Diameter

4.1. Summary

This chapter presents work from the paper titled “Improving the yield of GaAs nanowires on Si by Ga pre-deposition” (D. P. Wilson, V. G. Dubrovskii, and R. R. LaPierre, *Nanotechnology*, vol. 32, no. 26, 2021, Art. no. 265301. DOI: 10.1088/1361-6528/abef93). This work examined the relationship between the initial conditions of MBE-grown Ga seeded nanowires (NWs) and the resulting yield and diameter. A pre-deposition step was used to seed the NWs. The Ga shutter was opened without the presence of As₂ or P₂ in the MBE chamber. All NWs began with a short segment of GaP which has been shown to improve yield before transitioning to GaAs. This method should apply equally well to all Ga seeded NWs. Pre-deposition times ranged from 0 s to 500 s. Yield saw dramatic changes from under 20% to nearly 100% depending on the hole diameter and pre-deposition time. The NW diameter was examined using SEM and HAADF STEM and was found to be affected by VS growth along the sidewalls of the NW.

The explanation for the trends in the yield was supported by a numerical model derived in collaboration with Vladimir Dubrovskii from St. Petersburg State University. The model considered the filling of the hole with Ga atoms in the pre-growth stage. In the ideal case, the volume of liquid Ga would be equal to the available volume of the oxide hole, however thin residual oxide layers can impede the collection of Ga which alters the ideal pre-deposition time depending on the hole diameter.

4.2. Introduction

Nanowires (NWs) have shown promise in many optoelectronic device applications due to their unique properties. For example, the absorption spectrum of vertically standing III-V semiconductor NWs can be tuned by NW diameter due to resonant light absorption, thereby enabling broadband light absorption for photovoltaics or multi-spectral absorption for photodetectors [4.1-4.5]. These applications demand a high NW yield and control of the NW diameter, length and period (spacing between NWs). III-V NWs can be grown by the self-assisted vapor-liquid-solid (VLS) method whereby a metal droplet (containing an element of the NW itself) nucleates and sustains growth of the NWs (e.g., Ga droplets for growth of GaAs NWs) [4.6]. Furthermore, the position of NWs can be controlled by selective-area epitaxy using a patterned oxide mask, resulting in a periodic array of vertically standing NWs [4.6].

NW diameter can be controlled by the droplet size during self-assisted NW growth; e.g., the Ga droplet for self-assisted GaAs NWs. The droplet size can be controlled by adjusting the Ga flux that the droplet receives. This can be accomplished directly by adjusting the V/III flux ratio during growth [4.7-4.12]. High V/III flux ratio shrinks the droplet by consuming Ga into GaAs crystal, resulting in positively tapered NWs until complete consumption of the droplet. Conversely, as the V/III flux ratio is lowered, the droplet volume expands and the morphology of the NW can change from positive-tapered to straight or inverse-tapered.

A secondary flux of Ga desorbing from the oxide mask can impinge on the droplet or NW sidewalls [4.13]. This re-emitted flux increases with NW pitch; i.e., with the surface

area surrounding each NW. As a result, self-assisted NW arrays with large pitches often show an inverse tapered effect which is not present for smaller pitches grown under the same conditions [4.7, 4.13]. Thus, the NW pitch offers another method of controlling the Ga droplet dynamics.

Herein, we employ the self-assisted selective-area growth method in a molecular beam epitaxy (MBE) system to grow GaAs NWs. This article presents a study of Ga pre-deposition as a method to control the yield and diameter of GaAs NWs. The dependence of NW yield, dimensions (diameter, length) and morphology on oxide hole diameter, array pitch and Ga pre-deposition duration are investigated.

4.3. Experimental Details

GaAs NWs were grown by selective-area epitaxy (SAE) in a gas source molecular beam epitaxy (GS-MBE) system by the self-assisted VLS method (i.e., using a Ga droplet). A 30 nm layer of SiO_x was deposited on Si (111) substrates by plasma-enhanced chemical vapour deposition (PE-CVD). The SiO_x was patterned by electron beam lithography (EBL) into hexagonal arrays of holes with five different pitches (360, 440, 520, 600 and 1000 nm) and five hole diameters (57 ± 9 , 57 ± 6 , 71 ± 5 , 87 ± 6 and $101 \text{ nm} \pm 4 \text{ nm}$). The 57 nm hole diameter was repeated to check the reproducibility of the results. Hole diameter was controlled by adjusting the electron beam dose and measured by scanning electron microscopy (SEM). Reactive ion etching and a final HF dip was used to open the holes prior to NW growth. Further details on the substrate preparation method is available in Ref. [4.7, 4.14].

A Ga pre-deposition step was implemented prior to NW growth where the Ga shutter was opened without group V flux. The Ga pre-deposition duration was 0 s (no Ga pre-deposition), 250 s, or 500 s. Following the Ga pre-deposition step, NW growth was started by initiating the group V flux. All NWs began with a GaP segment which has also been shown to improve overall yield; i.e., the fraction of holes filled with a single vertically standing NW [4.14]. The GaP segment was grown for 25 min before changing the P₂ flux to As₂ over the course of 5 min. A GaAs segment was then grown for 100 min. The substrate temperature was 600 °C, the equivalent Ga impingement rate (corresponding to 2D growth rate of GaAs) was 0.125 mm/h, and V/III flux ratio was 2 throughout growth.

To further study the growth dynamics, GaAs_{0.8}P_{0.2} marker layers were introduced periodically during growth of the GaAs segment for observation by scanning transmission electron microscopy (STEM), allowing inspection of the growth progression. Marker layers were added to the GaAs segment in groups of three with the first GaAsP layer grown for 45 s and the following two grown for 30 s. Each set of GaAsP marker layers were separated by 5 min of GaAs growth. The growths were terminated by supplying only As₂ flux to the sample for 20 min at the growth temperature and then allowing the sample to cool under As₂ to consume the Ga droplet [4.10].

NW morphology and yield were examined using a JEOL JSM-7000F SEM operated at 5 kV. Marker layers were examined by STEM using high angle annular dark field (HAADF) imaging on a JEOL 2010F operated at 200 kV. STEM samples were prepared by sonicating the NW sample in isopropyl alcohol (IPA) followed by dispersion on a Cu grid.

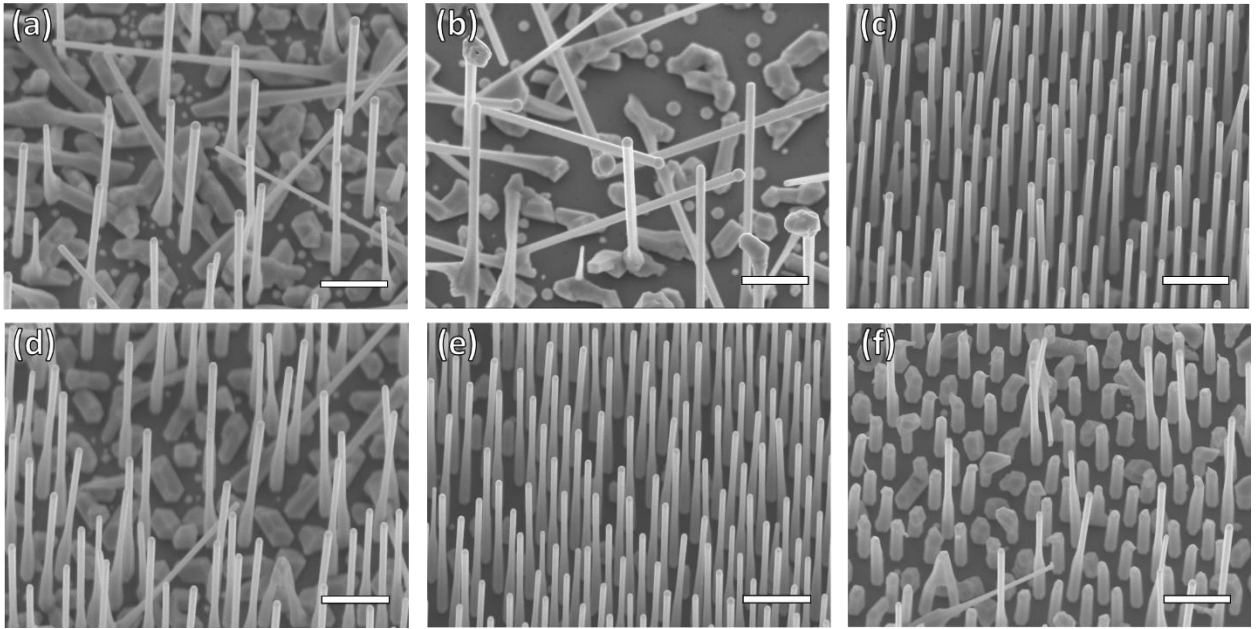


Figure 4.1. 20° tilted SEM images of NWs with (a, d) 0 s, (b, e) 250 s, and (c, f) 500 s of Ga pre-deposition. Pattern pitch was 520 nm and hole diameter was (a-c) 57 nm and (d-f) 101 nm. Scale bars are 1 μm.

4.4. Results and Discussion

4.4.1. Effect of Ga Pre-Deposition on Yield

First, the effect of the Ga pre-deposition step on the NW yield was examined by SEM. Figure 4.1 shows representative SEM images of NW arrays grown with different Ga pre-deposition durations. The data associated with the 57 nm hole diameter were obtained from two different NW arrays on the substrate with identical hole size, confirming the reproducibility of the results. Figure 4.2 shows the NW yield (the number of holes that produce a vertical NW) as obtained from SEM analysis of the NW arrays. For the large hole diameters (Figure 4.1d-f), the yield was observed to improve as the Ga pre-deposition

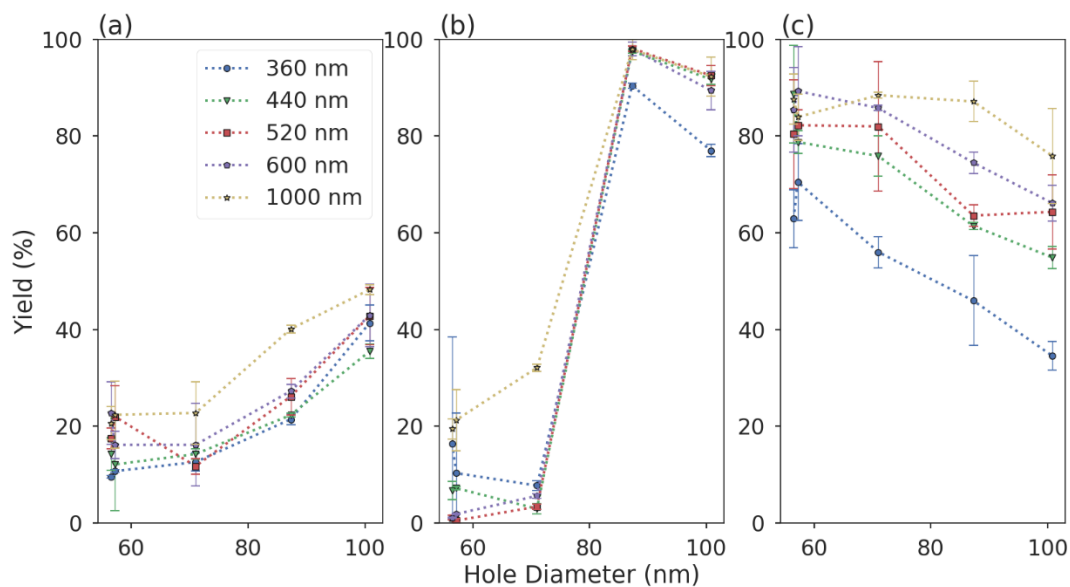


Figure 4.2. NW yield with (a) 0 s, (b) 250 s and (c) 500 s of Ga pre-deposition. The legend indicates the different pitches.

increased from 0 s to 250 s, but then declined for 500 s. For the smaller hole diameters (Figure 4.1a-c), the yield did not improve until 500 s of Ga pre-deposition. Poor yield was generally attributed to crystallites growing in the holes or tilted NWs. In addition, there was a trend of slightly increasing NW yield with pitch (see Supporting Information). These results, summarized in Figure 4.2, indicate that it is possible to achieve a high NW yield with a Ga pre-deposition step, but with a strong dependence on the hole diameter and a weaker dependence on the pitch. The NW length was not strongly influenced by hole diameter or pitch (see Supporting Information)

An improvement in NW yield has generally been observed with short Ga pre-deposition (generally, 120 s or less), followed by a decrease in yield as the pre-deposition

duration is increased further [4.7-4.9, 4.15, 4.16]. Small variations in substrate conditions, such as thermal oxide remaining in the holes, can also significantly impact the yield [4.15, 4.17]. In our case, SEM images of the samples with small hole diameters and no pre-deposition step showed crystallites or tilted NWs, as seen in Figure 4.1a and b, which often indicates a thin layer of SiO_x remaining at the bottom of the hole that impedes the growth of NWs [4.6, 4.11, 4.15, 4.18]. In some cases, the oxide may form a bowl-shaped layer in the holes which decreases the area accessible to the Si substrate [4.6]. In extreme cases, the Ga must etch a pinhole through the oxide layer for epitaxial growth with the Si substrate to occur [4.18]. The presence of an oxide layer will slow the rate of Ga collection, leading to smaller diameter droplets or no droplets at all [4.18, 4.19]. Additionally, oxide layers have been shown to increase the contact angle of the Ga droplet which can result in NW tilting if the angle becomes much greater than 90° [4.20, 4.21]. Similar to these prior observations, we speculate that SiO_x may remain at the bottom of our holes, especially for the smaller hole diameters, resulting in a low NW yield. For the smaller holes, the NW yield improves only with a relatively long (500 s) Ga pre-deposition duration that effectively etches the oxide remaining at the bottom of the holes [4.18]. Conversely, larger hole diameters, presumably with less oxide at the bottom, can improve the NW yield with only 250 s of Ga pre-deposition. With continued Ga pre-deposition, larger contact angles and over-filling of the oxide holes can reduce the yield with the formation of crystallites and tilted NWs [4.16, 4.21]. Another possibility for having lower Ga sticking within smaller holes could be the shadowing effect originating from blocking a part of the Ga flux

into the holes by the oxide mask, which is definitely the case for As. A detailed model discussing these effects is presented below.

Figure 4.2 also shows a trend of greater NW yield with increasing pitch. Our previous studies [4.7] have shown that the droplet of some NWs become insufficient to sustain NW growth, leading to instabilities such as kinked NWs. In extreme cases, droplets can become completely consumed, leading to crystallites. Arrays with larger pitches provide a larger surface area between the NWs for scattered flux that contribute to the NW droplet volume, thereby reducing droplet instabilities and improving NW yield.

4.4.2. Effect of Ga Pre-deposition on Morphology

Morphology was assessed by SEM measurements of the diameter at the top and base of the NWs for 0 s, 250 s and 500 s of Ga pre-deposition. Figure 4.3 shows the results of these measurements plotted against hole diameter for each array pitch. A larger overall NW diameter might be expected as the Ga pre-deposition duration increases; i.e., the NW diameter correlates with the droplet diameter. However, Figure 4.3 indicates that the top and base diameter of the NWs did not strongly correlate with increasing Ga pre-deposition. A similar observation was reported in Ref. [4.20]. Indeed, due to radius stabilization [4.22], all NWs can be expected to approach the same diameter over time regardless of starting diameter. On the other hand, the base diameter (solid lines in Figure 4.3) was usually larger than the top diameter (dashed lines), indicating a slightly positive-tapered NW morphology as evident in Figure 4.1. Comparing Figure 4.3a-e, there is also a slight increase in the base diameter as the pitch increases. The latter observations can be attributed to VS deposition

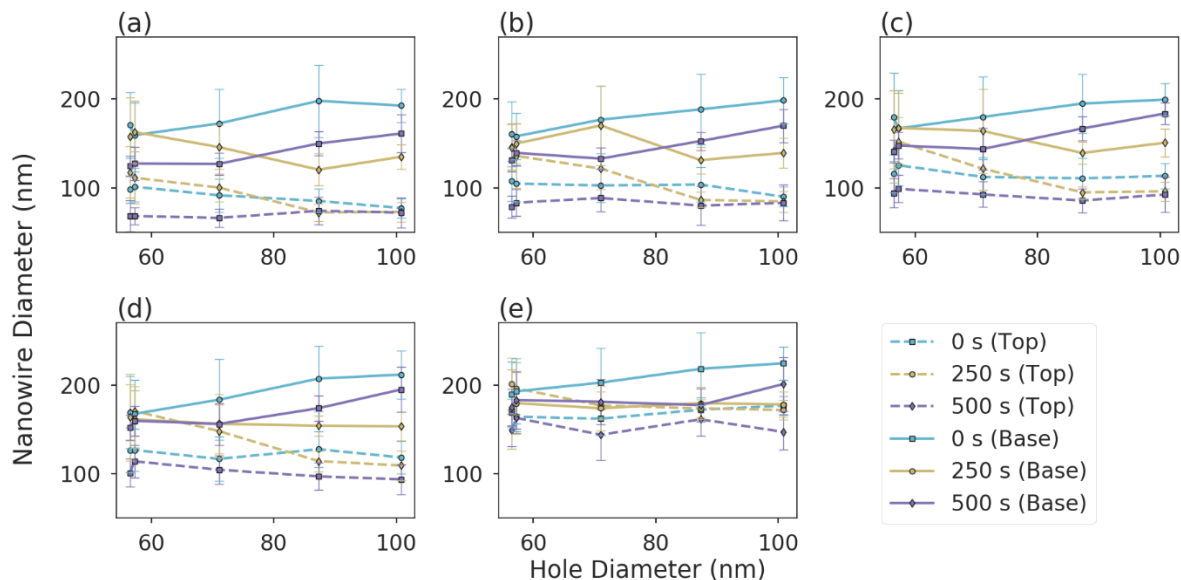


Figure 4.3. Diameter at the top and base of NWs with respect to hole diameter for pitches of (a) 360 nm, (b) 440 nm, (c) 520 nm, (d) 600 nm, and (e) 1000 nm. Legend indicates the Ga pre-deposition duration of 0, 250 and 500 s. Dashed lines indicate the top NW diameter and solid lines indicate the base diameter.

on the NW sidewalls with a greater flux of Ga re-emitted from the oxide mask or neighboring NWs for larger pitches [4.13]. Thus, under the present growth conditions, the diameter of NWs is dominated by VS growth on the NW sidewalls [4.6, 4.16, 4.20, 4.23], rather than the size of the Ga droplet. Figure 4.3 shows that the NWs without pre-deposition (0 s) showed a slightly wider base as compared to 250 and 500 s of pre-deposition. This may be due to increased VS deposition in the 0 s samples, where the lower NW yield causes less competition with neighboring NWs (effectively increasing the pitch).

To further verify VS deposition, the NWs were investigated by inspecting the GaAsP marker layers in STEM. STEM images of NWs grown with 0, 250 and 500 s of Ga

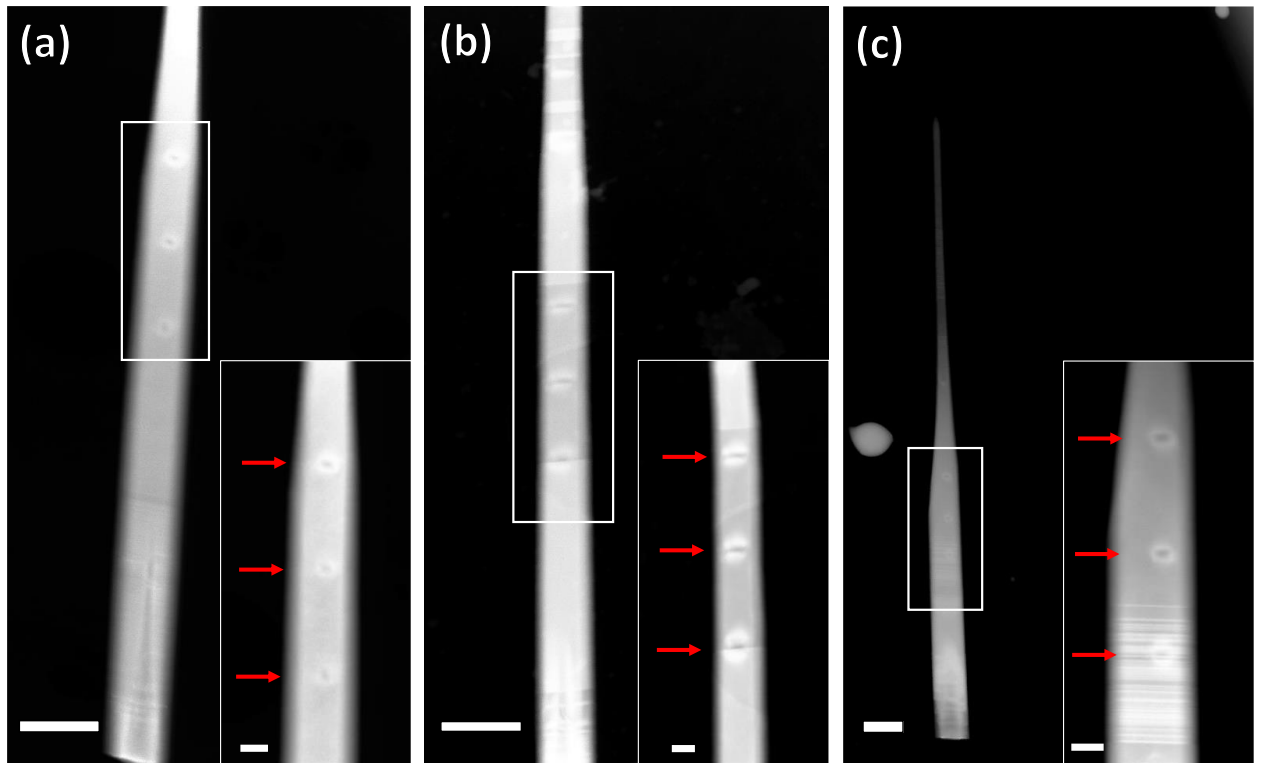


Figure 4.4. STEM images of NWs taken from samples with (a) 0 s, (b) 250 s and (c) 500 s of Ga pre-deposition. The boxes indicate the area of the higher magnification images in the insets. Scale bars are 200 nm on the main panels and 50 nm for the insets. The red arrows indicate the positions of the marker layers. Note that the bottom marker layer in (b) and (c) is obscured by stacking faults in the NW.

pre-deposition are shown in Figure 4.4. In all instances, the marker layers (indicated by red arrows in the insets of Figure 4.4) do not extend across the entire NW diameter, providing evidence for radial VS growth on the NW sidewalls. More heavily tapered NWs, such as that in Figure 4.4c, showed greater radial growth. For the growth conditions investigated here, the effects of VS growth had a more prominent effect on NW morphology than the Ga pre-deposition duration.

4.4.3. Model

As discussed above and studied in detail in Refs. [4.24-4.26], the maximum yield of vertical III-V NWs grown by MBE in patterned holes in $\text{SiO}_x/\text{Si}(111)$ is achieved when group III droplets in the holes are neither too small nor too large. Underfilled holes usually produce irregular GaAs crystallites or tilted NWs because the droplet wets asymmetrically one edge of the hole. Ga droplets in overfilled holes may keep the hole diameter by increasing the contact angle, but finally start crawling out of the holes onto the oxide surface, which also decreases the yield. Evolution of a Ga droplet inside the hole of a given radius and depth is illustrated in Figure 4.5a. According to Ref. [4.26], the maximum yield corresponds to the complete filling of the hole where the Ga droplet volume V_{Ga} approximately equals the hole volume V_{hole} . Due to the ability of the droplet to maintain the filling by increasing its contact angle before extending onto the mask, a slight overfilling should be less critical than underfilling.

With our 2D equivalent impingement rate of GaAs of $0.125 \mu\text{m}/\text{h} = 0.0347 \text{ nm}/\text{s}$, the deposition rate of Ga v_{Ga} equals $0.0154 \text{ nm}/\text{s}$. The coefficient is given by the ratio of the elementary volume of liquid Ga (0.02 nm^3) over the elementary volume of GaAs (0.0452 nm^3). The thickness of deposited Ga equals 3.84 nm in 250 s and 7.68 nm in 500 s . These values are too small compared to the hole depth H_{hole} of $\sim 30 \text{ nm}$, and would be further reduced by the shadowing effect as discussed below. Therefore, the filling process must be enhanced by surface diffusion of Ga adatoms from the oxide surface into the holes.

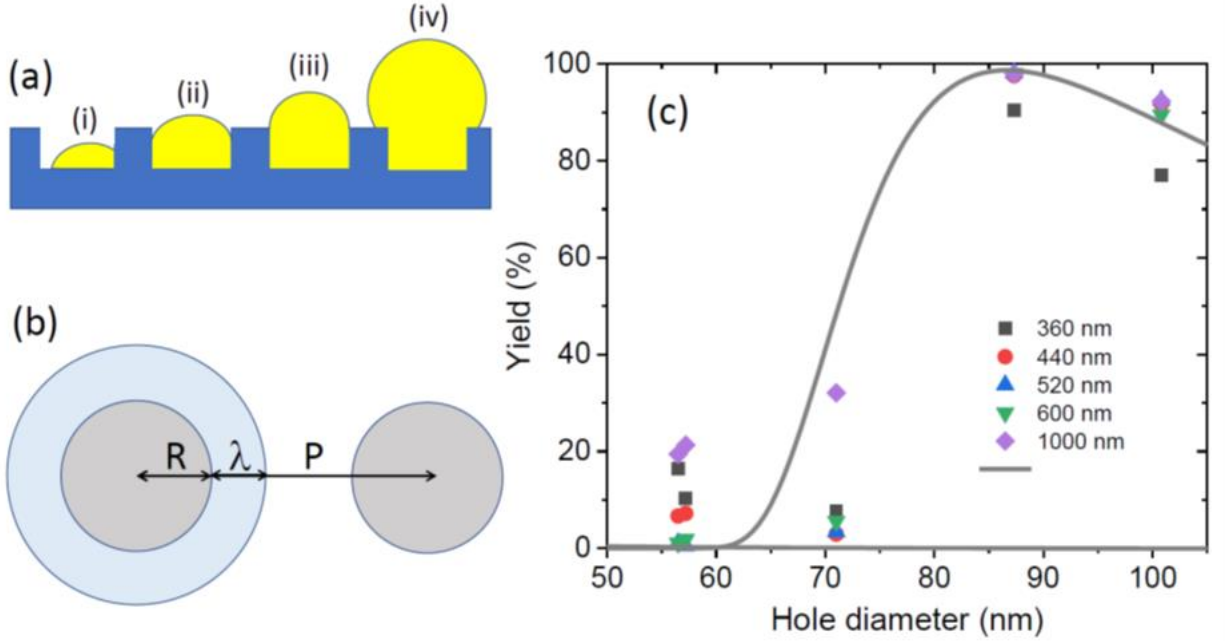


Figure 4.5. (a) Schematics showing the Ga droplet evolution in a hole: (i) underfilled hole with asymmetric wetting of the sidewalls. (ii) Optimally filled hole with $V_{Ga} \cong V_{hole}$. (iii) Slightly overfilled hole where the droplet maintains the hole size by increasing its contact angle. (iv) Overfilled hole with Ga droplet crawling out onto the mask. (b) Ga collection area whose radius $R + \lambda$ is smaller than $P/2$. (c) Fit of the yield versus the hole diameter with 250 s of Ga pre-deposition, obtained from Eq. (4.2) and (4.3).

Assuming that Ga atoms are collected from the surface area $\pi(R + \lambda)^2$, where R is the hole radius and λ is the diffusion length of Ga adatoms on the oxide surface, the droplet volume is:

$$V_{Ga} = \alpha(R)v_{Ga}\pi(R + \lambda)^2t \quad (4.1)$$

with t as the Ga pre-deposition time. Here, $\alpha(R)$ is the fraction of Ga atoms available for growth of the droplet and $1 - \alpha(R)$ is the fraction of Ga atoms which is lost for growth.

This expression is valid when $R + \lambda < P/2$, where P is the pitch (Figure 4.5b). In this case, different holes are not competing for the Ga diffusion flux and we completely ignore the influence of the pitch on the Ga volume. Hence, a trend of increasing yield with pitch is considered here as a secondary effect and we only study the yield as a function of the hole size.

Dividing Eq. (4.1) by the hole volume $V_{hole} = \pi R^2 H_{hole}$, we obtain:

$$\frac{V_{Ga}}{V_{hole}} = \alpha(R) \frac{v_{Ga}t}{H_{hole}} \left(1 + \frac{\lambda}{R}\right)^2 \quad (4.2)$$

Here, $v_{Ga}t$ is the thickness of deposited liquid Ga film, $(1 + \lambda/R)^2$ is the magnifying factor due to Ga surface diffusion, and $\alpha(R)$ is the suppression factor due to a thin layer of oxide remaining in smaller holes. According to the model, the maximum yield corresponds to $V_{Ga}/V_{hole} = 1$. We note that the ratio V_{Ga}/V_{hole} decreases with increasing hole radius at an R -independent α , in which case smaller holes would be filled earlier than the larger ones. According to Figures 4.1 and 4.2, this trend is reversed, meaning that $\alpha(R)$ decreases toward smaller R due to the presence of residual oxide in smaller holes.

Assuming that $\alpha = 1$ in the largest holes with $R = 50.5$ nm and using the data shown in Figure 4.2b (where the maximum yield of ~100% is observed at $R = 43.5$ nm), we estimate the Ga diffusion length at $\lambda = 97$ nm. This λ satisfies the inequality $R + \lambda < P/2$ in the entire range of investigated pitches and hole diameters. A linear increase of α with R is fitted by $\alpha(R) = 0.03R - 0.55$ if R is measured in nm. The factor $\alpha(R)$ decreases from ~1 at $R = 50.5$ nm to 0.3 at $R = 28.5$ nm, meaning that 70% of Ga atoms are re-evaporated from the smallest holes while etching the residual oxide layer.

We assumed that the lost fraction of Ga atoms is spent to etch a pinhole through the residual oxide layer as discussed above. More investigations are required to accurately verify this effect, which is beyond the scope of this work. We noticed that the direct impingement of Ga into the pinholes is insufficient for their filling. The additional diffusion flux is described by the effective diffusion length λ in Eq. (4.1), meaning that Ga atoms are collected from the surface area $\pi(R + \lambda)^2$. Without Ga diffusion from the oxide surface, the direct Ga flux would be collected from the reduced area due to the shadowing effect. Shadowing of the As flux into the holes by the mask and its role in nucleation of GaAs NWs is discussed in Ref. [4.26]. Shadowing depends on the beam angle α in the directional MBE technique. In our MBE, $\alpha = 35^\circ$ for both As and Ga beams. If the Ga sticking on the oxide surface were zero, as in the case of As, the suppression of Ga collection in the smallest holes (with $R_{min} = 28.5$ nm) with respect to the largest holes (with $R_{max} = 50.5$ nm) would be given by the factor $\sim [(2R_{min} - H\tan\alpha)/(2R_{max} - H\tan\alpha)]^2 \cong 0.25$. This is close to the obtained estimate ($\alpha_{min} = 0.3$). However, due to surface diffusion that brings Ga adatoms from the mask surface into the holes, the shadowed fraction of the Ga flux is not lost.

In the absence of better qualitative information, we use the double exponential dependence [4.27] of the NW yield y on the ratio V_{Ga}/V_{hole} :

$$y \propto \exp(cx - e^{cx}), \quad x = 1 - V_{Ga}/V_{hole}, \quad (4.3)$$

Here, the asymmetric shape of the curve allows us to describe a slower decrease of the yield in the overfilled holes, while c is a parameter giving the width of the yield distribution over differently sized holes. Figure 4.4c shows the fit to the data at $t = 250$ s, obtained

with Eq. (4.2) and (4.3) at $c = 11$. This value of c is chosen to fit the observed distribution width. The fit is not perfect and cannot be better as it ignores several ingredients such as the influence of pitch on the evolution of NW droplets and the role of hole aspect ratio [4.26] but reflects well the main effect. At a given time of Ga pre-deposition, the yield reaches its maximum (almost 100%) at a certain hole size corresponding to the optimal filling of the holes, decreases steeper toward smaller holes due to underfilling and more smoothly toward larger holes due to overfilling.

Our experiments were carried out at a substrate temperature of 600 °C. The diffusion length of Ga adatoms on the oxide surface is temperature dependent and is expected to strongly decrease for higher temperatures. Therefore, the filling process should take longer times at higher temperatures for a given size of the pinholes.

4.5. Conclusions

We have studied the effects of Ga pre-deposition on the NW yield and diameter. Increasing the Ga pre-deposition duration (up to 500 s) improved the NW yield. The improvement to the yield was strongly affected by the diameter of the holes in the oxide layer. Relatively short (250 s) pre-deposition durations were effective at improving the yield for large hole diameters, while longer (500 s) durations were required for small hole diameters. We suggest that a thin layer of oxide impedes the formation of droplets, especially in the small holes. According to the model, the hole filling with liquid Ga is enhanced by surface diffusion of Ga adatoms from the oxide surface, with a Ga diffusion length of 97 nm at 600 °C. On the other hand, the growth rate of Ga droplets is suppressed

in smaller holes by the residual oxide. Ga evaporation takes about 70% of atoms in the smallest 57 nm diameter holes. As a result, the optimal filling was reached with shorter Ga pre-deposition times in larger holes. The NW diameter was not strongly affected by the Ga pre-deposition duration. Instead, the positive tapering and STEM of marker layers indicated the presence of VS growth on the NW sidewalls.

4.6. Supplementary Materials

Late stage nanowire (NW) growth can be strongly affected by shadowing effects. As NWs grow longer, the flux of As and Ga may be limited due to geometric effects related to the angle of the beam, the height of the nanowires and the pitch. These shadowing effects can result in shorter NW lengths [4.13]. Figure 4.6 shows the average length of the NWs for a given pitch and hole diameter. The results indicate that NW length is not strongly influenced by hole diameter or pitch.

It might be expected that a low yield would result in longer lengths and larger diameters due to reduced shadowing between NWs (acting as an effectively larger pitch). Figure 4.7 shows the average NW length compared to the yield of a given sample. Instead, the length of the NWs appears to increase slightly as the yield increases for the majority of the samples. This trend suggests that the presence of crystallites on the surface of the substrate can also compete for the increased scattered flux that arises from a low yield.

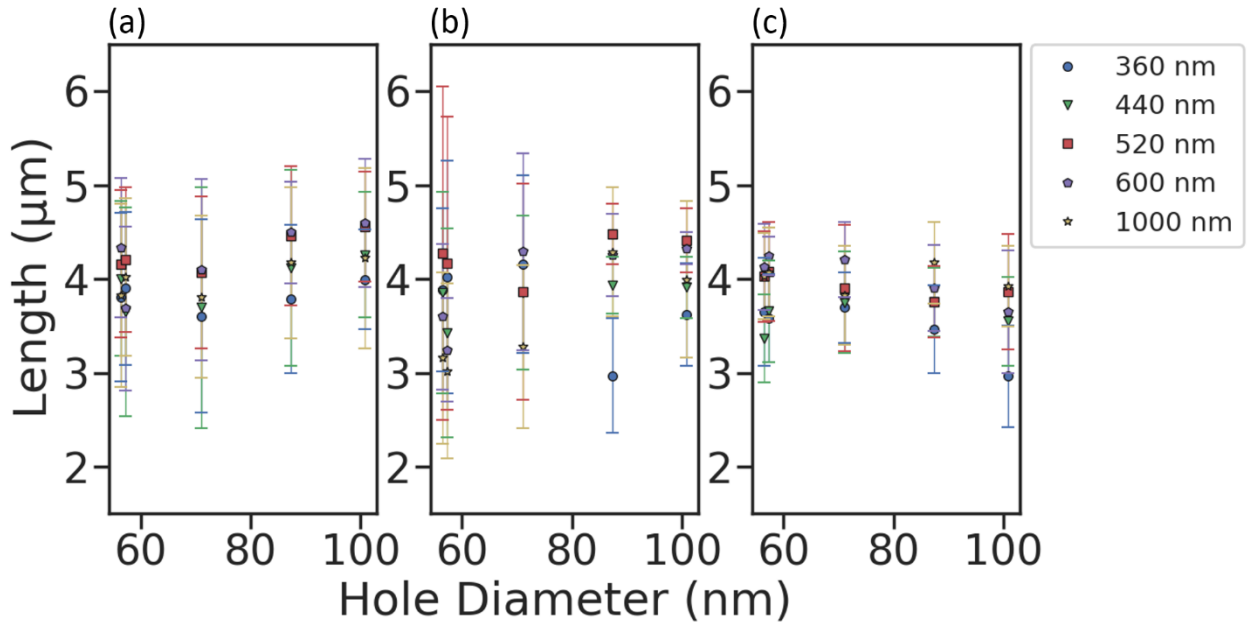


Figure 4.6. NW lengths with (a) 0 s, (b) 250 s and (c) 500 s of Ga pre-deposition. The legend indicates the different pitches.

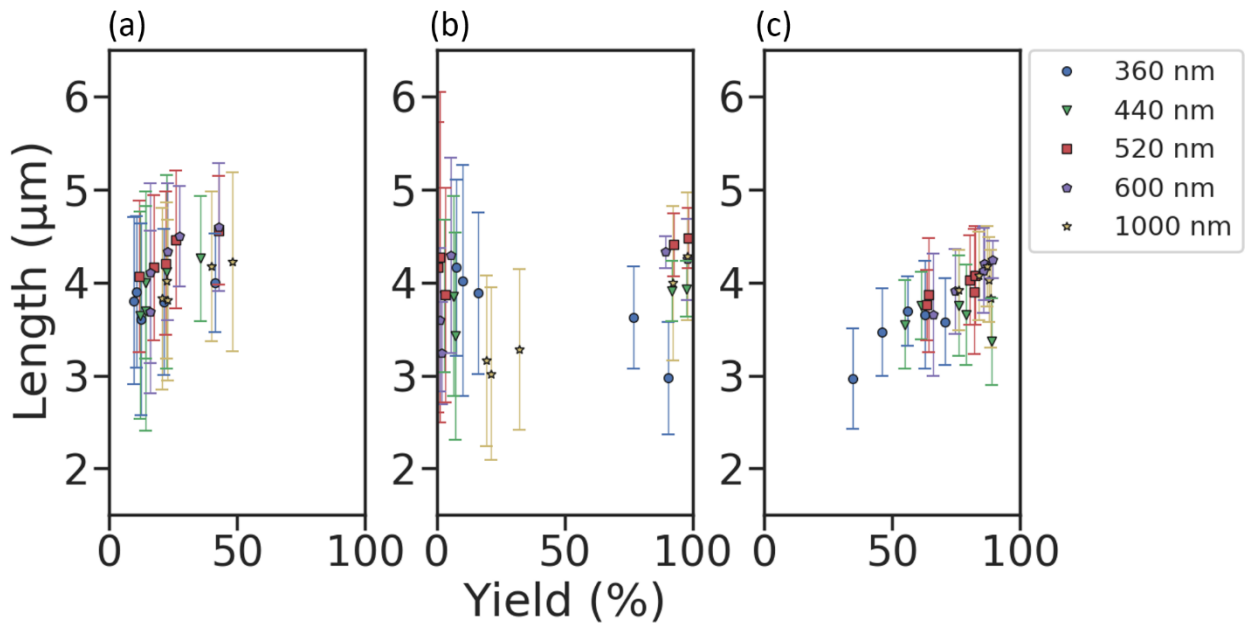


Figure 4.7. NW lengths with (a) 0 s, (b) 250 s and (c) 500 s of Ga pre-deposition compared to the yield for each sample. The legend indicates the different pitches.

4.7. References

- [4.1] N. I. Goktas, P. Wilson, A. Ghukasyan, D. Wagner, S. McNamee, and R. LaPierre, “Nanowires for energy: A review,” *Appl. Phys. Rev.*, vol. 5, no. 4, 2018, Art. no. 041305.
- [4.2] C. J. Goosney, V. M. Jarvis, D. P. Wilson, N. I. Goktas, and R. R. LaPierre, “InSb nanowires for multispectral infrared detection,” *Semicond. Sci. Technol.*, vol. 34, no. 3, 2019, Art. no. 035023.
- [4.3] R. R. LaPierre, M. Robson, K. M. Azizur-Rahman, and P. Kuyanov, “A review of III-V nanowire infrared photodetectors and sensors,” *J. Phys. D. Appl. Phys.*, vol. 50, no. 12, 2017, Art. no. 123001.
- [4.4] R. R. LaPierre et al., “III-V nanowire photovoltaics: Review of design for high efficiency,” *Phys. Status Solidi - Rapid Res. Lett.*, vol. 7, no. 10, pp. 815–830, 2013.
- [4.5] Y. Zhang, J. Wu, M. Aagesen, and H. Liu, “III–V nanowires and nanowire optoelectronic devices,” *J. Phys. D. Appl. Phys.*, vol. 48, no. 46, 2015, Art. no. 463001.
- [4.6] S. J. Gibson, J. P. Boulanger, and R. R. LaPierre, “Opportunities and pitfalls in patterned self-catalyzed GaAs nanowire growth on silicon,” *Semicond. Sci. Technol.*, vol. 28, no. 10, 2013, Art. no. 105025.
- [4.7] P. Kuyanov, J. Boulanger, and R. R. LaPierre, “Control of GaP nanowire morphology by group V flux in gas source molecular beam epitaxy,” *J. Cryst. Growth*, vol. 462, pp. 29–34, 2017.

- [4.8] T. Rieger, S. Heiderich, S. Lenk, M. I. Lepsa, and D. Grützmacher, “Ga-assisted MBE growth of GaAs nanowires using thin HSQ layer,” *J. Cryst. Growth*, vol. 353, no. 1, pp. 39–46, 2012.
- [4.9] C. Colombo, D. Spirkoska, M. Frimmer, G. Abstreiter, and A. Fontcuberta i Morral, “Ga-assisted catalyst-free growth mechanism of GaAs nanowires by molecular beam epitaxy,” *Phys. Rev. B - Condens. Matter Mater. Phys.*, vol. 77, 2008, Art. no. 155326.
- [4.10] M. H. T. Dastjerdi, J. P. Boulanger, P. Kuyanov, M. Aagesen, and R. R. LaPierre, “Methods of Ga droplet consumption for improved GaAs nanowire solar cell efficiency,” *Nanotechnology*, vol. 27, no. 47, 2016, Art. no. 475403.
- [4.11] S. Plissard et al., “Gold-free growth of GaAs nanowires on silicon: Arrays and polytypism,” *Nanotechnology*, vol. 21, no. 38, 2010, Art. no. 385602.
- [4.12] H. Küpers et al., “Diameter evolution of selective area grown Ga-assisted GaAs nanowires,” *Nano Res.*, vol. 11, no. 5, pp. 2885-2893, 2018.
- [4.13] S. J. Gibson and R. R. LaPierre, “Model of patterned self-assisted nanowire growth,” *Nanotechnology*, vol. 25, no. 41, 2014, Art. no. 415304.
- [4.14] J. P. Boulanger et al., “Characterization of a Ga-Assisted GaAs Nanowire Array Solar Cell on Si Substrate,” *IEEE J. Photovoltaics*, vol. 6, no. 3, pp. 661–667, 2016.
- [4.15] F. Jabeen, V. Grillo, S. Rubini, and F. Martelli, “Self-catalyzed growth of GaAs nanowires on cleaved Si by molecular beam epitaxy,” *Nanotechnology*, vol. 19, no. 27, 2008, Art. no. 275711.

- [4.16] S. Plissard, G. Larrieu, X. Wallart, and P. Caroff, “High yield of self-catalyzed GaAs nanowire arrays grown on silicon via gallium droplet positioning,” *Nanotechnology*, vol. 22, no. 27, 2011, Art. no. 275602.
- [4.17] A. M. Munshi et al., “Position-controlled uniform GaAs nanowires on silicon using nanoimprint lithography,” *Nano Lett.*, vol. 14, no. 2, pp. 960–966, 2014.
- [4.18] M. Heiss et al., “III–V nanowire arrays: growth and light interaction,” *Nanotechnology*, vol. 25, no. 1, 2014, Art. no. 014015.
- [4.19] Y. Zhang et al., “Self-catalyzed ternary core–shell GaAsP nanowire arrays grown on patterned Si substrates by molecular beam epitaxy,” *Nano Lett.*, vol. 14, pp. 4542–4547, 2014.
- [4.20] A. Fontcuberta I Morral, C. Colombo, G. Abstreiter, J. Arbiol, and J. R. Morante, “Nucleation mechanism of gallium-assisted molecular beam epitaxy growth of gallium arsenide nanowires,” *Appl. Phys. Lett.*, vol. 92, no. 6, 2008, Art. no. 063112.
- [4.21] F. Matteini, G. Tütüncüoğlu, H. Potts, F. Jabeen, and A. Fontcuberta I Morral, “Wetting of Ga on SiO_x and its impact on GaAs nanowire growth,” *Cryst. Growth Des.*, vol. 15, no. 7, pp. 3105–3109, 2015.
- [4.22] V. G. Dubrovskii, “Stabilization of the morphology and crystal phase in ensembles of self-catalyzed GaAs nanowires,” *Phys. status solidi – Rapid Res. Lett.*, vol. 13, no. 10, 2019, Art. no. 1900301.

- [4.23] F. Matteini et al., “Impact of the Ga Droplet Wetting, Morphology, and Pinholes on the Orientation of GaAs Nanowires,” *Cryst. Growth Des.*, vol. 16, no. 10, pp. 5781–5786, 2016.
- [4.24] M. T. Robson, V. G. Dubrovskii, and R. R. LaPierre, “Conditions for high yield of selective-area epitaxy InAs nanowires on SiOx/Si(111) substrates,” *Nanotechnology*, vol. 26, no. 46, 2015, Art. no. 465301.
- [4.25] J. Vukajlovic-Plestina et al., “Engineering the size distributions of ordered GaAs nanowires on silicon,” *Nano Lett.*, vol. 17, no. 7, pp. 4101–4108, 2017.
- [4.26] J. Vukajlovic-Plestina et al., “Fundamental aspects to localize self-catalyzed III-V nanowires on silicon,” *Nat. Commun.*, vol. 10, no. 1, 2019, Art. no. 869.
- [4.27] V. G. Dubrovskii and M. V. Nazarenko, “Nucleation theory beyond the deterministic limit. I. The nucleation stage,” *J. Chem. Phys.*, vol. 132, no. 11, 2010, Art. no. 114507.

5. Modeling the Nanowire Diameter Progression During Growth

5.1. Summary

This chapter presents previously published work titled “Modeling the dynamics of interface morphology and crystal phase change in self-catalyzed GaAs nanowires” (D. P. Wilson, A. S. Sokolovskii, R. R. LaPierre, F. Panciera, F. Glas, and V. G. Dubrovskii, *Nanotechnology*, vol. 31, no. 48, 2020, Art. no. 485602, DOI: 10.1088/1361-6528/abb106). This work was completed during an internship at ITMO University in Saint Petersburg, Russia. It presents a model for the change in nanowire (NW) radius and contact angle and the relationship between the two as a function of increasing NW length. It presents a system of two coupled equations for the radius and contact angle as a function of length. Additional parameters include the diffusion length of Ga adatoms, the direct flux of Ga and As provided from the molecular beam, and the “reverse” flux. The behavior also depends on two critical contact angles which determine the formation of widening and narrowing facets, which result in changes to the NW radius. A third contact angle determines the switching between ZB and WZ crystal phases and while it is not necessary to solve for the radius and contact angle progressions, it is a useful parameter for designing controlled switching between the two phases during growth.

The mathematical model was derived in collaboration with Vladimir Dubrovskii and Andreii Sokolovskii of Saint Petersburg State University and ITMO University, respectively. In-situ TEM data, where NWs are grown in a TEM equipped with MBE sources, was provided by Frank Glas and Frederico Panciera of the CNRS.

A Python script was written to perform several functions. The script could solve the coupled equations or it could be used to solve for parameters using a data fitting program. The equations were solved using a Runge-Kutta method. The fitting program used least squares to estimate the error between the model and the experimental data and a differential evolution algorithm to find the parameters. The differential evolution algorithm was chosen because it can search a global parameter space and is not gradient dependent. This choice was made since the complexity of the data and the relationship between the parameters often led to multiple local minima.

5.2. Introduction

Semiconductor nanowires (NWs), particularly III–V NWs, are widely considered as fundamental building blocks for nanoscience and nanotechnology [5.1–5.3]. Most III–V NWs are synthesized by the vapor-liquid-solid (VLS) method [5.4] using liquid metal droplets to promote vertical growth. In the case of molecular beam epitaxy (MBE), self-catalyzed VLS growth with gallium droplets [5.5, 5.6] is commonly employed, which allows one to safely avoid gold contamination, reduce the density of crystallographic defects, obtain organized arrays of III–V NWs on silicon substrates, modulate at will the NW radius [5.7–5.12], and narrow the NW length distributions to sub-Poisson values [5.13–5.15]. *In situ* growth monitoring of the NW growth dynamics inside a transmission electron microscope (TEM) [5.16–5.19] plays an important role in understanding the VLS process and controlling the crystal phase of III–V NWs, which can be either cubic zincblende (ZB) or hexagonal wurtzite (WZ) depending on the growth conditions [5.20].

Recent *in situ* TEM data on MBE growth of self-catalyzed GaAs NWs [5.19] clearly reveal the droplet contact angle as the main parameter governing the crystal phase selection. It has been demonstrated that the ZB phase forms at small ($<100^\circ$) and large ($>125^\circ$) contact angles, whereas pure WZ phase is observed for intermediate contact angles. WZ NWs are restricted by vertical sidewalls, whereas ZB NWs taper at small contact angles ($<100^\circ$) or develop a truncated edge at their top at large contact angles ($>125^\circ$). Above a certain maximum contact angle, which was estimated at around 130° in [5.11], ZB NWs start to develop inverse tapering. These trends have been explained by a stationary model based entirely on the surface energetics [5.19, 5.21], and related to the bi-stability of the contact angle under stationary conditions [5.11]. The droplet contact angle can be finely tuned by changing the group III and V fluxes [5.11, 5.17, 5.19], which gives a simple tool for crystal phase switching and obtaining ZB-WZ heterostructures in GaAs NWs. However, a more detailed theoretical description of the interface dynamics under varying material fluxes is missing. Consequently, here we present a model which describes the time-dependent contact angle for vertical NWs, or the top NW radius (at smaller or larger contact angles) for tapered or inverse-tapered NWs. The model fits quite well the data on the evolution of the contact angle in self-catalyzed GaAs NWs [5.19] and should be useful for the fine tuning of the NW interface morphology and the related crystal phase in a wide range of VLS III–V NWs.

5.3. Model

In self-catalyzed growth of III-V NWs, the number of group III atoms in the droplet N_3 is given by the ratio of its volume (with neglect of group V atoms due to their extremely low concentration) over the elementary volume per atom in liquid Ω_L

$$N_3 = \frac{\pi R^3 f(\beta)}{3\Omega_L}. \quad (5.1)$$

Here, R is the top radius of the cylindrical NW, which equals the radius of the droplet base, and

$$f(\beta) = \frac{(1 - \cos \beta)(2 + \cos \beta)}{(1 + \cos \beta) \sin \beta} \quad (5.2)$$

is the geometrical function relating the volume of spherical cap to the cube of its base through the droplet contact angle β , with $df/d\beta = 3/(1 + \cos \beta)^2$.

According to Ref. [5.22], the change in N_3 is described by the material transport equation

$$\frac{dN_3}{dt} = \frac{\pi R^2}{\Omega_S} \left[\frac{2\lambda_3 v_3 \sin \alpha_3 (1 - \theta_{lf}) [\cosh(L/\lambda_3) - 1] + \theta_{sf} - \theta_{lf}}{\pi R \sinh(L/\lambda_3)} - (\chi_5 v_5 - \chi_3 v_3) \right] \quad (5.3)$$

Here, Ω_S is the elementary volume per III-V pair in solid, $\theta_{sf} = n_s/n_f$ and $\theta_{lf} = n_l/n_f$ are the ratios of the group III adatom concentration (n) on the substrate surface (s) to the side facets of the NW (f), and at the liquid-solid interface (l) to the side facets, respectively. They can be related to the corresponding chemical potential differences as discussed in [5.23] and [5.24]. L denotes the NW length, and λ_3 is the collection length of group III adatoms on the NW side facets. The term proportional to $(1 - \theta_{lf})$ in the $1/R$ diffusion flux in equation (5.3) stands for group III atoms collected by the NW sidewalls.

The term proportional to $\theta_{sf} - \theta_{lf}$ describes the diffusion flux from the substrate surface. The diffusion flux is positive when $\theta_{lf} < 1$ and $\theta_{sf} > \theta_{lf}$, meaning that more group III adatoms enter the droplet from the NW sidewalls than escape from the droplet. Negative diffusion fluxes correspond to reverse diffusion of group III atoms from the droplet onto the NW sidewalls [5.23]. Very importantly, the last bracket term in equation (5.3) is proportional to the group V to III influx imbalance, $\chi_5 v_5 - \chi_3 v_3$, with v_k for $k = 3, 5$ as the atomic fluxes of group III and V elements onto the surface (measured in nm/s). The droplet volume will self-equilibrate to a certain stationary value when $\chi_5 v_5 > \chi_3 v_3$ [5.8, 5.9, 5.12], while in the opposite case it will only grow [5.7, 5.11]. The geometrical functions $\chi_k(\alpha_k, \beta)$ in directional MBE growth depend on the beam angles α_k of group III and V species with respect to the substrate normal and the contact angle β according to [5.25].

In many cases [5.8, 5.26, 5.27], the axial growth rate of self-catalyzed III–V NWs is proportional to the incoming flux of group V atoms

$$\frac{dL}{dt} = \chi_5(\alpha_5, \beta)v_5. \quad (5.4)$$

To model experimental data, we assume that $L/\lambda_3 \gg 1$, in which case equation (5.3) contains only the diffusion flux of group III adatoms from the NW sidewalls. Expressing dN_3/dt through dR/dt and $d\beta/dt$ from equations (5.1) and (5.2) and eliminating time by combining equations (5.3) and (5.4), after some simple manipulations we obtain the dynamics of the NW top radius and contact angle versus the NW length L in the form

$$f(\beta) \frac{dR}{dL} + \frac{R}{(1+\cos \beta)^2} \frac{d\beta}{dL} = a + \frac{\rho}{R}. \quad (5.5)$$

Here, the coefficients are given by

$$a = \frac{\Omega_L}{\Omega_S} \left(\frac{\chi_3 v_3}{\chi_5 v_5} - 1 \right), \rho = \frac{\Omega_L}{\Omega_S} \frac{2\lambda_3 \sin \alpha_3 (v_3 - v_l)}{\pi \chi_5 v_5}. \quad (5.6)$$

Clearly, the coefficient a describes the contribution from the direct impingement of group III atoms minus their sink due to NW growth, while ρ gives the diffusion flux of group III adatoms. v_l is the reverse diffusion flux from the droplet onto the NW sidewalls such that $v_l/v_3 = n_l/n_f$. The total diffusion flux is positive when $v_3 > v_l$ and negative otherwise. In our MBE system (*in situ* TEM), Ga flux is perpendicular to the NW axis and As flux parallel to it, therefore

$$\alpha_3 = \pi/2, \chi_3 = \frac{2\beta - \sin(2\beta)}{2\sin^2\beta}, \chi_5 = \frac{1}{\sin^2\beta}. \quad (5.7)$$

According to equation (5.5), the volume of the catalyst droplet may change by changing either the NW top radius R or the droplet contact angle β . The recent data on the morphology of self-catalyzed GaAs NWs [5.11, 5.19, 5.21] can be summarized as follows. Under the stationary conditions corresponding to a fixed V/III ratio, GaAs NWs show two stable contact angles, β_{min} around 90-100° and β_{max} around 130-140°, corresponding to shrinking or extending their top radius R in the ZB phase. Below β_{min} , the NW is ZB and has narrowing (n) facets of angle φ_n while above β_{max} the NW is ZB and has widening (w) facets of angle φ_w (case 1). Between these angles the NW has vertical sidewalls (case 2) and is mainly WZ except above a critical contact angle β_{crit} around 125° [5.19]. These contact angles are semi-stable, meaning that if the change in flux is not ‘too fast’ the contact angle may remain constant at either of these angles (case 3). We define as ‘too fast’ a flux

change which produces a change in radius $dR/dL > |\tan \varphi_k|$. These cases are described by

Case 1:

$$R = R_0 - \tan \varphi_k (L - L_0), \quad (5.8)$$

$$\frac{d\beta}{dL} = \frac{(1+\cos\beta)^2}{R} \left[\left(a + \frac{\rho}{R} \right) + f(\beta) \tan \varphi_k \right], \quad (5.9)$$

with L_0 and R_0 the initial length and radius of the widening or narrowing NW segment.

Case 2:

$$\frac{d\beta}{dL} = \left(a + \frac{\rho}{R} \right) \frac{(1-\cos\beta)^2}{R_0} \quad (5.10)$$

at a constant radius ($dR/dL = 0$), which is the limiting case of Eq. (5.9) for vertical NW sidewalls ($\varphi_k = 0$).

Case 3:

$$\frac{dR}{dL} = \frac{(a+\rho/R)}{f(\beta)} \quad (5.11)$$

at a constant $\beta = \beta_{min}$ or $\beta = \beta_{max}$, as in Refs. [7,8].

If we ignore the β dependence in the geometrical coefficients χ_k , we obtain by integration

Case 1:

$$f(\beta) = \frac{1}{(1-cx)^3} \left\{ f(\beta_0) - \frac{a}{cR_0} [(1-cx)^3 - 1] - \frac{3\rho}{2cR_0^2} [(1-cx)^2 - 1] \right\}. \quad (5.12)$$

Case 2:

$$f(\beta) = f(\beta_0) + 3 \left(\frac{a}{R_0} + \frac{\rho}{R_0^2} \right) x, \quad (5.13)$$

where for brevity we have let $x = L - L_0$ and $c = \tan \varphi_k / R_0$. Integrating Eq. (5.11), in

Case 3 we find:

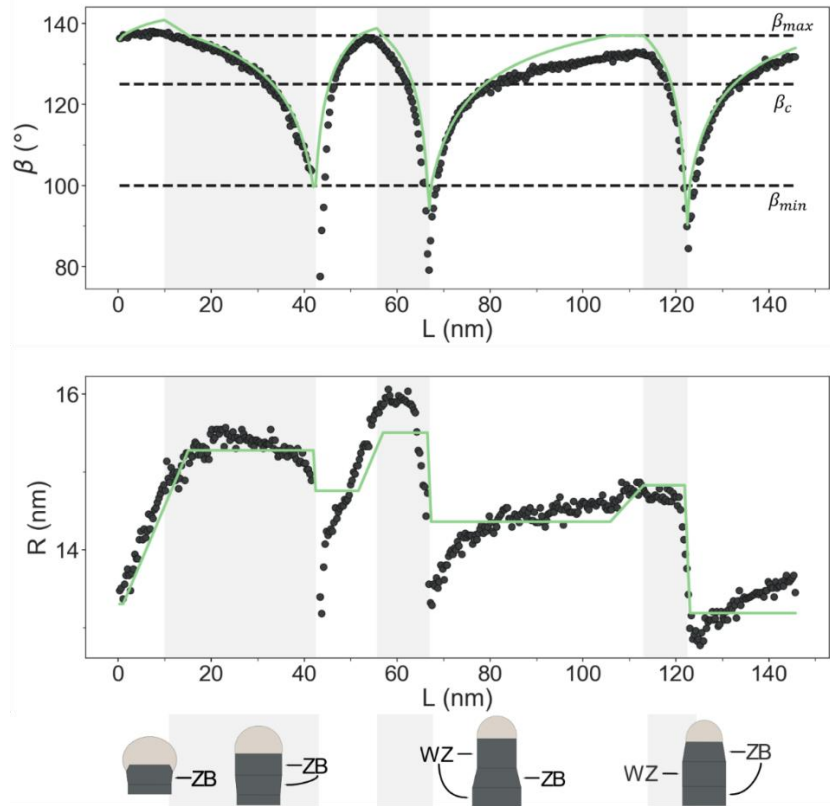


Figure 5.1. Experimental data (symbols) and best fit (lines) of the contact angle (upper panel) and radius (lower panel) dynamics in a single self-catalyzed GaAs NW. The fit is obtained using the parameters given in Table 5.1 to find the solution. The alternating blocks of white and shaded background indicate changes in the V/III ratio as shown in table 5.1. The values of β_{max} and β_{min} are 137° and 100° , respectively, as indicated by dashed lines. The values of φ_w and φ_n are -8° and 55° , respectively, as measured from the images of Ref. [5.19]. The diagrams in the bottom panel show the NW shape and crystal phase. Transitions from the WZ to the ZB phase occur when the contact angle becomes larger than $\beta_c = 125^\circ$, with vertical NW sidewalls and truncated top above this value, or smaller than $\beta_{min} = 100^\circ$, with tapered NW morphology and flat top below this value [5.19].

$$x = \frac{f(\beta)}{a} \left[R - R_0 - \frac{\rho}{a} \ln \left(\frac{R+\rho/a}{R_0+\rho/a} \right) \right], \quad (5.14)$$

which agrees with the result of Refs. [5.7, 5.8].

5.4. Results and Discussion

The data for the contact angle and the NW radius dynamics under varying group III and V fluxes, obtained by *in situ* monitoring of MBE growth of self-catalyzed GaAs NWs grown inside the TEM NanoMax at 420 °C [5.19], are shown in figure 5.1. The growth temperature was fixed at 420 °C. However, the temperature effect on the NW interface morphology and crystal phase was shown to be negligible [5.19]. The main growth parameters affecting the droplet shape were the Ga and As fluxes which were changed abruptly as described in detail in [5.19]. Figure 5.2 shows the representative TEM images of the NW tips with a large and a small Ga droplet. The growth conditions corresponded to those of segment B in figure 5.1. To fit the data, we solve all equations numerically using Python 3.7. The solutions to the ordinary differential equations (equations (5.8)–(5.10)) are found using a Runge–Kutta method [5.28], whereas the approximate forms of the equations (equations (5.12)–(5.14)) are solved by finding the zeros of the equation using the secant method [5.29]. At the end of each solver step, the conditions for the case being solved are checked. If the solution no longer meets the criteria, the solver is switched to the appropriate case and uses the previous solution as the new starting conditions. The best fit is found for the parameters λ_3 , v_5 , v_l and β_{max} by minimizing the sum of squared residuals.

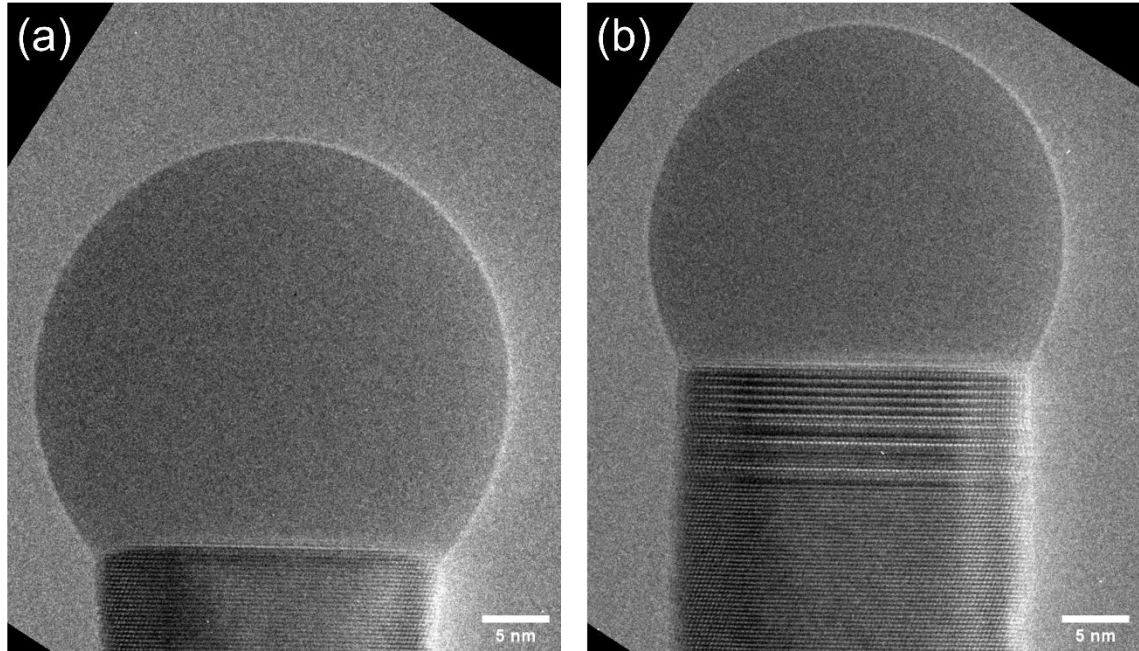


Figure 5.2. TEM images of a GaAs NW with Ga droplet on top corresponding to section B where the droplet contact angle gradually decreases under high As/Ga flux ratio. (a) Large droplet with $\beta > 125^\circ$, yielding a truncated growth interface and pure ZB phase. (b) Small droplet with β approaching 100° , yielding planar growth interface with vertical sidewalls. The crystal phase is pure WZ far below the droplet, with stacking faults appearing immediately below the droplet near the transition from WZ to ZB phase.

Table 5.1. Values of the parameters used to produce the fits to the data.

	Inputs	Parameters		
Segment	v_3 (nm/s)	λ_3 (nm)	v_5 (nm/s)	v_l (nm/s)
A, C	0.15	461	0.1000	0.06167
B	0.15		0.2318	0.2183
D, F	0		0.8989	0.7847
E, G	0.15		0.4736	0.02472

We use a global differential evolution solver to narrow down the parameter space [5.30] and then refine the solution locally with a Nelder–Mead minimization algorithm [5.29].

The data set of [5.19] results from several changes to the Ga and As fluxes. To set our numerical results in the context of the experiment we use the values of the Ga flux, v_3 , stated in [5.19] (0.15 nm s^{-1} or 0 nm s^{-1}). The effective As flux, v_5 , can differ from the direct flux due to reflections within the MBE [5.26] so these values are solved for rather than taken from [5.19]. However, we assume that sections with the same direct flux ratio in the experiment should produce the same values of v_5 and v_l and constrain our fitting algorithm to ensure this is the case. Changes in flux are assumed to be instantaneous. The best fits shown in figure 5.1 are obtained with the parameters summarized in table 1 for each NW section from A to G corresponding to different As and Ga fluxes.

Figure 5.3 shows a comparison of the solutions to equations (5.8)–(5.11) with the approximations at constant χ_3 and χ_5 values given by equations (5.12) and (5.13) for the same parameters given in table 5.1. We can see that the fits obtained for the contact angle dynamics are only slightly worse than those obtained from the general equations. However, the constant χ model cannot reproduce the dynamics of NW radius. Figure 5.4 shows the inverted v_3/v_5 and $(v_3 - v_l)/v_5$ ratios corresponding to the fitting parameters given in table 1 versus the V/III flux ratios as presented in [5.19]. The inverted v_3/v_5 ratios obtained from the fits are not identical to the V/III ratios of [5.19] but remain in the range on the order of unity. For NW segments B, D and F corresponding to the droplet shrinkage, the values $v_3 - v_l$ are negative (even if v_3 is non-zero as in segment B) and so are the $(v_3 - v_l)/v_5$ ratios.

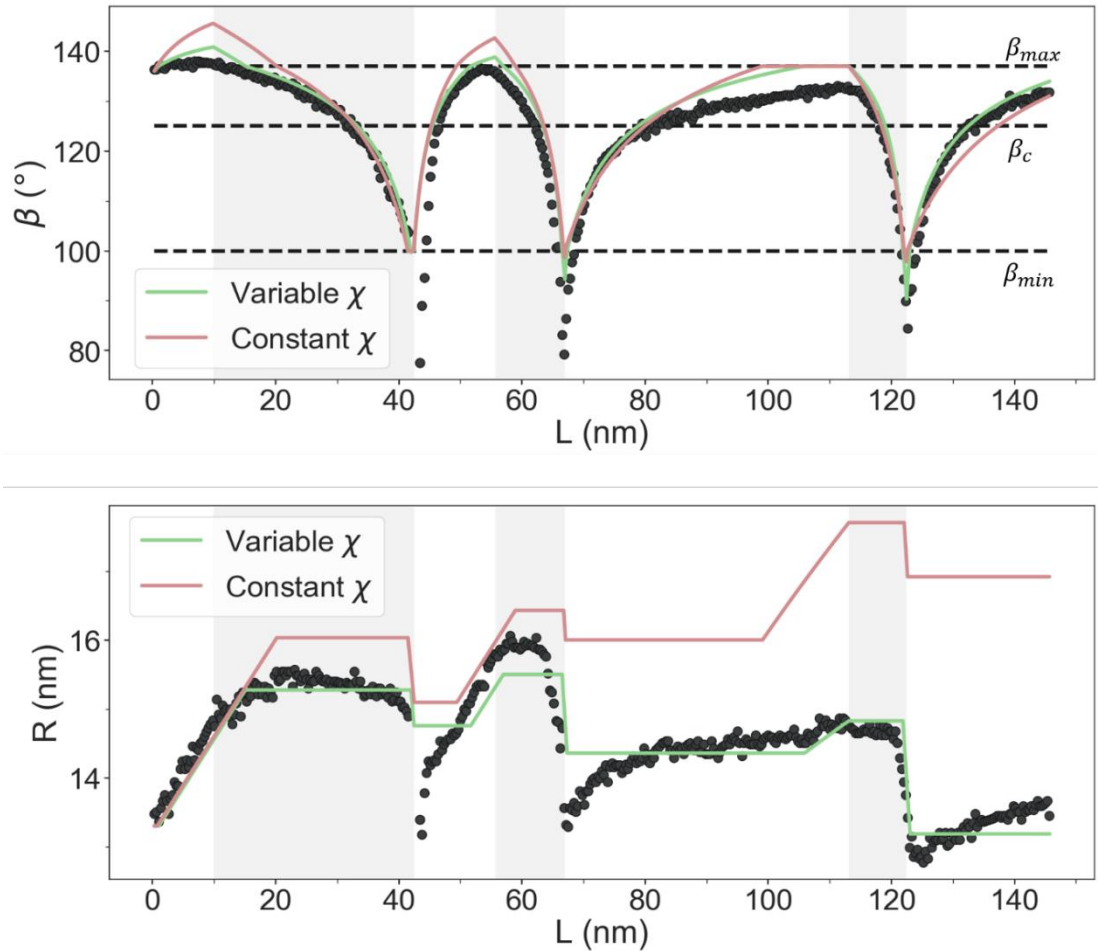


Figure 5.3. The solutions from solving the equations with χ dependent on β as compared to using constant χ values. The solution shown for variable χ is the same as that in Fig. 5.1. Both solutions use the parameters given in Table 3. The constant value of χ_3 and χ_5 were set to 0.808 and 1.132, respectively, corresponding to $\beta = 110^\circ$. We choose 110° because it falls in the middle of the range of contact angles present in this study. While the plots are similar for β , small differences compound as L increases which results in the plots of R diverging from one another.

Let us now analyze these results and the parameter values used to obtain best fits to the data. The taper angles for widening and narrowing side facets were obtained from the TEM images of [5.19]. The contact angle changes under varying material fluxes are well-fitted with a fixed collection length of gallium adatoms of 461 nm regardless of the V/III flux ratio. This relatively small value (compared, for example, to 750 nm in [5.8]) should be due to the low growth temperature of 420 °C, because the surface diffusion is thermally activated [5.3]. At a fixed λ_3 , the main parameter influencing the fits is the reverse diffusion flux of Ga from the droplet onto the NW sidewalls, v_l . It is well known that the ratio $v_l/v_3 = n_l/n_f$, which directs the Ga diffusion flux to the droplet at $v_l/v_3 < 1$ or from the droplet at $v_l/v_3 > 1$, changes very substantially when altering the V/III flux ratio [5.24]. Here, we find that v_l/v_3 is noticeably lower than unity (on the order of 0.2–0.4) in segments A, C, E and G corresponding to the droplet inflation steps and ultimately to large droplets with the contact angles within the range of 125-140° and pure ZB phase of GaAs NWs. This yields high Ga diffusion fluxes from the NW sidewalls to the droplet which are several times larger than the direct vapor flux of Ga. Conversely, in segments B, D and F, the Ga diffusion flux is directed from the droplet down to the substrate. This reverse diffusion is the main mechanism of the droplet shrinkage to a contact angle of 100° or even less, and the crystal phase of GaAs NWs becomes ZB again. As a general conclusion, the possibility to rapidly redirect the diffusion flux of Ga to or from the droplet by changing the V/III flux ratio allows for a sharp change of the droplet contact angle which determines the crystal phase and consequently thinner ZB/WZ heterostructures.

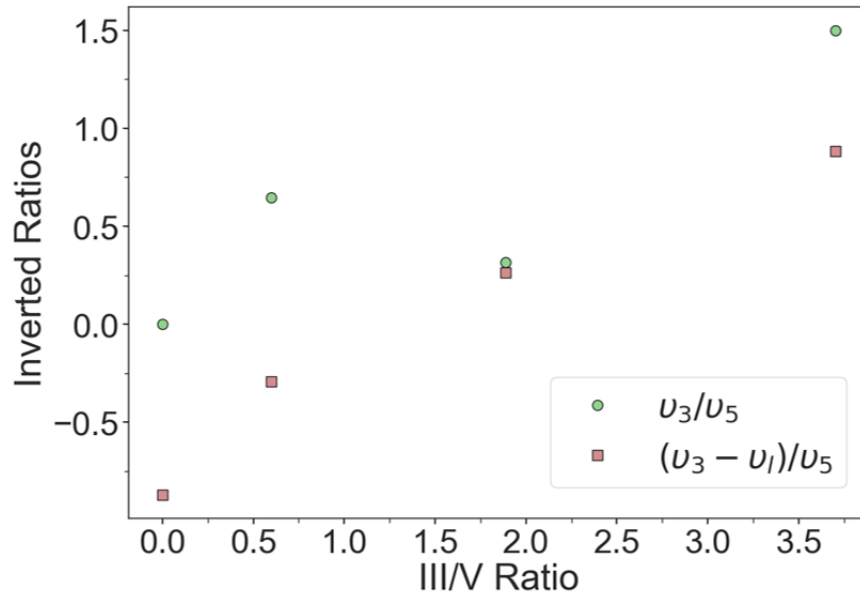


Figure 5.4. The relationship between the inverted V/III ratios numerically determined for the solved parameters and the V/III flux ratios as presented in Ref. [19]. Both the V/III ratios and the V/III ratios with reverse diffusion are shown.

We note that the changes of the contact angle shown in figure 5.1 are highly non-linear, particularly for small β below β_{min} . The amplitude of the radius oscillations obtained from *in situ* data (symbols in figures 5.1 and 5.3) is very small (< 3 nm). However, the variations of the measured radius are non-linear, while theoretical curves are linear due to this very small amplitude of oscillations. We found it impossible to exactly fit *in situ* data for the contact angle *and* the NW radius dynamics simultaneously using the current model. Figures 5.1 and 5.3 show that, when we solve for the best fit of the contact angle and radius simultaneously, there is a discrepancy in the measured and modelled radius

changes. This may be partly due to the radial growth, which is not included in the model but affects the radius of WZ NW sections during the increase of the contact angle. We use cylindrical NW geometry and spherical cap droplet geometry, while in the real NWs the liquid droplet is constrained to rest on top of a hexagonal shape. Finally, the small and large contact angles were estimated in [5.11, 5.19, 5.21] from surface energy considerations and under stationary material fluxes, while the data of [5.19] were obtained with abrupt changes of the fluxes. Despite these complicated factors, the current model fits very accurately the contact angle crossing the two critical angles ($\beta_{min} = 100^\circ$ and $\beta_c = 125^\circ$) for the crystal phase changes.

In conclusion, our model describes fast changes of the droplet contact angle under variable fluxes of group III and V elements. We considered self-catalyzed VLS growth of III–V NWs by MBE. However, generalization of this approach to Au-catalyzed VLS growth of III–V NWs requires only a slight modification. The crystal phase change is determined by the dynamics of the droplet contact angle. In the case of GaAs NWs, there is a wide range of the contact angles in which the NWs grow in the WZ phase with vertical sidewalls. As discussed in [5.19], the best point for sharp ZB-WZ phase change is around the critical contact angle of 125° , because it occurs without changing the NW radius and does not require too rapid droplet shrinkage under excessive V/III flux ratio. The situation may be different for GaP NWs, which seem to maintain a stable contact angle around 123° in the ZB phase according to [5.12] and [5.21]. In this case, a ZB-WZ phase transition may require tapering. It will be interesting to consider in more detail the droplet dynamics in doped GaAs and other III–V NWs where the introduction of doping impurities may change

the surface energetics and lead to the formation of regular twinning superlattices [5.31]. We plan to study the interface dynamics of other III–V NWs using a similar approach. We will also refine the model to include the radial growth on the NW sidewalls, which occurs after the crystal phase is decided. Overall, our approach should be applicable to a wide range of III–V materials and epitaxy techniques, and further used for developing the growth protocols to form ZB-WZ NW heterostructures in a controllable manner.

5.5. References

- [5.1] P. Yang, R. Yan, and M. Fardy, “Semiconductor nanowire: What’s next?,” *Nano Lett.*, vol. 10, no. 5, pp. 1529–1536, 2010.
- [5.2] A. Zhang, G. Zheng, and C. M. Lieber, *Nanowires: Building blocks for nanoscience and nanotechnology*. Berlin: Springer, 2016.
- [5.3] V. G. Dubrovskii, “Theory of VLS growth of compound semiconductors,” in *Semiconductors and Semimetals*, vol. 93, A. Fontcuberta i Morral, Ed. New York: Academic, 2015, pp. 1–78.
- [5.4] R. S. Wagner and W. C. Ellis, “Vapor-liquid-solid mechanism of single crystal growth,” *Appl. Phys. Lett.*, vol. 4, no. 5, pp. 89–90, 1964.
- [5.5] C. Colombo, D. Spirkoska, M. Frimmer, G. Abstreiter, and A. Fontcuberta i Morral, “Ga-assisted catalyst-free growth mechanism of GaAs nanowires by molecular beam epitaxy,” *Phys. Rev. B - Condens. Matter Mater. Phys.*, vol. 77, 2008, Art. no. 155326.

- [5.6] F. Jabeen, V. Grillo, S. Rubini, and F. Martelli, “Self-catalyzed growth of GaAs nanowires on cleaved Si by molecular beam epitaxy,” *Nanotechnology*, vol. 19, no. 27, 2008, Art. no. 275711.
- [5.7] G. Priante, S. Ambrosini, V. G. Dubrovskii, A. Franciosi, and S. Rubini, “Stopping and resuming at will the growth of GaAs nanowires,” *Cryst. Growth Des.*, vol. 13, no. 9, pp. 3976–3984, 2013.
- [5.8] V. G. Dubrovskii et al., “Self-Equilibration of the Diameter of Ga-Catalyzed GaAs Nanowires,” *Nano Lett.*, vol. 15, no. 8, pp. 5580–5584, 2015.
- [5.9] J. Tersoff, “Stable self-catalyzed growth of III-V nanowires,” *Nano Lett.*, vol. 15, no. 10, pp. 6609–6613, 2015.
- [5.10] F. Matteini, V. G. Dubrovskii, D. Ruffer, G. Tütüncüoğlu, Y. Fontana, and A. F. I. Morral, “Tailoring the diameter and density of self-catalyzed GaAs nanowires on silicon,” *Nanotechnology*, vol. 26, no. 10, 2015, Art. no. 105603.
- [5.11] W. Kim et al., “Bistability of contact angle and its role in achieving quantum-thin self-assisted GaAs nanowires,” *Nano Lett.*, vol. 18, no. 1, pp. 49–57, 2018.
- [5.12] E. D. Leshchenko, P. Kuyanov, R. R. LaPierre, and V. G. Dubrovskii, “Tuning the morphology of self-assisted GaP nanowires,” *Nanotechnology*, vol. 29, no. 22, 2018, Art. no. 225603.
- [5.13] F. Glas and V. G. Dubrovskii, “Self-narrowing of size distributions of nanostructures by nucleation antibunching,” *Phys. Rev. Mater.*, vol. 1, no. 3, 2017, Art. no. 036003.

- [5.14] E. S. Koivusalo, T. V. Hakkarainen, M. D. Guina, and V. G. Dubrovskii, “Sub-poissonian narrowing of length distributions realized in Ga-catalyzed GaAs nanowires,” *Nano Lett.*, vol. 17, no. 9, pp. 5350–5355, 2017.
- [5.15] T. Tauchnitz, Y. Berdnikov, V. G. Dubrovskii, H. Schneider, M. Helm, and E. Dimakis, “A simple route to synchronized nucleation of self-catalyzed GaAs nanowires on silicon for sub-Poissonian length distributions,” *Nanotechnology*, vol. 29, no. 50, 2018, Art. no. 504004.
- [5.16] C.-Y. Wen et al., “Periodically changing morphology of the growth interface in Si, Ge, and GaP nanowires,” *Phys. Rev. Lett.*, vol. 107, no. 2, 2011, Art. no. 025503.
- [5.17] D. Jacobsson et al., “Interface dynamics and crystal phase switching in GaAs nanowires,” *Nature*, vol. 531, no. 7594, pp. 317–322, 2016.
- [5.18] J. C. Harmand et al., “Atomic step flow on a nanofacet,” *Phys. Rev. Lett.*, vol. 121, no. 16, 2018, Art. no. 166101.
- [5.19] F. Panciera et al., “Phase selection in self-catalyzed GaAs nanowires,” *Nano Lett.*, vol. 20, no. 3, pp. 1669–1675, 2020.
- [5.20] F. Glas, J. C. Harmand, and G. Patriarche, “Why does wurtzite form in nanowires of III-V zinc blende semiconductors?,” *Phys. Rev. Lett.*, vol. 99, no. 14, 2007, Art. no. 146101.
- [5.21] V. G. Dubrovskii, N. V. Sibirev, N. N. Halder, and D. Ritter, “Classification of the morphologies and related Crystal phases of III–V nanowires based on the surface energy analysis,” *J. Phys. Chem. C*, vol. 123, no. 30, pp. 18693–18701, 2019.

- [5.22] V. G. Dubrovskii, “Stabilization of the morphology and crystal phase in ensembles of self-catalyzed GaAs nanowires,” *Phys. status solidi – Rapid Res. Lett.*, vol. 13, no. 10, 2019, Art. no. 1900301.
- [5.23] V. G. Dubrovskii et al., “Role of nonlinear effects in nanowire growth and crystal phase,” *Phys. Rev. B - Condens. Matter Mater. Phys.*, vol. 80, no. 20, 2009, Art. no. 205305.
- [5.24] J. C. Harmand, F. Glas, and G. Patriarche, “Growth kinetics of a single $\text{InP}_{1-x}\text{As}_x$ nanowire,” *Phys. Rev. B - Condens. Matter Mater. Phys.*, vol. 81, no. 23, 2010, Art. no. 235436.
- [5.25] F. Glas, “Vapor fluxes on the apical droplet during nanowire growth by molecular beam epitaxy,” *Phys. Status Solidi Basic Res.*, vol. 247, no. 2, pp. 254–258, 2010.
- [5.26] F. Glas, M. R. Ramdani, G. Patriarche, and J. C. Harmand, “Predictive modeling of self-catalyzed III-V nanowire growth,” *Phys. Rev. B - Condens. Matter Mater. Phys.*, vol. 88, no. 19, 2013, Art. no. 195304.
- [5.27] V. G. Dubrovskii, “Group V sensitive vapor-liquid-solid growth of Au-catalyzed and self-catalyzed III-V nanowires,” *J. Cryst. Growth*, vol. 440, pp. 62–68, 2016.
- [5.28] E. Hairer, S. P. Norsett, and G. Wanner, *Solving Ordinary Differential Equations II: Stiff and Differential-Algebraic Problems*, 2nd ed. Springer-Verlag, 1993.
- [5.29] P. Virtanen et al., “SciPy 1.0: fundamental algorithms for scientific computing in Python,” *Nat. Methods*, vol. 17, no. 3, pp. 261–272, 2020.

- [5.30] R. Storn and K. Price, “Differential evolution - A simple and efficient heuristic for global optimization over continuous spaces,” *J. Glob. Optim.*, vol. 11, no. 4, pp. 341–359, 1997.
- [5.31] N. Isik Goktas, A. Sokolovskii, V. G. Dubrovskii, and R. R. LaPierre, “Formation mechanism of twinning superlattices in doped GaAs nanowires,” *Nano Lett.*, vol. 20, no. 5, pp. 3344–3351, 2020.

6. MBE Grown Photovoltaic Light Funnels Using Droplet Dynamics

6.1. Summary

This chapter presents the work from our paper titled “Photovoltaic Light Funnels Grown by Nanowire Droplet Dynamics” (D. P. Wilson, A. S. Sokolovskii, N. I. Goktas, V. G. Dubrovskii, and R. R. LaPierre, IEEE J. Photovoltaics, vol. 9, no. 5, pp. 1225–1231, 2019., DOI: 10.1109/JPHOTOV.2019.2925554.) This work studied the growth of tapered GaAs nanowires (NWs), which were achieved by adjusting the V-III flux ratio during the NW growth. All NWs began with a short segment of GaP, which has been shown to improve yield, before transitioning to GaAs over the course of 5 min. While the P_2 flux is reduced to zero, the As_2 is introduced so that the final V-III ratio is equal to 1. We observe the formation of NWs with thin bases that rapidly inflate to large top segments upon the changing flux ratio. To prevent the sharp change in diameter, the GaP segment is reduced which allows the V/III ratio change to occur closer to the substrate. The yield of the NW arrays remains high.

This work was supported by optical simulations in COMSOL Multiphysics 5.3a using the RF module. The NW unit cell was illuminated with incoming light power weighted to the solar spectrum. An array of tapered NWs with a pitch of 320 nm, a top diameter of 170 nm, and a base diameter of 100 nm was compared to an array of cylindrical NWs with equal pitch but a constant diameter of 170 nm. The absorptance spectra for the tapered NWs showed additional peaks which are not present in the cylindrical NW. The calculated photocurrent of the tapered NW array was only slightly less than that of the

cylindrical NW array (24.7 mA/cm² compared to 25.6 mA/cm².) The similarity of the values indicates that tapered NWs are competitive with cylindrical NWs. These results also suggested that a study would be required, as has been done numerous times with cylindrical NWs, to optimize the diameter and tapering of the conical NWs to achieve maximum photocurrent. The results of this study are presented in Section 7.

The results of the growth study were compared to a numerical model. The derivations and fitting were provided in collaboration with Andrei S. Sokolovskii and Vladimir G. Dubrovskii of ITMO University in St. Petersburg, Russia. The growth model used is similar to the one presented in Section 4 but does not require knowledge of the contact angle and does not consider the type of faceting that occurs during NW growth. The contact angle is assumed constant. The NW diameter is still derived based on the droplet volume, but the equations take a simpler form with the effective fluxes and other terms being collected into the parameters A and B and the radius being determined by a single equation rather than a coupled set. This model is appropriate for use here since the contact angle throughout growth cannot be observed directly in our system.

6.2. Introduction

Semiconductor III-V nanowires (NWs) have shown promise for optoelectronic device applications due to their unique photonic properties. Specifically, the optical absorption spectrum of vertically standing III–V NWs can be tuned by NW diameter due to resonant HE₁₁ radial waveguide modes [6.1]. This property enables either broadband

light absorption for photovoltaics (PV) [6.2, 6.3], or narrow-band multispectral absorption for photodetectors [6.4–6.6].

III–V NWs are typically grown by the vapor–liquid–solid (VLS) method, whereby a metal droplet or seed particle nucleates and sustains growth of the NWs [6.6]. The self-assisted growth method employs a seed particle that is an element of the NW itself (e.g., Ga droplets for growth of GaAs NWs). Furthermore, selective-area epitaxy, using an oxide mask, can be used to control the NW position to produce periodic NW arrays [6.6].

GaAs NWs integrated with Si substrates are particularly interesting as a GaAs/Si tandem solar cell to boost the efficiency of conventional Si PV modules [6.7]. The diameter, length, and period of the NW array needs to be controlled for optimal PV efficiency. Numerical simulations have shown that the optimum absorptance of the solar spectrum in GaAs NW arrays requires a NW length of several microns, an NW diameter of ~ 170 nm, and an NW period of (separation between NWs) of ~ 320 – 360 nm [6.8–6.10]. Such a diameter can be achieved by growing a thin core by the self-assisted VLS method, and then thickening the NW laterally along the radial direction by vapor-solid (VS) deposition on the NW sidewalls after elimination of the droplet [6.11, 6.12]. This method of NW growth is usually used to produce a core-shell (coaxial) p-n junction geometry. However, this approach is not amenable to purely axial NW p-n junctions as used, for example, in tandem NW solar cells [6.7]. In addition, the highest NW PV efficiency reported thus far has been demonstrated in axial NW p-n junctions, rather than core-shell NW p-n junctions [6.13, 6.14]

Growing thick NWs is further complicated if the NW and substrate are lattice mismatched. GaAs NWs grown on lattice-mismatched substrates such as Si exhibit a critical diameter above which NW growth is hindered, or plastic relaxation of the strain occurs by formation of misfit dislocations [6.15]. For GaAs NWs on Si, this critical diameter has been estimated at 110 nm [6.16], which is below the desired diameter for optimum PV efficiency. There are reports of critical diameters as small as 10 nm for GaAs NWs on Si [6.17]. On the other hand, if the misfit dislocations are isolated at the NW-Si interface and do not propagate along the NW length (as in [6.17]), then they may not be detrimental to device performance. Further studies on the nature of dislocations in NWs and their influence on device performance would be beneficial.

Rather than lateral extension of the NWs by VS deposition on the NW sidewalls, the NW diameter can alternatively be controlled by adjusting the droplet size. Attempts to produce large droplets (and, hence, large NW diameter) in the initial stages of growth by a Ga predeposition step typically result in a low NW yield with the formation of crystallites due to overgrowth on the oxide mask [6.18]. Large droplets at the top of NWs can also result in the droplet wetting the NW sidewalls, resulting in the formation of kinked NWs [6.19]. Finally, increasing the hole size in the oxide mask (to collect larger Ga droplets) results in polynucleation, multiple seed formation and multiple NW growth within each oxide hole, rather than a single NW per hole [6.20, 6.21].

Rather than attempting to increase the size of Ga droplets in the initial stages of growth, this paper will show that the droplet can be gradually inflated by adjusting the Ga flux that the droplet receives throughout growth. This can be accomplished by adjusting

the V/III flux ratio during growth [6.22, 6.23]. High V/III flux ratio shrinks the droplet, resulting in positively tapered NWs or the complete consumption of the droplet [6.11, 6.23]. Conversely, for low V/III flux ratio, the droplet volume expands and the morphology of the NW can change from positive-tapered to straight or inverse-tapered [6.23]. As a result, this paper presents a simple method of growing GaAs NWs that are sufficiently thin at their base to avoid dislocations due to lattice misfit with the Si substrate, and thick enough at their top to optimize solar absorption.

6.3. Experimental Details

GaAs NWs were grown in a gas source molecular beam epitaxy (GS-MBE) system by the self-assisted VLS method (i.e., using a Ga droplet). A 30 nm layer of SiO_x was deposited on Si (111) wafers by plasma-enhanced chemical vapour deposition (PE-CVD). The SiO_x was patterned by electron beam lithography (EBL) and reactive ion etching into hexagonal arrays of holes of ~100 nm diameter (below the critical thickness of 110 nm) and pitch of 360, 600, or 1000 nm. Further details on the substrate preparation method are available in [6.12].

All NWs began with a GaP NW stem that has been shown to improve yield; i.e., the fraction of holes filled with a single vertically standing NW [6.12]. The GaP stem is also used as a back surface field in NW-based PV devices [6.12]. After growth of the GaP stem, a “ramp” stage was implemented where the P₂ flux was decreased to zero and the As₂ flux was linearly increased over the course of 5 min to switch from growth of GaP to GaAs. This ramp stage was followed by growth of the GaAs segment for 120 min. The

substrate temperature was 600 °C and Ga impingement rate was 0.125 $\mu\text{m}/\text{h}$ throughout growth.

Three growths were performed. In the first growth (referred to as “sample A”), the GaP stem was grown for 25 min and the V/III flux ratio was kept constant at 2 throughout growth. A second growth (“sample B”) was identical to the previous, but was performed with a change of V/III flux ratio from 2 to 1 during the ramp stage. The group V flux progression with time is illustrated in Fig. 6.3(a) for this case. Finally, a third growth (“sample C”) was performed with a shorter GaP stem of only 10 min, followed by the same change of V/III flux ratio from 2 to 1 during the ramp stage.

The NW morphology was examined using a JEOL JSM-7000F scanning electron microscope (SEM) operated at 5 kV. The resulting NW morphology is described by a growth model, involving the flux of Ga atoms to the droplet. Numerical studies of optical absorption in the resulting inverse-tapered NWs was implemented by the finite element method (FEM) using COMSOL Multiphysics 5.3a [6.24].

6.4. Results

6.4.1. NW Growth

Fig. 6.1(a) shows a representative SEM image of a GaAs NW array grown with a constant V/III flux ratio of 2 (sample A). The NWs of Fig. 6.1(a) had a diameter of 135, 151, and 178 nm at their base, and 73, 96, and 172 nm at their top for a pitch of 360, 520, and 1000 nm, respectively. Hence, the NWs were positive-tapered with a larger diameter at the base compared to the top, as typically observed for self-assisted GaAs NWs [6.25].

The increasing diameter with pitch is caused by Ga re-emission from the oxide mask area surrounding each NW, which increases with the pitch [6.26]. A top NW diameter that is sufficient for strong solar light absorption (~170 nm) is only achieved with the largest pitch of 1000 nm. However, a pitch of 1000 nm is far from the optimum pitch of 360 nm for light absorption. Also, these NWs exhibit a large base diameter that exceeds the critical diameter for dislocations (~110 nm). Hence, the NW growth conditions of sample A result in a positive NW tapering with a large base diameter that can exceed the critical diameter for dislocations, and a small top diameter that is too small for optimum solar absorption.

Next, we examined the influence on the NW morphology of decreasing the V/III flux ratio from 2 to 1 after 25 min of GaP stem growth (sample B). The SEM image of Fig. 6.1(b) shows that the Ga droplet appears to have rapidly expanded, revealing the thin GaP stem at the base of the NWs followed by an abrupt transition to a much wider GaAs segment at the top. In this case, a large Ga droplet is also clearly visible at the top of the NWs. The slight bending of the NWs observed in Fig. 6.1(b) is due to NW attraction caused by electrostatic charging [6.27]. The base of the NWs had a diameter of about 52 nm regardless of pitch, while the top of the NWs had a much wider diameter of 152, 177, and 185 nm for a pitch of 360 nm, 520 nm, and 1000 nm, respectively. As described above, the diameter increased with pitch due to re-emission of Ga from the oxide mask [6.26]. In this case, the NWs exhibited a small base diameter (52 nm), well below the critical diameter for dislocations (110 nm). Concurrently, by lowering the V/III flux ratio after stem growth, the net flux of Ga to the droplet increased, causing an expansion of the droplet and thereby achieving a much larger NW diameter at the top than would otherwise be possible. For the

pitch of 360 nm (optimum for light absorption), a top diameter of 152 nm was achieved, nearly twice that of the NWs in Fig. 6.1(a) and nearer the optimum for solar absorption.

Finally, we examined the growth where the V/III flux ratio was reduced from 2 to 1 after only 10 min of GaP stem growth (sample C). The SEM image in Fig. 6.1(c) indicated a NW morphology with a gradual inverse tapering, rather than the abrupt transition in diameter of Fig. 6.1(b). In this case, the shorter stem was not visible due to the droplet

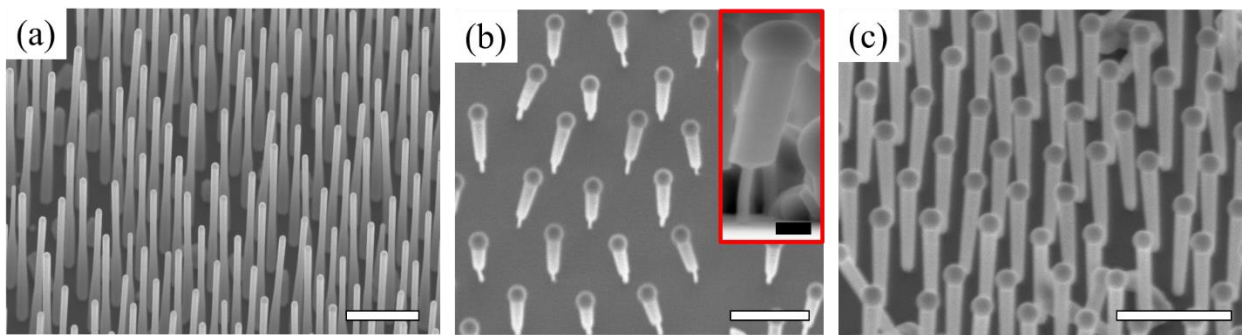


Figure 6.1. (a) 20° tilted SEM image of NW array from sample A with a V/III flux ratio of 2 throughout growth. Pitch is 520 nm. Scale bar is 1 μm . (b) 30° tilted SEM image of NW array from sample B with a V/III flux ratio that was reduced from 2 to 1 after 25 min of GaP stem growth. Pitch is 1000 nm. Scale bar is 1 μm . Inset shows a magnified cross-sectional SEM view with a scale bar of 100 nm. (c) 30° tilted SEM image of NW array from sample C with a V/III flux ratio that was reduced from 2 to 1 after 10 min of GaP stem growth. Pitch is 520 nm. Scale bar is 1 μm .

expansion occurring near the substrate surface. The NWs of Fig. 6.1(c) had a diameter of 98, 111, and 115 nm at their base, and 138, 163, and 166 nm at their top for a pitch of 360, 520, and 1000 nm, respectively. Again, the diameter increased with pitch due to re-emission of Ga from the oxide mask [6.26]. In this case, the base diameter for a pitch of 360 nm was below the critical thickness for dislocations, while the top diameter of 138 nm was nearly twice that of the NWs in Fig. 6.1(a) and nearer the optimum for solar absorption. With continued growth, the NW top diameter will continue to expand and any desired top diameter can be achieved. Hence, a V/III flux ratio of 2 resulted in positive-tapered NWs (Fig. 6.1(a)) that is usually observed for self-assisted NWs, while a V/III flux ratio of 1

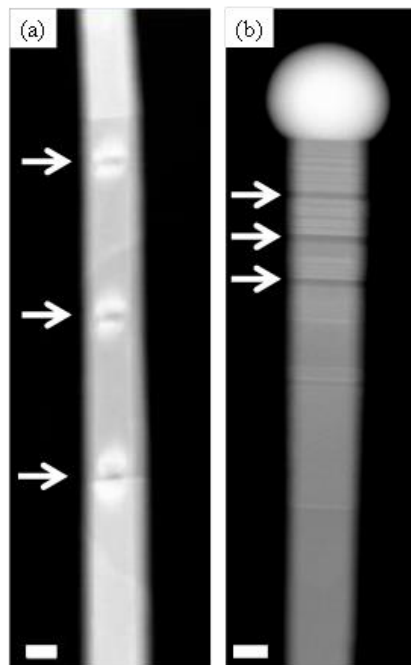


Figure 6.2. STEM image of NW from (a) sample A and (b) sample B, with three marker layers indicated by arrows. Scale bars are 50 nm.

resulted in inverse-tapered or funnel-shaped NWs (Fig. 6.1(b), (c)) that are more desirable for PV.

An additional factor influencing NW morphology is the possible presence of parasitic VS growth on the NW sidewalls. The presence of VS growth was observed by introducing GaAs_{0.8}P_{0.2} marker layers periodically during growth, as described in Ref. [6.12]. The marker layers were observed by a JEOL 2010F scanning transmission electron microscope (STEM) using high angle annular dark field (HAADF) imaging at 200 kV. Fig. 6.2a shows the presence of GaAs radial overgrowth at the base of sample A with a NW diameter of 112 nm and marker layer diameter of 66 nm. This radial growth is believed to contribute to the positive tapering observed in the NWs of sample A, with less overgrowth occurring towards the NW top. The thin stem of the NWs in sample B, which are comparable in diameter to the marker layers in Fig. 6.2a, suggests that these NWs experience less radial growth at their base when the V/III flux ratio was reduced. Fig. 6.2b shows negligible radial growth near the top of sample B. Thus, the NW top diameter was determined by the Ga droplet expansion that occurred upon reduction of the V/III flux ratio. The NW top radius can be expressed in terms of the Ga droplet radius. When the V/III flux ratio is instantaneously reduced, an excessive Ga influx to the droplet leads to a rapidly increasing NW top diameter [6.28, 6.29]. The number of Ga atoms (N_3) in the droplet changes with time according to the following equation [6.30, 6.31]:

$$\frac{dN_3}{dt} = J_3^{eff} \pi R^2 + 2J_3 \sin(\alpha_3) R\lambda \left(1 - \frac{\theta_l}{\theta_s}\right) - \frac{\pi R^2}{\Omega_{35}} \frac{dL}{dt} \quad (6.1)$$

where R is the radius of a cylindrical NW. In the first term, J_3^{eff} is the influx of Ga atoms from vapor, including contributions from direct impingement, re-emission from the oxide mask and re-emission from the sidewalls of neighboring NWs. The second diffusion-induced term in (6.1) is proportional to the direct flux of Ga atoms, J_3 , impinging onto the NW sidewalls with the incident angle α_3 ; λ is the effective diffusion length of the Ga adatoms on the NW sidewalls; and θ_l and θ_s are the activity of Ga in the liquid droplet and on the NW sidewalls, respectively, which accounts for the reverse diffusion flux from the droplet [6.30, 6.31]. The $\frac{\theta_l}{\theta_s} = \exp\left(\frac{\mu_3 - \mu_5}{k_B T}\right)$ where μ_3 and μ_5 is the chemical potential of Ga atoms in liquid and on the NW sidewalls, respectively, k_B is the Boltzmann constant and T is the absolute temperature. Finally, the third term in (6.1) describes the sink of Ga atoms in the liquid due to the NW axial growth rate $\frac{dL}{dt}$, where Ω_{35} is the elementary volume per III-V pair in the solid ($\Omega_{35} = 0.0452 \text{ nm}^3$ for GaAs, and $\Omega_{35} = 0.0405 \text{ nm}^3$ for GaP).

Similarly, the rate of change of the total number of As atoms (N_5) in the droplet is given by:

$$\frac{dN_5}{dt} = J_5^{eff} \pi R^2 - \frac{\pi R^2}{\Omega_{35}} \frac{dL}{dt} \quad (6.2)$$

where J_5^{eff} is the effective flux of As atoms to the droplet (including adsorption, desorption, and possible re-emitted flux of As atoms). We do not count the surface diffusion of highly volatile As atoms along the NW sidewalls.

The volume of the Ga droplet is given by:

$$V = \frac{1}{3} \pi f(\beta) R^3 \quad (6.3)$$

where $f(\beta) = (1 - \cos \beta)^2(2 + \cos \beta)/\sin^3 \beta$ is a geometrical function relating the volume of a spherical cap to the radius of its base with a droplet contact angle β . An excessive Ga influx leads to an inflation of the Ga droplet:

$$\frac{dV}{dt} = \Omega_3 \left(\frac{dN_3}{dt} - \frac{dN_5}{dt} \right) > 0 \quad (6.4)$$

where $\Omega_3 = 0.02 \text{ nm}^3$ is the Ga atomic volume in the liquid phase.

According to the results of [6.23], Ga droplets on top of self-catalyzed GaP NWs exhibit a constant value of β around 123° regardless of the NW shape (vertical, tapered or inverse-tapered). Similar surface energies of the GaAs and GaP VLS system provide similar stable contact angles [6.28, 6.32]. Assuming β is constant (independent of R) and combining (6.1) to (6.4) gives [6.30, 6.31]:

$$\frac{dR}{dt} = A + \frac{B}{R} \quad (6.5)$$

where

$$A = \frac{\Omega_3}{f(\beta)} (J_3^{eff} - J_5^{eff}) \quad (6.6)$$

$$B = \frac{\Omega_3}{f(\beta)} \frac{2\lambda J_3 \sin \alpha_3}{\pi} \left(1 - \frac{\theta_l}{\theta_s} \right) \quad (6.7)$$

In general, the parameter A in (6.6) can be of either sign. When $A < 0$, or $J_5^{eff} > J_3^{eff}$, more Ga atoms are removed from the droplet due to crystallization than supplied from the vapor. Equation (6.5) then has a stationary solution at $R_s = -B/A$. For all NWs with initial top radius lower (greater) than R_s , the Ga droplet will inflate (shrink) until reaching the steady-state value R_s . This is referred to as radial “self-focusing” [6.30].

A completely different situation occurs when $A > 0$, or $J_3^{eff} > J_5^{eff}$. In this case, the droplet swells indefinitely with the help of surface diffusion. However, the

experimental data indicates that the radial growth eventually becomes linear after the droplet inflation (dR/dt is constant), which implies that the B term is negligible. In this case, the solution of (6.5) can be expressed as $R(t) = R_0 + At$, similar to [6.31].

The instantaneous change of V/III flux ratio from 2 to 1 means the influx of Ga atoms suddenly becomes greater than the influx of group V atoms. Thus, the droplet rapidly inflates as observed in Fig. 6.1(b). This corresponds to A changing sign and taking a new fixed value. Decreasing the As flux leads to a reduction of As concentration in the liquid phase until a certain stationary concentration is reached. Weak differences in As concentration relates to strong variation of chemical potential [6.32]. Furthermore, the result of declining As concentration is increasing Ga concentration. From (6.7), $B \sim \theta_s - \theta_l = \theta_s - \exp(\mu_3)$, where μ_3 is the chemical potential of Ga atoms in the droplet in units of $k_B T$. We assume that after the V/III flux change, a rapid diameter expansion correlates with the achievement of steady-state conditions until B is equal to zero. In other words, when the steady-state condition is achieved, the difference $[1 - \theta_l/\theta_s]$ in (6.7) becomes equal to zero, and the reverse diffusion from the droplet equals the Ga adatom surface diffusion from the NW sidewalls.

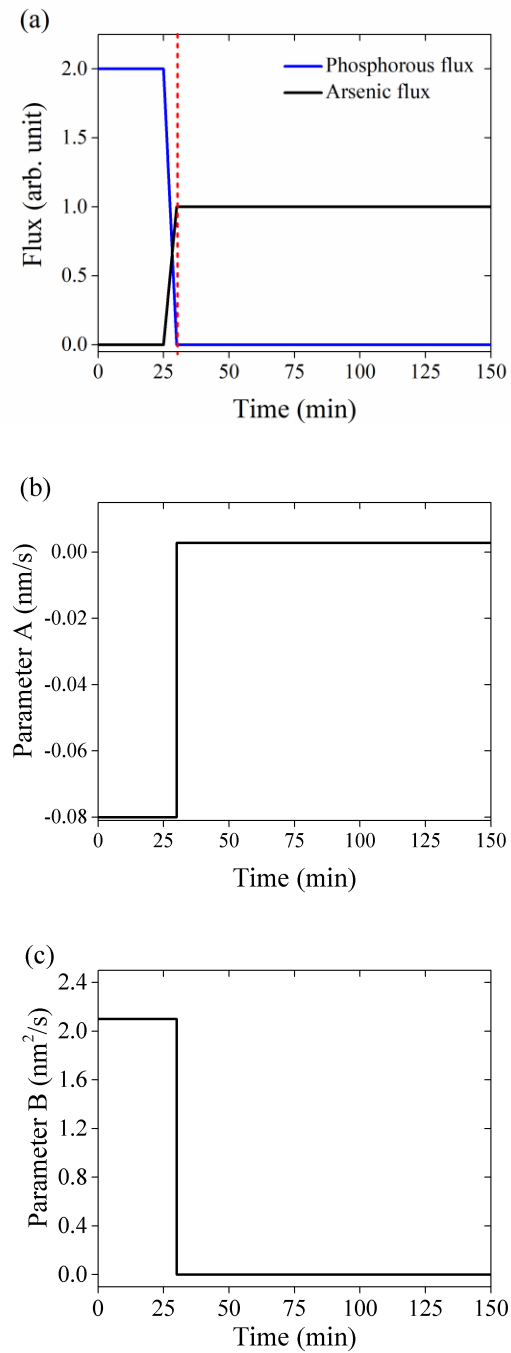


Figure 6.3. (a) P and As flux for sample B. The red dashed line indicates the time when the V/III flux ratio was changed from 2 to 1. (b) Progression of parameter A with time. (c) Progression of parameter B with time.

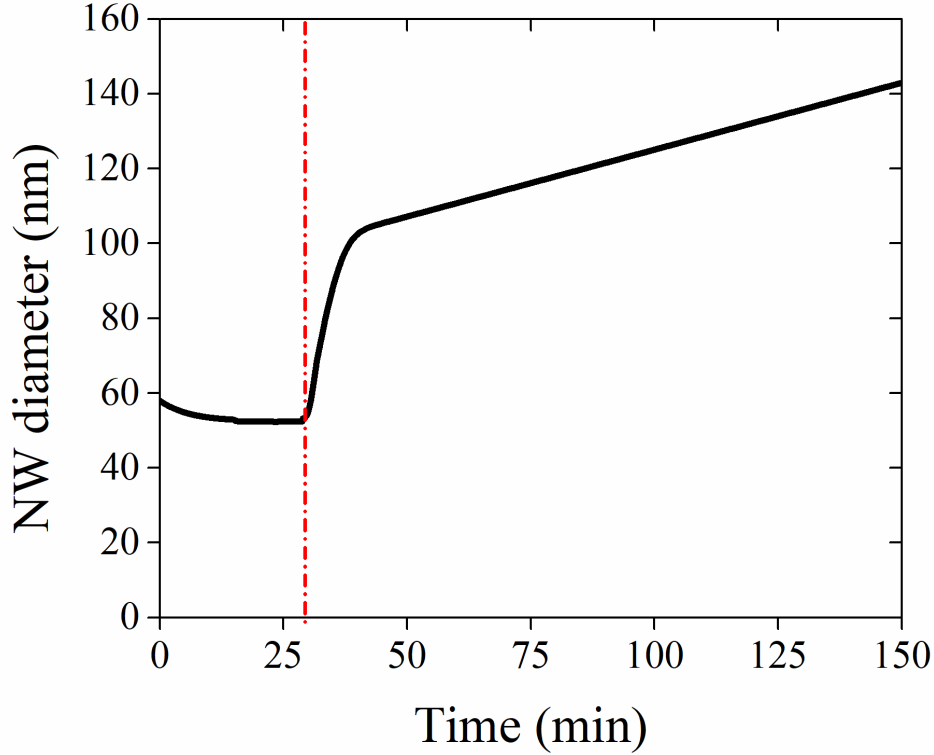


Figure 6.4. Model prediction of the NW diameter versus time. The red dashed line indicates the time when the V/III flux ratio was changed from 2 to 1.

Using measured values of the NW diameter, steady-state values for the parameters A and B can be estimated both before and after the change in V/III flux ratio from 2 to 1. The initial NW radius before the droplet expansion with a V/III flux ratio of 2 was $R \sim 26$ nm, corresponding to R_S . In our MBE system, $\alpha_3 = 35^\circ$ and we estimate $\lambda = 750$ nm [6.28]. We assume that reverse diffusion of Ga adatoms from the droplet to the NW sidewalls is negligible before and during the ramp stage. Consequently, $B = 2.1$ nm²/s from (6.7), and $A = -B/R_S \sim -0.08$ nm/s. The effective flux imbalance from (6.6) is $I_3^{eff} - I_5^{eff} = -0.37$

nm/s, where $I_{eff} = J_{eff}\Omega$. For a V/III flux ratio of 1, the value of parameter A can be estimated from the linear diameter evolution after the droplet expansion. This gives $A = 0.0028$ nm/s and an effective flux imbalance of $I_3^{eff} - I_5^{eff} = 0.53$ nm/s. As mentioned above, we assume B tends to zero after the droplet expansion for the V/III flux of 1. Fig. 6.3(b) and Fig. 6.3(c) illustrate the parameters A and B versus time. Using these parameter values, (6.5) to (6.7) were solved for the NW diameter using variable-step, variable-order (VSVO) Adams-Bashforth-Moulton PECE solver of orders 1 to 13 [6.33] and time step equal to 0.9 seconds. The NW diameter versus time is shown in Fig. 6.4, which reproduces the NW morphology observed in Fig. 6.1(b).

6.4.2. Light Absorption Model

To determine if the tapered NW morphology of Fig. 6.1(c) is suitable for PV devices, a numerical study of optical absorptance was performed by finite element analysis using COMSOL Multiphysics. GaAs NWs were modeled with circular cross-section and 2 μm length with either straight or tapered sidewalls on a Si substrate. The incident light spectrum was weighted according to the AM 1.5D spectrum with right circular polarization. A single NW unit cell was modeled with periodic Floquet boundary conditions, thereby simulating a NW array. Perfectly matched layers (PML) were placed above and below the NW geometry to model infinite layers of air and Si substrate. The light absorption and photocurrent density from the inverse-tapered NW was compared with that from the NW with straight sidewalls. The straight NW model had a constant diameter of 170 nm and periodic spacing of 320 nm, suitable for strong absorption of the AM1.5D

spectrum [6.3, 6.7–6.10]. For the tapered NW, the top diameter was 170 nm while the bottom was only 100 nm with linear tapering as observed in Fig. 6.1(c).

Previous studies [6.1, 6.8–6.10], [6.33–6.43] have shown that NWs support HE_{11} optical resonant modes, dependent on the NW diameter. For GaAs, the HE_{11} resonance wavelength red-shifts by 3.27 nm per nm of diameter increase [6.1]. This means that a NW with a continuous variation of diameter can more effectively couple to a broader wavelength range, as compared to a NW of constant diameter. Indeed, numerical studies of inverse-tapered NW structures have indicated improved light absorption [6.44, 6.45].

Fig. 6.5 shows the contribution to optical absorptance due to consecutive 500 nm segments from the top of the straight NW (solid lines) and tapered NW (dashed lines). The greatest absorptance occurs in the top 500 nm of both NWs. The absorptance spectrum at 500 nm is similar for both NW geometries except for the peak at ~ 725 nm. This peak exhibits greater absorptance and is slightly blue-shifted in the tapered as compared to the straight NW. The slight blue-shift of this peak in the tapered NW is due to the shrinking diameter of the NW towards the NW base which has allowed shorter wavelengths to couple more effectively into the HE_{11} resonance mode of the NW.

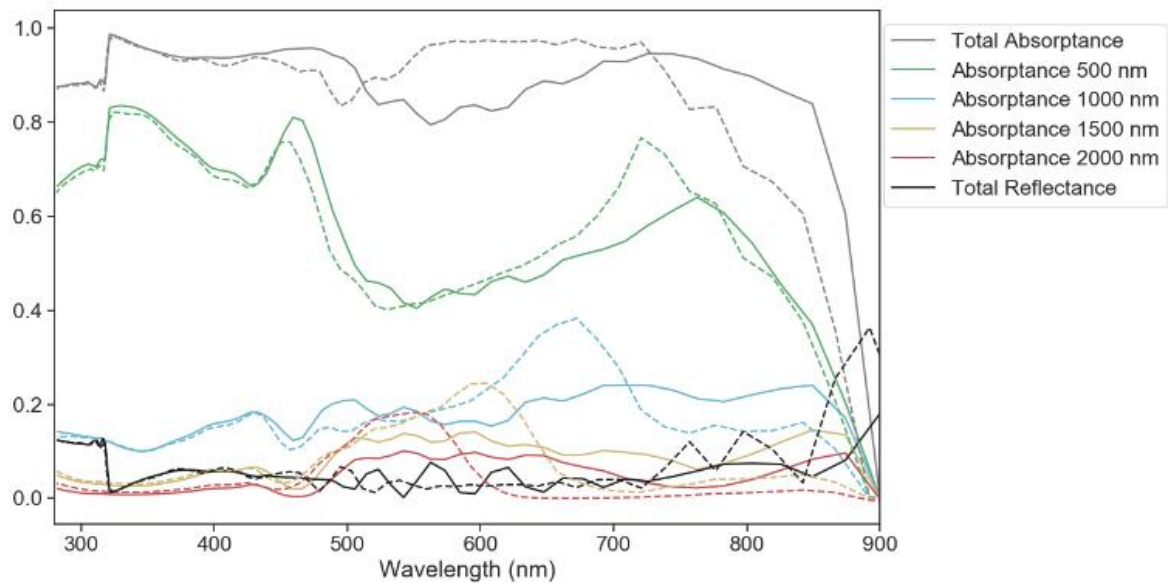


Figure 6.5. Theoretical absorptance in straight NWs (solid lines) and tapered NWs (dashed lines) due to consecutive 500 nm segments. ‘500 nm’ represents the segment at the top of the NW and ‘2000 nm’ represents the segment at the base of the NW. The total absorptance and reflectance is also indicated.

Further along the length of the NW (from the top), additional peaks appear in the absorptance spectrum (Fig. 6.5) for the tapered NW which were not present in the straight NW. These peaks progressively blue-shift with increasing depth into the NW, as expected due to the shift of the HE_{11} mode with diameter. Absorption peaks were observed in the tapered NW at approximately 550, 600, 675, and 725 nm at depths of 2000, 1500, 1000, and 500 nm, respectively. The generation rate of electron and holes due to photon absorption associated with the aforementioned peaks were examined as shown in Fig. 6.6. In each of the straight NW profiles, the generation rate is greatest at the top of the NW but

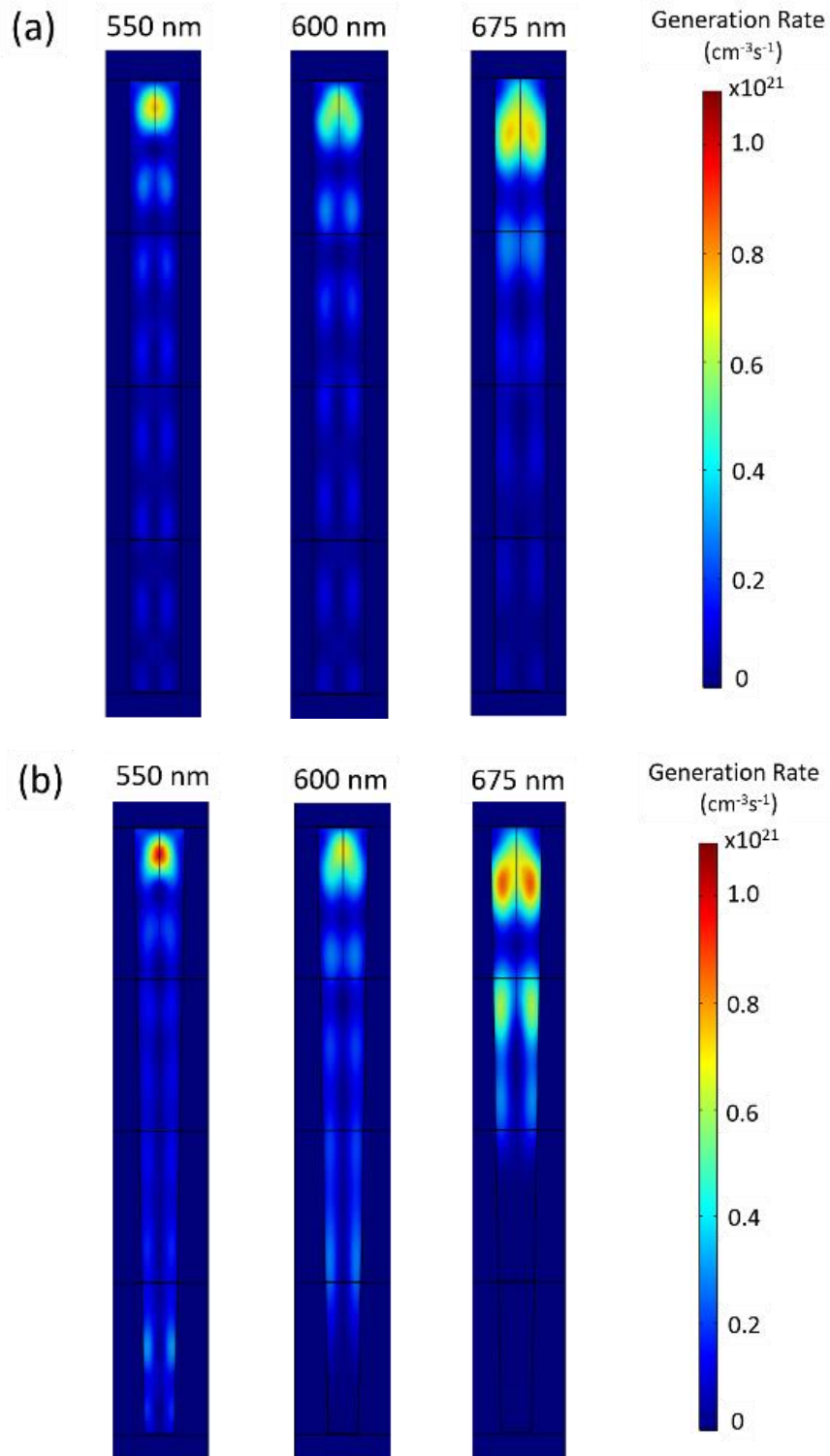


Figure 6.6. Generation rate in (a) straight and (b) inverse-tapered NWs.

attenuates gradually down its length. In the tapered NWs, for the wavelength values examined, the field does not attenuate as strongly. Future work will corroborate these theoretical results with experimental measurements.

The expected photocurrent density due to solar absorption was determined to further assess the difference between the tapered and straight NWs. The photocurrent density is calculated by integrating over the volume of the NWs according to Eq. (7) in Ref. [6.10] where the generation rate is given by Eq. (1) in Ref. [6.8] and we assume each absorbed photon generates one electron-hole pair that is collected at the contacts. Additional losses due to surface or bulk recombination were not included. The photocurrent densities given here therefore represent the theoretical maximum that the NW could achieve. The straight NW only slightly outperformed the tapered NW with a photocurrent density of 25.6 mA/cm² and 24.7 mA/cm², respectively. Hence, the tapered NW is able to maintain 96% of the photocurrent of the straight NW with only 64% of its volume. For reference, the maximum photocurrent density for GaAs under the AM1.5D spectrum is 29 mA/cm².

6.5. Conclusions

We have shown that the most effective way of obtaining wide diameter NWs is to controllably inverse-taper the structures to create NWs with thin bases and wide tops. The thinner base is advantageous because the diameter lies below the critical diameter for misfit dislocations. Controlling diameter through the droplet presents the possibility of adjusting the diameter throughout the growth process, allowing for more complex NW structures. A

comparison of inverse-tapered NWs with straight NWs indicated that they are capable of giving comparable optical absorptance. The inverse-tapered NWs simulated in this study were able to achieve 96% of the photocurrent generated in the straight NWs with only 64% of the volume. The funnel shaped NWs would work well for direct integration with a Si cell in a multi-junction photovoltaic device as presented in Ref. [6.47, 6.48].

6.6. References

- [6.1] K. M. Azizur-Rahman and R. R. LaPierre, “Wavelength-selective absorptance in GaAs, InP and InAs NW arrays,” *Nanotechnol.*, vol. 26, no. 29, 2015, Art. no. 295202.
- [6.2] N. I. Goktas et al., “Nanowires for energy: A review,” *Appl. Phys. Rev.*, vol. 5, no. 4, 2018, Art. no. 041305.
- [6.3] R. R. LaPierre et al., “III-V nanowire photovoltaics: Review of design for high efficiency,” *Phys. Status Solidi RRL*, vol. 7, no. 10, pp. 815–830, 2013.
- [6.4] C. J. Goosney, V. M. Jarvis, D. P. Wilson, N. I. Goktas, and R. R. LaPierre, “InSb nanowires for multispectral infrared detection,” *Semicond. Sci. Technol.*, vol. 34, no. 3, 2019, Art. no. 035023.
- [6.5] R. R. LaPierre, M. Robson, K. M. Azizur-Rahman, and P. Kuyanov, “A review of III-V nanowire infrared photodetectors and sensors,” *J. Phys. D: Appl. Phys.*, vol. 50, no. 12, 2017, Art. no. 123001.

- [6.6] Y. Zhang, J. Wu, M. Aagesen, and H. Liu, “III–V nanowires and nanowire optoelectronic devices,” *J. Phys. D: Appl. Phys.*, vol. 48, no. 46, 2015, Art. no. 463001.
- [6.7] G. Otnes and M. T. Borgström, “Towards high efficiency nanowire solar cells,” *Nano Today*, vol. 12, pp. 31–45, 2017.
- [6.8] A. H. Trojnar, C. E. Valdivia, R. R. LaPierre, K. Hinzer, and J. J. Krich, “Optimizations of GaAs nanowire solar cells,” *IEEE J. Photovolt.*, vol. 6, no. 6, pp. 1494–1501, 2016.
- [6.9] K. W. Robertson, R. R. LaPierre, and J.J. Krich, “Accurate wave optics modeling of nanowire solar cells using rigorous coupled wave analysis,” *Opt. Express*, vol. 27, no. 4, pp. A133–A147, 2019.
- [6.10] Y. Hu, R. R. LaPierre, M. Li, K. Chen, and J.-J. He, “Optical characteristics of GaAs nanowire solar cells,” *J. Appl. Phys.*, vol. 112, no. 10, 2012, Art. no. 104311.
- [6.11] M. H. T. Dastjerdi, J. P. Boulanger, P. Kuyanov, M. Aagesen, and R. R. LaPierre, “Methods of Ga droplet consumption for improved GaAs nanowire solar cell efficiency,” *Nanotechnol.*, vol. 27, no. 47, 2016, Art. no. 475403.
- [6.12] J. P. Boulanger et al., “Characterization of a Ga-assisted GaAs nanowire array solar cell on Si substrate,” *IEEE J. Photovolt.*, vol. 6, no. 3, pp. 661–667, 2016.
- [6.13] I. Aberg et al., “A GaAs nanowire array solar cell with 15.3% efficiency at 1 Sun,” *IEEE J. Photovolt.*, vol. 6, no. 1, pp. 185–190, 2016.
- [6.14] J. Wallentin et al., “InP nanowire array solar cells achieving 13.8% efficiency by exceeding the ray optics limit,” *Science*, vol. 339, no. 6123, pp. 1057–1060, 2013.

- [6.15] K. L. Kavanagh, “Misfit dislocations in nanowire heterostructures,” *Semicond. Sci. Technol.*, vol. 25, no. 2, 2010, Art. no. 024006.
- [6.16] F. Glas, “Critical dimensions for the plastic relaxation of strained axial heterostructures in free-standing nanowires,” *Phys. Rev. B*, vol. 74, no. 12, 2006, Art. no. 121302.
- [6.17] A. Biermanns, S. Breuer, A. Trampert, A. Davydok, L. Geelhaar and U Pietsch, “Strain accommodation in Ga-assisted GaAs nanowires grown on silicon (111),” *Nanotechnol.*, vol. 23, 2012, Art. no. 305703.
- [6.18] F. Matteini et al., “Impact of the Ga droplet wetting, morphology, and pinholes on the orientation of GaAs nanowires,” *Cryst. Growth Des.*, vol. 16, no. 10, pp. 5781–5786, 2016.
- [6.19] H. Potts, N. P. Morgan, G. Tütüncüoğlu, M. Friedl, and A. Fontcuberta i Morral, “Tuning growth direction of catalyst-free InAs(Sb) nanowires with indium droplets,” *Nanotechnol.*, vol. 28, no. 5, 2016, Art. no. 054001.
- [6.20] E. Russo-Averchi et al., “Suppression of three dimensional twinning for a 100% yield of vertical GaAs nanowires on silicon,” *Nanoscale*, vol. 4, no. 5, pp. 1486–1490, 2012.
- [6.21] S. Plissard, G. Larrieu, X. Wallart, and P. Caroff, “High yield of self-catalyzed GaAs NW arrays grown on silicon via gallium droplet positioning,” *Nanotechnol.*, vol. 22, no. 27, 2011, Art. no. 275602.

- [6.22] E. D. Leshchenko, P. Kuyanov, R. R. LaPierre, and V. G. Dubrovskii, “Tuning the morphology of self-assisted GaP nanowires,” *Nanotechnol.*, vol. 29, no. 22, 2018, Art. no. 225603.
- [6.23] P. Kuyanov, J. Boulanger, and R. R. LaPierre, “Control of GaP nanowire morphology by group V flux in gas source molecular beam epitaxy,” *J. Cryst. Growth*, vol. 462, pp. 29–34, 2017.
- [6.24] COMSOL, *RF Module User's Guide v. 5.3*, Stockholm, Sweden: COMSOL AB, 2017.
- [6.25] H. Kupers et al., “Diameter evolution of selective area grown Ga-assisted GaAs nanowires,” *Nano Res.*, vol. 11, no. 5, pp. 2885–2893, 2018.
- [6.26] S. J. Gibson and R. R. LaPierre, “Model of patterned self-assisted nanowire growth,” *Nanotechnol.*, vol. 25, no. 41, 2014, Art. no. 415304.
- [6.27] L. A. Bitzer et al., “Modelling of electron beam induced nanowire attraction,” *J. Appl. Phys.*, vol. 119, no. 14, 2016, Art. no. 145101.
- [6.28] V. G. Dubrovskii et al., “Self-equilibration of the diameter of Ga-catalyzed GaAs nanowires,” *Nano Lett.*, vol. 15, no. 8, pp. 5580–5584, 2015.
- [6.29] G. A. Priante, S. Ambrosini, V. G. Dubrovskii, A. Franciosi, and S. Rubini, “Stopping and resuming at will the growth of GaAs nanowires,” *Cryst. Growth Des.*, vol. 13, no. 9, pp. 3976–3984, 2013.
- [6.30] V. G. Dubrovskii et al., “Narrowing the length distribution of Ge nanowires,” *Phys. Rev. Lett.*, vol. 108, no. 10, 2012, Art. no. 105501.

- [6.31] V. G. Dubrovskii et al., “Gibbs-Thomson and diffusion-induced contributions to the growth rate of Si, InP, and GaAs nanowires,” *Phys. Rev. B*, vol. 79, no. 20, 2009, Art. no. 205316.
- [6.32] F. Glas, M. R. Ramdani, G. Patriarche, and J. C. Harmand, “Predictive modeling of self-catalyzed III-V nanowire growth,” *Phys. Rev. B*, vol. 88, no. 19, 2013, Art. no. 195304.
- [6.33] L.F. Shampine and M.K. Gordon, *Computer solution of ordinary differential equations: the initial value problem*. San Francisco: W. H. Freeman, 1975.
- [6.34] N. Anttu and H. Q. Xu, “Coupling of light into nanowire arrays and subsequent absorption,” *J. Nanosci. Nanotechnol.*, vol. 10, no. 11, pp. 7183–7187, 2010.
- [6.35] N. Anttu et al., “Absorption of light in InP nanowire arrays,” *Nano Res.*, vol. 7, no. 6, pp. 816–823, 2014.
- [6.36] P. Kailuweit et al., “Numerical simulations of absorption properties of InP nanowires for solar cell applications,” *Prog. Photovolt: Res. Appl.*, vol. 20, no. 8, pp. 945–953, 2012.
- [6.37] N. Anttu and H. Q. Xu, “Efficient light management in vertical nanowire arrays for photovoltaics,” *Opt. Express*, vol. 21, no. 103, pp. A558–A575, 2013.
- [6.38] J. Kupec, R. L. Stoop, and B. Witzigmann, “Light absorption and emission in nanowire array solar cells,” *Opt. Express*, vol. 18, no. 26, pp. 27589–27605, 2010.
- [6.39] H. Guo, L. Wen, X. Li, Z. Zhao, and Y. Wang, “Analysis of optical absorption in GaAs nanowire arrays,” *Nanoscale Res. Lett.*, vol. 6, no. 1, 2011, Art. no. 617.

- [6.40] N. Dhindsa et al., “Highly ordered vertical GaAs nanowire arrays with dry etching and their optical properties”, *Nanotechnol.*, vol. 25, no. 30, 2014, Art. no. 305303.
- [6.41] P. M. Wu, N. Anttu, H. Q. Xu, L. Samuelson, and M. E. Pistol, “Colorful InAs nanowire arrays: From strong to weak absorption with geometrical tuning,” *Nano Lett.*, vol. 12, no. 4, pp. 1990–1995, 2012.
- [6.42] L. Cao et al., “Engineering light absorption in semiconductor nanowire devices,” *Nat. Mater.*, vol. 8, no. 8, 2009, Art. no. 643.
- [6.43] B. Wang and P. W. Leu, “Tunable and selective resonant absorption in vertical nanowires,” *Opt. Express*, vol. 37, no. 18, pp. 3756–3758, 2012.
- [6.44] K. T. Fountaine, W. S. Whitney, and H. A. Atwater, “Resonant absorption in semiconductor nanowires and nanowire arrays: Relating leaky waveguide modes to Bloch photonic crystal modes,” *J. Appl. Phys.*, vol. 116, no. 15, 2014, Art. no. 153106.
- [6.45] G. Shalev, S. W. Schmitt, H. Embrechts, G. Bronstrup, and S. Christiansen, “Enhanced photovoltaics inspired by the fovea centralis,” *Sci. Rep.*, vol. 5, 2015, Art. no. 8570
- [6.46] A. Prajapati, Y. Nissan, T. Gabay, and G. Shalev, “Light trapping with silicon light funnel arrays,” *Materials*, vol. 11, no. 3, 2018, Art. no. 445.
- [6.47] R.R. LaPierre, “Theoretical conversion efficiency of a two-junction nanowire on Si solar cell,” *J. Appl. Phys.*, vol. 110, 2011, Art. no. 014310.

- [6.48] J.P. Boulanger, A.C.E. Chia, B. Wood, S. Yazdi, T. Kasama, M. Aagesen and R.R. LaPierre, “Characterization of a Ga-assisted GaAs nanowire array solar cell on Si substrate,” *IEEE J. Photovoltaics*, vol. 6, pp. 661-667, 2016.

7. Optimizing Tapered Nanowires for Photovoltaic Applications

7.1. Summary

This chapter presents work previously published as “Simulation of optical absorption in conical nanowires” (D. P. Wilson and R. R. LaPierre, *Opt. Express*, vol. 29, no. 6, pp. 9544-9552, 2021., DOI: 10.1364/OE.419535). In the previous chapter, an inverted cone shape was suggested as a way of achieving the large top diameters needed for optimized optical absorption in photovoltaic nanowires (NWs). These structures were demonstrated experimentally by altering the V/III ratio during MBE growth. Simulations were performed comparing an optimized NW with straight sidewalls to a tapered NW with the same top diameter. This comparison showed similar photocurrent could be generated from both.

A more thorough optimization is presented to examine the potential of inverted conical NWs. The conical NW top diameter was optimized for three different base diameters, creating a range of shapes from conical (larger base diameter) to inverse conical (larger top diameter). The reflectance and transmittance were compared for all the shapes. The conical design had a lower overall reflectance, whereas the inverse conical NWs had to balance the contributions to reflectance from the flat top as well as from the substrate. The total photocurrent depends on the total volume available for absorption, as well as the top and base diameters, which can affect the reflectance and transmittance.

For a top diameter above ~170 nm, the photocurrent produced by all geometries is similar, meaning there is little disadvantage in using an inverted conical geometry if the

necessary top diameters can be produced through MBE growth techniques. Inverted conical NWs may be desirable over conical NWs for producing higher yields and lattice relaxed interfaces.

7.2. Introduction

Semiconductor nanowires (NWs) are being investigated for applications in photonic and optoelectronic devices [7.1-7.4]. In particular, the optical absorption in cylindrical III-V NW arrays has been investigated predominantly for GaAs [7.5-7.9] and InP material [7.10-7.13] mainly for photovoltaic applications. Control of the shape, size, and positioning of NWs are critical factors that determine device performance. Simulations indicate that the optimal absorption of the solar spectrum in cylindrical GaAs and InP NWs for normal light incidence (AM1.5G simulated solar spectrum) occurs when the NW diameter is ~180 nm, the pitch (separation between NWs) is ~360 nm, and the NW length is ~2 μm [7.5-7.13]. With the optimum NW geometry, the absorptance exceeds 90% over the visible spectrum, which is much higher than that of thin films with thickness equal to the NW length and excluding an anti-reflection coating. The improvement in optical absorptance of NW arrays as compared to thin films is due to the presence of leaky mode resonances (LMRs) within the NWs [7.14, 7.15]. The HE_{1n} set of modes can efficiently couple to vertically standing NWs, resulting in an optical antenna effect [7.16-7.18]. These modes produce resonant absorption peaks which shift to longer wavelengths with increasing NW diameter to satisfy the electromagnetic boundary conditions [7.14, 7.15].

This phenomenon can be used to create wavelength selectivity for multispectral photodetectors [7.19, 7.20] or broadband absorption for solar photovoltaic cells [7.21].

Generally, NWs with cylindrical cross-section have been studied with a few notable exceptions such as elliptical, square, hexagonal and triangular cross-sections where relatively minor differences in absorption were noted [7.22-7.25]. Also, the symmetry of the array lattice (typically square or hexagonal) has little effect on optical absorption for large inter-NW separations where there is negligible coupling of optical modes between adjacent NWs. A uniform array of cylindrical NWs of constant diameter may not be the optimum geometry to maximize optical absorptance. For example, to further improve absorption efficiency, arrays containing NWs with multiple diameters have been investigated [7.26-7.30]. More complicated morphologies, such as periodic diameter modulation in NWs, has also been investigated [7.31, 7.32]. Another fruitful approach to improving optical absorptance involves tuning the NW morphology. Rather than a discrete set of NW diameters, it is possible to vary the diameter of NWs continuously in a tapered morphology. Nanocones, frustum nanocones, or related shapes [7.33-7.41] can improve optical absorption as compared to NWs with a constant diameter due to less reflection from the smaller top diameter and less transmission due to the larger base diameter. The gradual increase in diameter of the nanocones acts as a gradual refractive index profile that improves antireflection. Finally, the expanding diameter of the nanocone broadens the HE_{1n} resonance absorption peaks, improving the broadband absorption. Alternatively, inverted frustum nanocone arrays (sometimes called light funnels) [7.42-7.45] or related structures [7.46, 7.47] have recently been proposed, inspired by the working principle of

the human retina [7.42, 7.48]. The inverted nanocones can provide enhanced optical absorption compared to NWs due to the support of multiple optical modes.

NWs can be grown by either top-down etching or bottom-up growth methods [7.49]. Wet and dry etching methods are commonly used for the top-down fabrication of NWs. For example, NWs have been selectively etched with doping-dependent etchants [7.32]. Reactive ion etching (RIE) has also been used to fabricate cylindrical [7.50], conical [7.27, 7.40] and inverted conical NWs [7.42]. However, the performance of NW devices produced by etching may be limited by the resulting surface roughness and high density of surface states. Alternatively, NWs may be produced by bottom-up growth with smooth sidewall facets and passivated by shell growth [7.51]. Impurity dopants can also be incorporated during growth of the NWs, in either an axial or core-shell geometry, to produce electrically active NW diodes. Bottom-up grown NWs are typically produced by epitaxy using the vapor-liquid-solid (VLS) method where seed particles, typically metallic droplets, are used to collect and nucleate the growth species into a NW array [7.49]. GaAs NWs can be grown by the self-assisted growth method where growth is seeded by a Ga droplet. The diameter of the NWs can be controlled by the size of the Ga droplet. Various NW morphologies, such as tapered, straight (cylindrical), or inverse tapered NWs, are possible by controlling the Ga droplet continuously during growth. For example, we recently showed that an inverted nanocone morphology could be achieved in GaAs NWs during molecular beam epitaxy (MBE) by controlling the Ga droplet size via growth conditions [7.52]. The inverted conical morphology is particularly advantageous because the small base diameter can be less than the critical diameter for misfit dislocations due to

the lattice-mismatch between NWs and their substrate (e.g., GaAs NWs on Si), while the top diameter can be tuned for optimum absorptance of incident light. Here, we examine the optical absorptance in GaAs NWs for conical, straight and inverted conical morphologies (frustum nanocones), and optimize the geometry for absorption of the simulated solar spectrum.

7.3. Methods

The optical absorptance spectrum from 300 nm to 900 nm was simulated by the finite element method (FEM) using the RF module in COMSOL Multiphysics 5.3A software. The FEM is a popular choice of solver, which is well suited for NW designs of arbitrary shape [7.53]. The electric field of the NWs was simulated using left-hand circularly polarized light with incident power weighted by the AM1.5D simulated solar spectrum [7.54].

The geometric unit cell was periodic in the x and y directions (z is along the length of the NW), simulating a square array of NWs. A port boundary is placed in the space above the NW to simulate the incoming wave. The reflected and transmitted power are found by integrating the power flowing through xy planes. Reflection is measured in the plane directly above the port boundary (which is transparent to the reflected wave), and transmitted power is obtained at several planes spaced evenly along the length of the NW. Perfectly matched layers (PMLs) were placed at the top and bottom of the NW geometry to absorb the reflected and transmitted light. The simulated geometry is shown in Figure 7.1(d). The model geometry consisted of a GaAs NW sitting on a 500 nm slab of Si and

surrounded by vacuum. As illustrated in Figure 7.1, three NW morphologies were examined by varying the top and base NW diameter: a frustum cone (referred to as conical

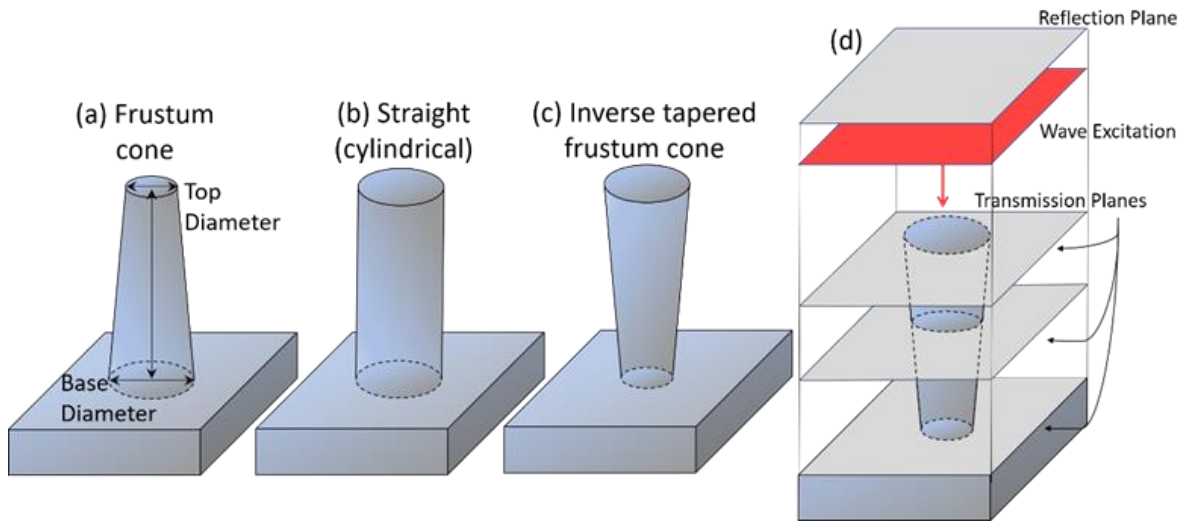


Figure 7.1. (a-c) Definition of NW morphologies. (b) Schematic of source, reflection and transmission planes.

NWs), a straight (cylindrical) NW, and an inverted frustum cone (referred to as inverted conical NWs). The materials were defined by their wavelength-dependent refractive indices [7.55]. The NW pitch was fixed at 320 nm since this value was previously shown to produce optimum solar absorption for cylindrical NWs [7.1]. The top diameters were varied between 50 nm and 290 nm for one of three fixed base diameters: 50 nm, 100 nm and 200 nm. The 50 nm and 100 nm base diameters are particularly relevant because they are below the theoretical critical diameter for misfit dislocations in GaAs NWs on Si [7.56]. The NWs had a length of 1000 nm or 2000 nm.

7.4. Results and Discussion

Figure 7.2 shows the simulated absorptance spectra for NWs with a base diameter of 100 nm and a length of 2000 nm. The NW top diameter is given above each plot. The spectra have been subdivided into contributions from incremental segments of 500 nm length (segments A, B, C and D, from the top to the bottom of the NW, respectively). The total absorptance from the full 2000 nm length of the NW is shown as the black curves in Figure 7.2. The top diameter of 50, 70 and 90 nm give a conical NW morphology, while all other top diameters (>100 nm) give an inverted conical NW morphology. Figure 7.2 also shows the simulated absorptance spectrum for a 2000 nm thick GaAs thin film for comparison with the NWs.

Starting with a top diameter of 50 nm (top left panel of Figure 7.2), the main absorption peak in each segment (A, B, C, D) is attributed to the HE_{11} resonance mode as confirmed by field patterns (for example, see Figure 7.5 of the Supplementary Material). For NWs with top diameter exceeding about 70 nm, the greatest contribution to the optical absorption occurs from the top 500 nm of the NW (segment A, green curves of Figure 7.2). The HE_{11} absorption peak of segment A (green curves) continuously red-shifts as the NW top diameter increases from 70 nm to 290 nm. Below a top diameter of 110 nm, where the NW morphology is conical, the HE_{11} mode also red-shifts as the diameter increases from the top of the NW (segment A) to the bottom of the NW (segment B). This red-shift with

increasing NW diameter is expected for the HE_{1n} modes due to the dispersion relation that arises from the electromagnetic boundary conditions [7.14, 7.15, 7.19, 7.20].

As the NW top diameter increases, higher order modes are introduced (for example, the peak at 445 nm for a top diameter of 170 nm is an HE_{12} mode; see Figure 7.6 of the Supplementary Material). The higher order modes red-shift with NW top diameter and tapering, and begin to dominate the absorption spectrum above a top diameter of 170 nm. Mode coupling is expected as the NW top diameter approaches the pitch between NWs.

The introduction of higher order HE_{1n} modes, the red-shift of the HE_{1n} modes along the NW length due to NW tapering, and the red-shift of the modes due to increase of the overall NW diameter, all contribute to a broadening of the absorption spectrum in conical NWs as compared to NWs with a constant diameter. Similar trends are presented in the Supplementary Material (Figure 7.7-Figure 7.11) for different NW base diameters (50, 200 nm) and a different NW length (1000 nm). This broadening of the absorption spectrum is advantageous for solar photovoltaic energy conversion. It is noteworthy that the maximum in the total absorptance spectrum of the NWs exceeded that from the thin film in all cases due to the optical modes in the NWs.

In addition to the mode peaks, periodic ripples of small amplitude are observed in the total absorptance spectra of Figure 7.2, particularly at large top diameters. These oscillations are due to multiple reflections from the top (GaAs/air interface) and base (GaAs/Si interface) of the NW forming a Fabry-Perot cavity. The period of the ripples increases with decreasing NW length, consistent with F-P modes (compare Figure 7.2 (2000 nm length) with Figure 7.9 (1000 nm length) in the Supplementary Material).

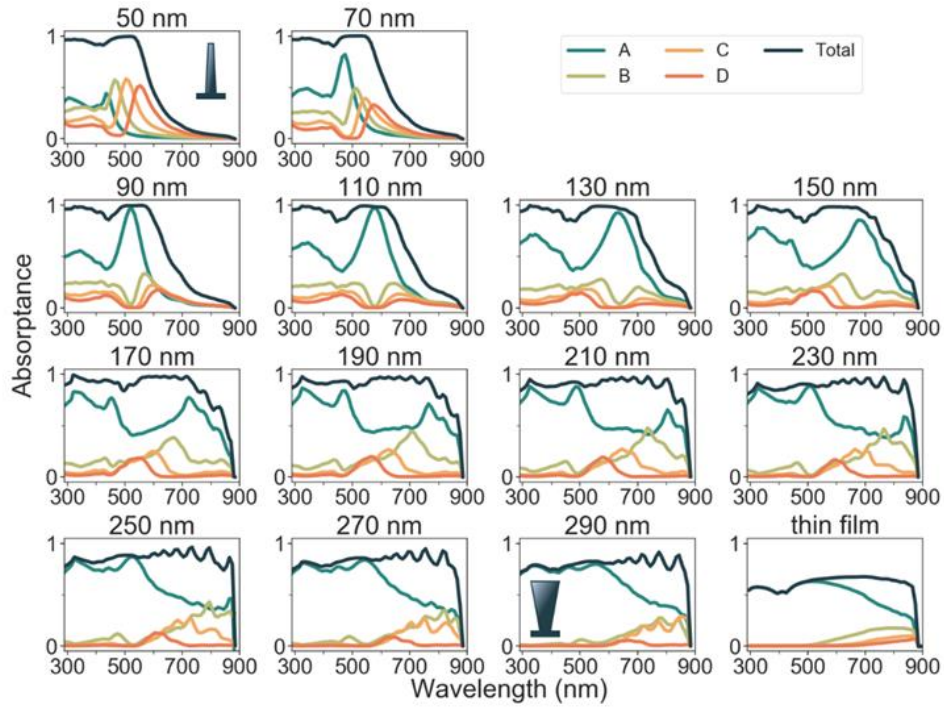


Figure 7.2. Absorbance spectra for NWs with a base diameter of 100 nm and a length of 2000 nm. The NW top diameter is given above each plot. Insets in the 50 nm and 290 nm panels illustrate a typical NW profile. The spectra have been subdivided into the contributions to absorbance from incremental segments of 500 nm length where A is the top 500 nm and D is the bottom 500 nm. The absorbance spectrum of a thin film is also shown.

Figure 7.3 shows the total reflectance and transmittance from the NWs (averaged over all wavelengths from 300-900 nm). The reflectance is given by:

$$R_{tot} = \frac{1}{N} \sum \frac{P_{ref}(\lambda)}{P_{in}(\lambda)} \quad (7.1)$$

where P_{ref} is the reflected power, P_{in} is the incident power at each simulated wavelength, and N is the number of wavelength increments in the summation (wavelength increment was 10 nm). Here, P_{in} is constant, not weighted by the solar spectrum. A similar calculation was performed for the transmittance where the transmitted power is measured in the plane at the base of the NW. A horizontal line representing the reflectance and transmittance from a thin film without any anti-reflection coating is also shown in Figure 7.3.

As the NW top diameter increases, the reflectance approaches that of the GaAs thin film due to increasing reflectance from the top of the NWs. Conversely, as the NW top diameter decreases, there is an increasing contribution to reflectance from the exposed Si/air interface between the NWs. Consequently, NWs with small base diameters of 50 nm or 100 nm have a minimum reflectance near 170 nm, which can be understood as a balance between reflectance from the NW top and the substrate. As the base of the NW becomes thinner, the substrate surface can contribute more strongly to the reflection. This contribution from the substrate is evident in Figure 7.3(a) by the greater reflectance for a 50 nm base diameter as compared to a 100 nm base diameter when the top diameter is below 170 nm. For the conical NWs with 200 nm base diameter, relatively little substrate is available for light reflection since the base of the NW nearly fills the unit cell. In this instance, a reflectance minimum is not observed, and the reflectance increases monotonically with the NW top diameter. Lengthening the NW contributes to a decrease in the reflectance since a taller NW has a smaller angle of escape for back-reflected light, increasing the likelihood of scattered light interactions with the sidewalls of the NW.

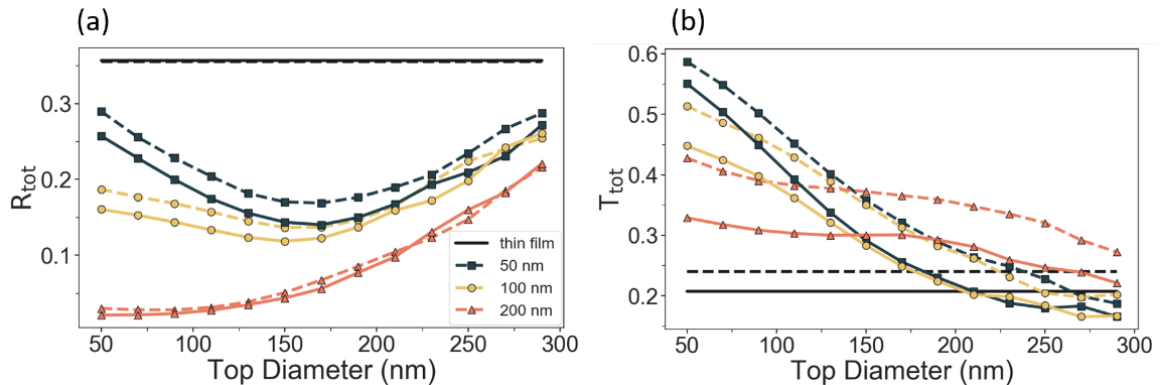


Figure 7.3. (a) The total reflectance and (b) total transmittance versus top diameter for each of the NW morphologies, as well as a thin film. The legend indicates the NW base diameter. Dashed lines represent NWs with length of 1000 nm and solid lines indicate those with length of 2000 nm.

Figure 7.3(b) shows that transmission through the NW array can be reduced by increasing the top diameter. For small top diameter, the lack of volume leads to large transmission. The ratio between the top and the bottom diameter of the NW also plays a role. A larger ratio means that a wider range of diameters is accessible along the length of the NW, which improves absorption at different wavelengths across the spectrum, according to the diameter dependence of the HE_{11} optical resonance. For comparison, Figure 7.3 also shows the transmission and reflection for 1000 nm and 2000 nm thin films without anti-reflection coatings.

The overall performance of NW arrays for solar energy conversion is determined by the absorptance, transmittance and reflectance. To quantify the expected photovoltaic performance of the various NW morphologies, the photocurrent density (J in units of

mA/cm²) generated by the AM1.5D simulated solar spectrum was calculated according to the following volume integral [7.9]:

$$J = \frac{e}{p^2} \int \frac{\epsilon_0}{\hbar} |E|^2 nk dV \quad (7.2)$$

where e is the fundamental charge, ϵ_0 is the permittivity of free space, P is the pitch of the square array, E is the electric field in the NW solved by COMSOL, and n and k are the real and complex components of the refractive index, respectively. As mentioned in the Methods section, the incident electric field is weighted by the AM1.5D simulated solar spectrum, so that $|E|^2$ in Eq. (7.2) accordingly contains the spectral dependence of the solar spectrum. The integrand has units of m⁻³s⁻¹ and represents the rate of photon absorption. The internal quantum efficiency is assumed to be unity; i.e., each photon produces one electron-hole pair that contributes to the photocurrent. The total photocurrent is the sum of the photocurrent over all wavelengths.

The total photocurrent for each NW morphology is shown in Figure 7.4 for two different lengths of 1000 nm (dashed lines) and 2000 nm (solid lines). For comparison with the NWs, the horizontal lines indicate the photocurrent from a GaAs thin film without any anti-reflection coating. The photocurrent improves slightly by increasing the NW length from 1000 to 2000 nm by reducing transmittance loss through the NW array, and likewise for the thin film. The optimum photocurrent (26.5 mAcm⁻²) corresponded to a conical NW morphology with base diameter of 200 nm, top diameter of 110 nm, and length of 2000 nm. For the inverted conical morphology with a base diameter of 50 or 100 nm, the optimum photocurrent was 25.0 and 25.6 mAcm⁻², respectively, with an optimum top

diameter of 210 nm. Figure 7.13 of the Supplementary Document shows the related electric field profiles. Previously reported optimized cylindrical NWs of 170 nm diameter also had photocurrents of 25.6 mAcm^{-2} [7.52], making the inverted cones on par with the cylindrical structures, while the cones demonstrated a slight improvement. However, the smaller base diameter of the inverted conical morphology would be advantageous to reduce misfit dislocations with a lattice-mismatched substrate such as silicon.

In comparison, the photocurrent for the thin film GaAs (without any anti-reflection coatings) was much lower than that from the NWs due to substantial reflectance loss. The maximum possible photocurrent from GaAs under the AM1.5D spectrum, ignoring any reflectance or transmittance loss, is 29 mAcm^{-2} . Thus, the optimum NW morphology achieves a photocurrent that approaches the best possible performance.

Kordrostrami et al. [7.36] showed that photocurrent improved by 13% for conical Si NWs but decreased by 5% for inverted conical NWs as compared to cylindrical NWs [7.36]. Ko et al. [7.31] compared cylindrical Si NWs to four different inverted conical geometries. They reported short circuit currents of 20.4 mAcm^{-2} and 27.5 mAcm^{-2} for the best inverted cone. Shalev et. al [7.42] showed absorption enhancements of 65% and 36.6% for inverted Si cones and cylinders, respectively, as compared to a thin film (and a 1.8% improvement of inverted cones over cylinders). Wang and Leu showed that Si conical NWs can absorb 74% of light in the solar spectrum compared to only 61% in cylindrical NWs [7.38]. With respect to GaAs NWs, Fountaine et. al. have also demonstrated that GaAs conical NWs improve absorption over cylindrical NWs showing an increase in photocurrent from 25.0 mAcm^{-2} to 29.5 mAcm^{-2} [7.57].

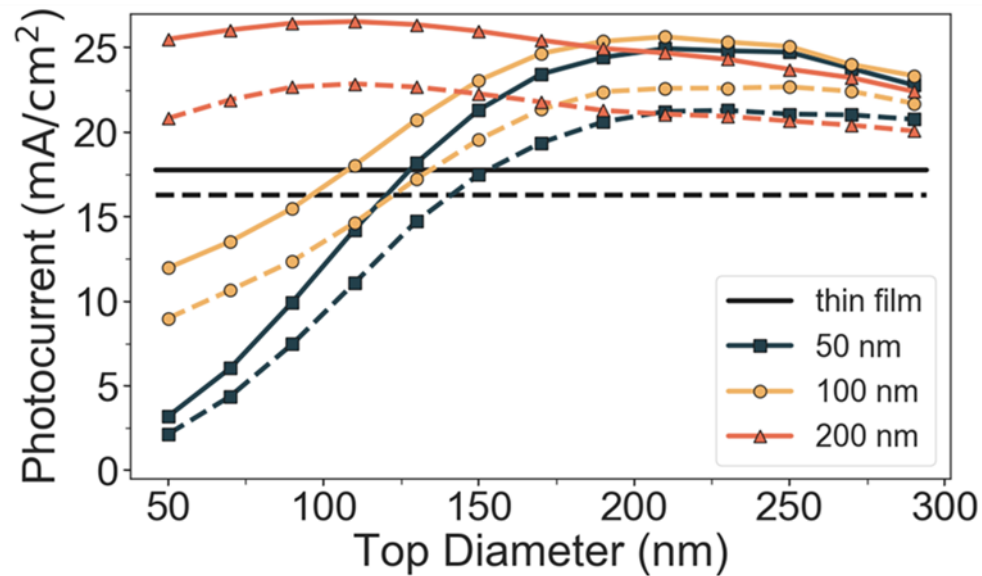


Figure 7.4. Photocurrent versus top diameter generated in each of the NW morphologies. The legend indicates the NW base diameter. Dashed lines represent NWs with length of 1000 nm and solid lines indicate those with length of 2000 nm.

The dependence of pitch has not been explored in this work, although pitch can play an important role in light scattering and absorption [7.58]. If the pitch is too small, neighboring NWs compete for absorption, and reflection from the top of the array increases. On the other hand, if the pitch is too large, the NW absorption decreases since the NW density is too sparse. The optimum ratio between the top diameter and the pitch is a topic for future studies. However, we do not expect substantial further improvement with pitch, since the optimum geometry discussed above already provides nearly the maximum theoretical current density.

7.5. Conclusions

Optical absorptance in conical and inverted conical NW arrays support multiple HE_{1n} modes that red-shift along the length of the NW as the diameter changes due to tapering. Conical NWs have superior anti-reflection properties compared to the inverted conical NWs by reducing reflectance loss from the substrate and NW top. Nevertheless, when both optical absorptance and reflectance are considered, the inverted conical NWs achieved only slightly less photocurrent than the conical NWs.

7.6. Supplementary Materials

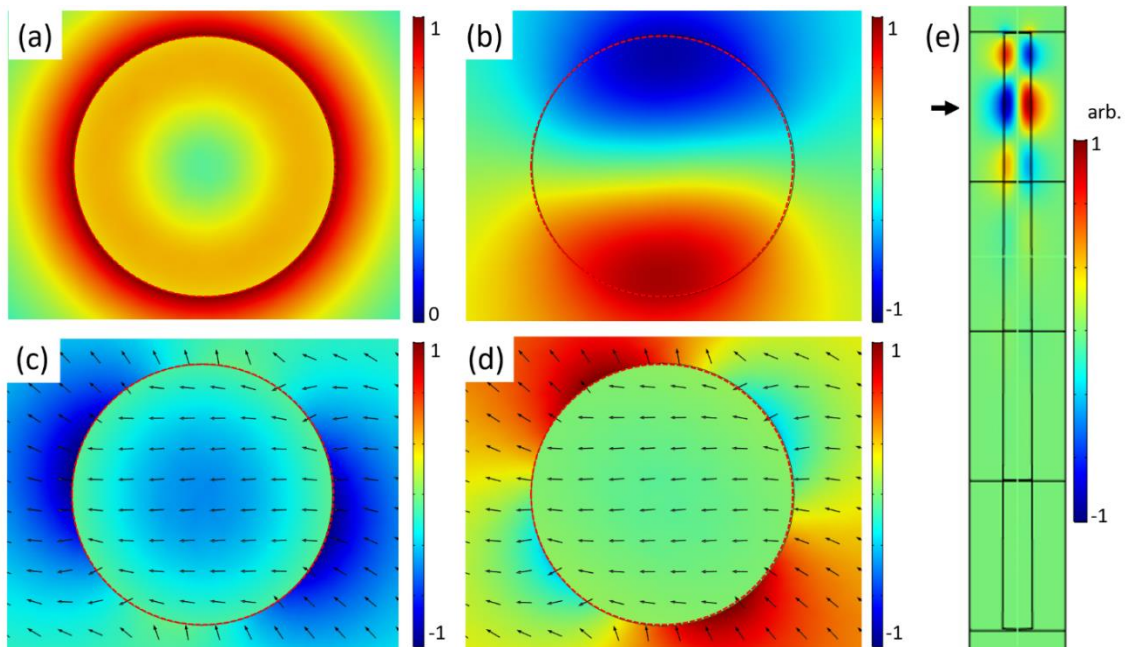


Figure 7.5. Electric field profiles for a nearly cylindrical nanowire with 90 nm top diameter, 100 nm base diameter, and 2000 nm length. The exciting wavelength is 525 nm. The norm of the electric field is shown in (a) for a planar slice at a depth of 250 nm from the top of the nanowire as indicated by the arrow in (e). Subplots (b) and (e) show the E_z component of the electric field while (c) and (d) show E_x and E_y , respectively. The arrow plots show the direction of the field in the plane. The red dotted circle represents the edge of the nanowire at the given depth.

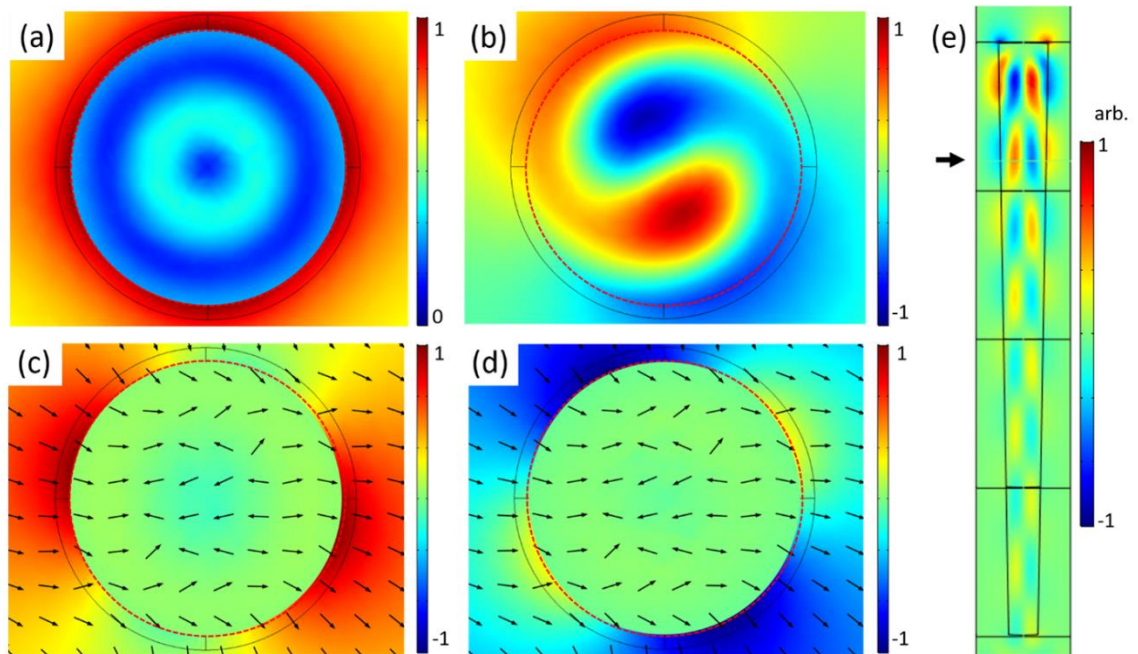


Figure 7.6. Electric field profiles for a nearly cylindrical nanowire with 170 nm top diameter, 100 nm base diameter, and 2000 nm length. The exciting wavelength is 455 nm. The norm of the electric field is shown in (a) for a planar slice at a depth of 400 nm from the top of the nanowire as indicated by the arrow in (e). Subplots (b) and (e) show the E_z component of the electric field while (c) and (d) show E_x and E_y respectively. The arrow plots show the direction of the field in the plane. The red dotted circle represents the edge of the nanowire at the given depth.

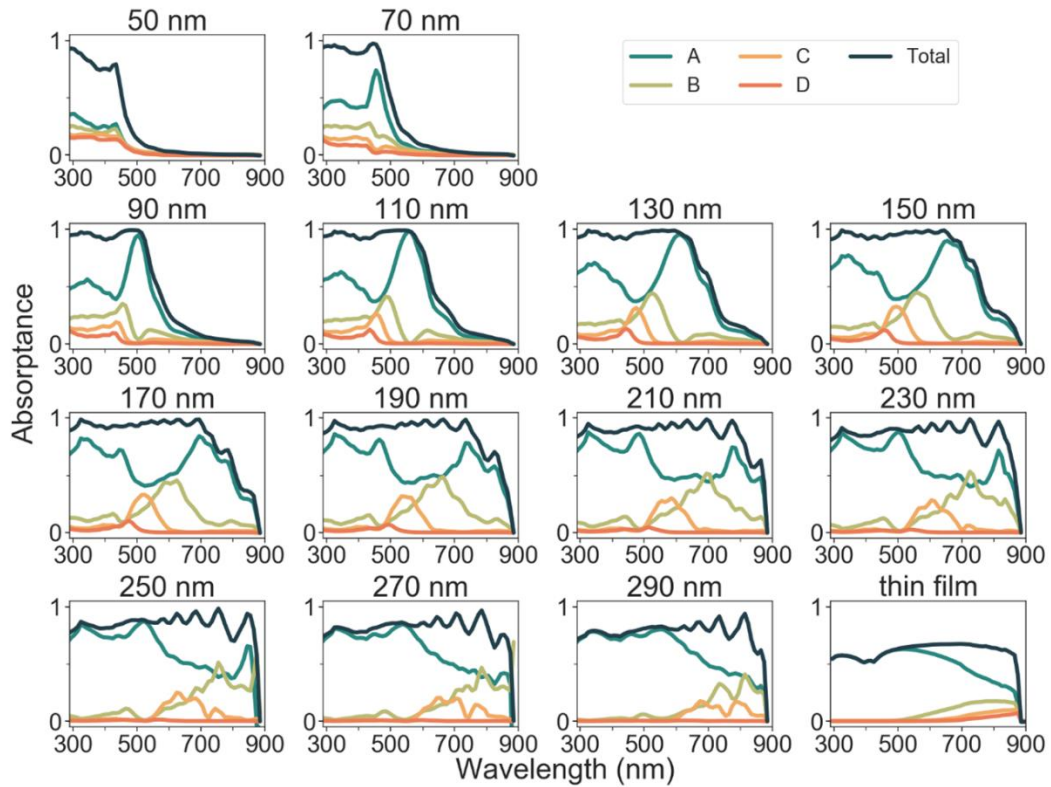


Figure 7.7. Absorbance spectra for NWs with a base diameter of 50 nm and a length of 2000 nm. The NW top diameter is given above each plot. The spectra have been subdivided into the contributions to absorbance from incremental segments of 500 nm length where A is the top 500 nm and D is the bottom 500 nm. The absorbance spectrum of a thin film is also shown.

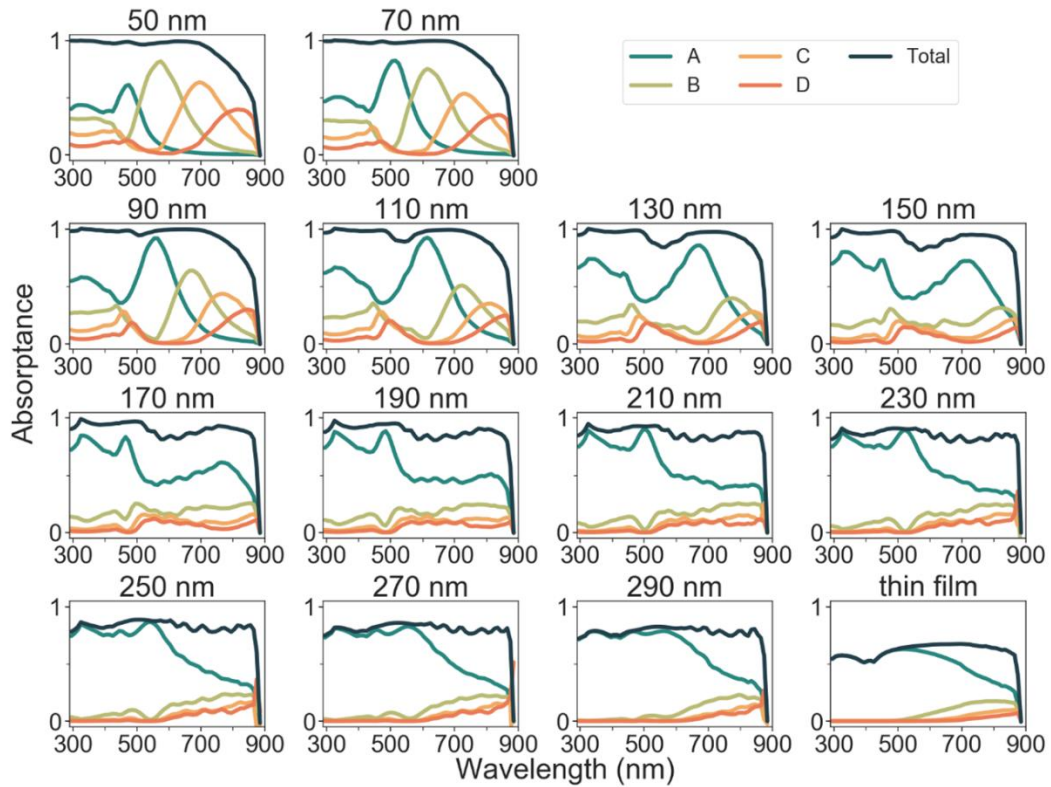


Figure 7.8. Absorbance spectra for NWs with a base diameter of 200 nm and a length of 2000 nm. The NW top diameter is given above each plot. The spectra have been subdivided into the contributions to absorbance from incremental segments of 500 nm length where A is the top 500 nm and D is the bottom 500 nm. The absorbance spectrum of a thin film is also shown.

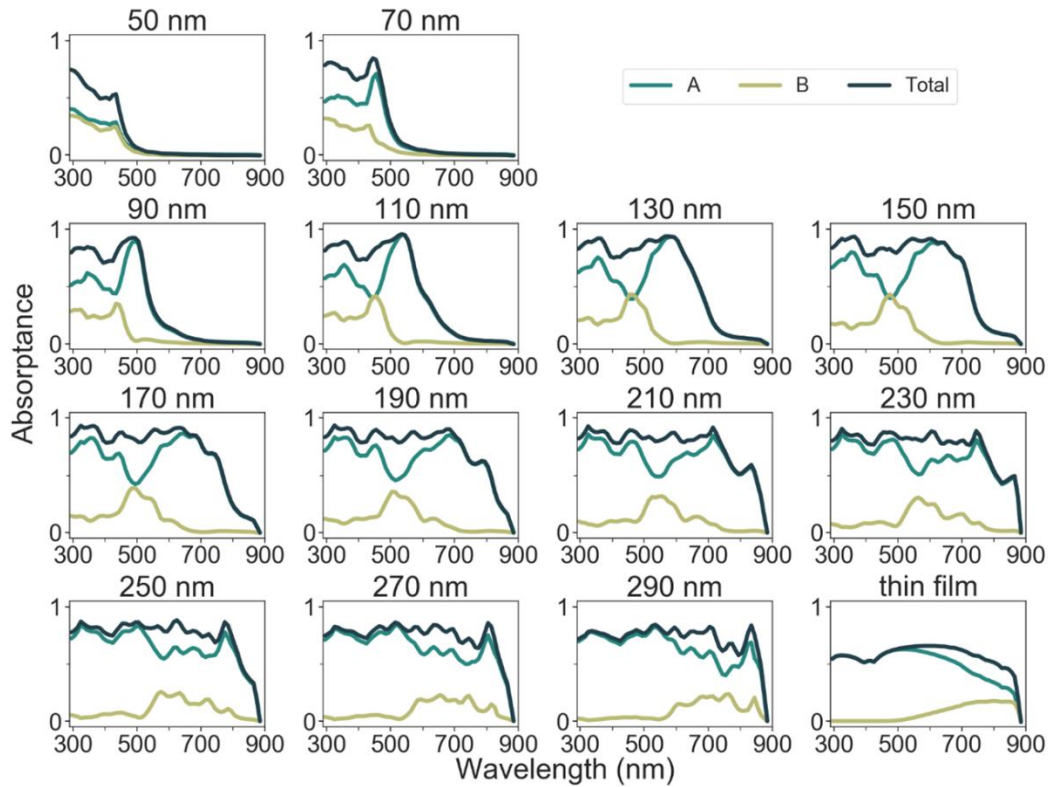


Figure 7.9. Absorbance spectra for NWs with a base diameter of 50 nm and a length of 1000 nm. The NW top diameter is given above each plot. The spectra have been subdivided into the contributions to absorbance from incremental segments of 500 nm length where A is the top 500 nm and B is the bottom 500 nm. The absorbance spectrum of a thin film is also shown.

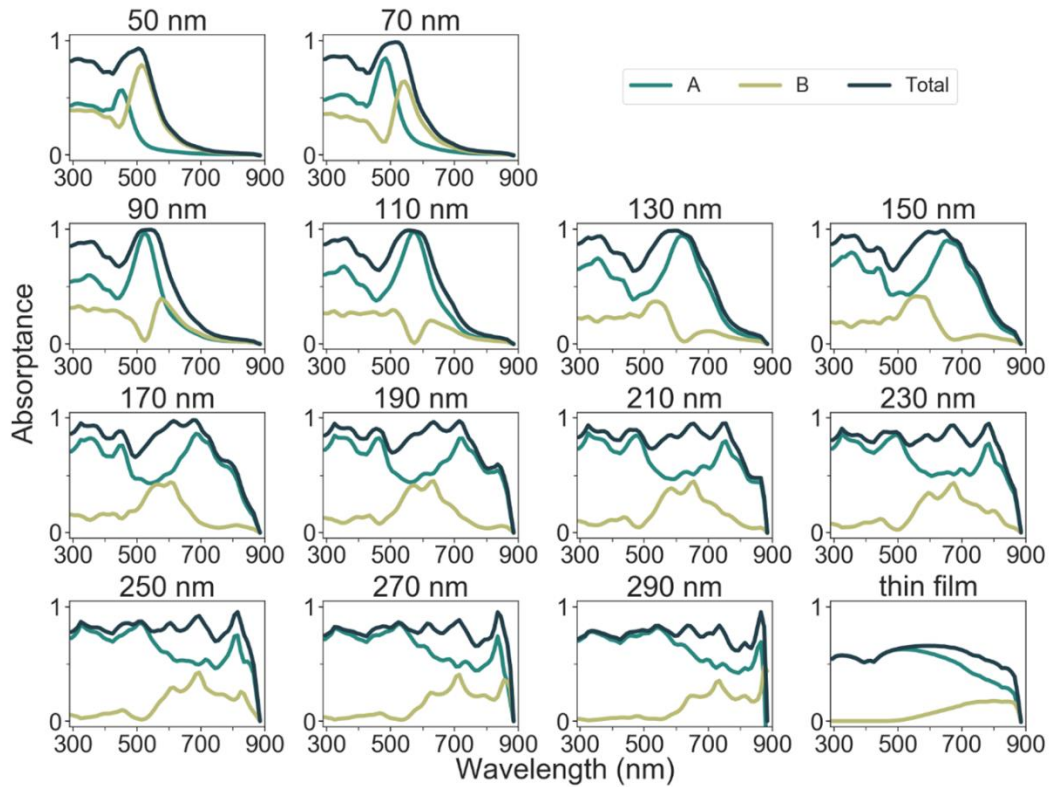


Figure 7.10. Absorbance spectra for NWs with a base diameter of 100 nm and a length of 1000 nm. The NW top diameter is given above each plot. The spectra have been subdivided into the contributions to absorbance from incremental segments of 500 nm length where A is the top 500 nm and B is the bottom 500 nm. The absorbance spectrum of a thin film is also shown.

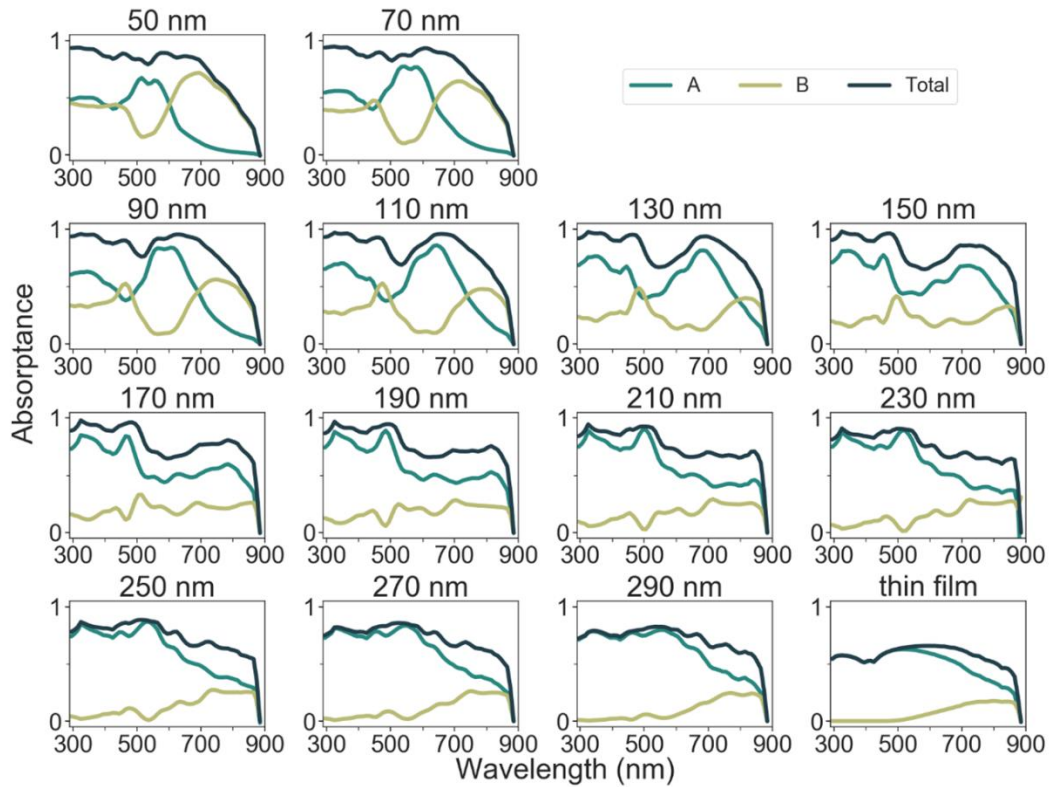


Figure 7.11. Absorbance spectra for NWs with a base diameter of 200 nm and a length of 1000 nm. The NW top diameter is given above each plot. The spectra have been subdivided into the contributions to absorbance from incremental segments of 500 nm length where A is the top 500 nm and B is the bottom 500 nm. The absorbance spectrum of a thin film is also shown.

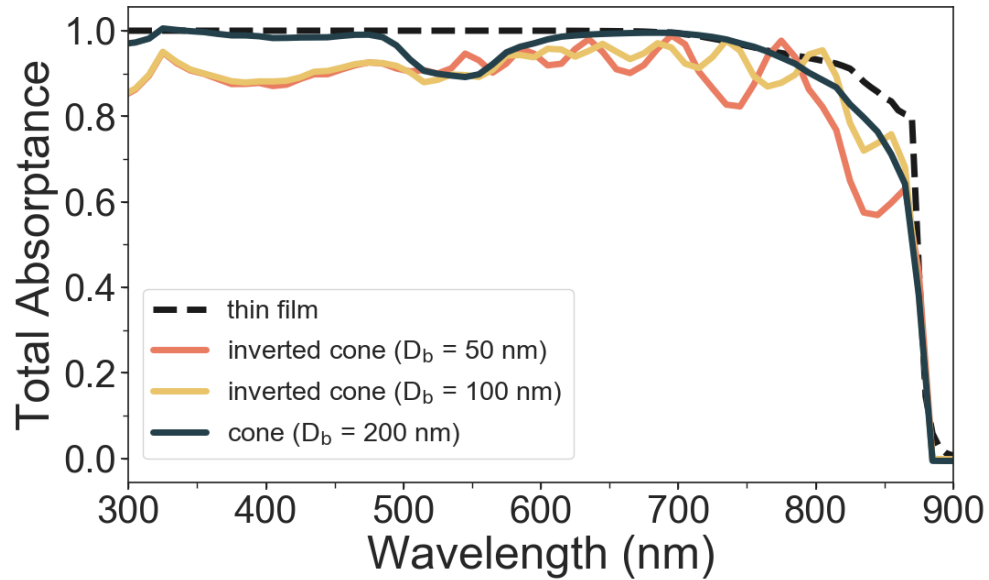


Figure 7.12. Absorptance for inverted cone NWs (base diameter of 50 nm and 100 nm, and top diameter of 210 nm), a cone NW (base diameter of 200 nm and a top diameter of 110 nm), and a 2000 nm thick film (according to the Beer-Lambert model and assuming perfect anti-reflection coating).

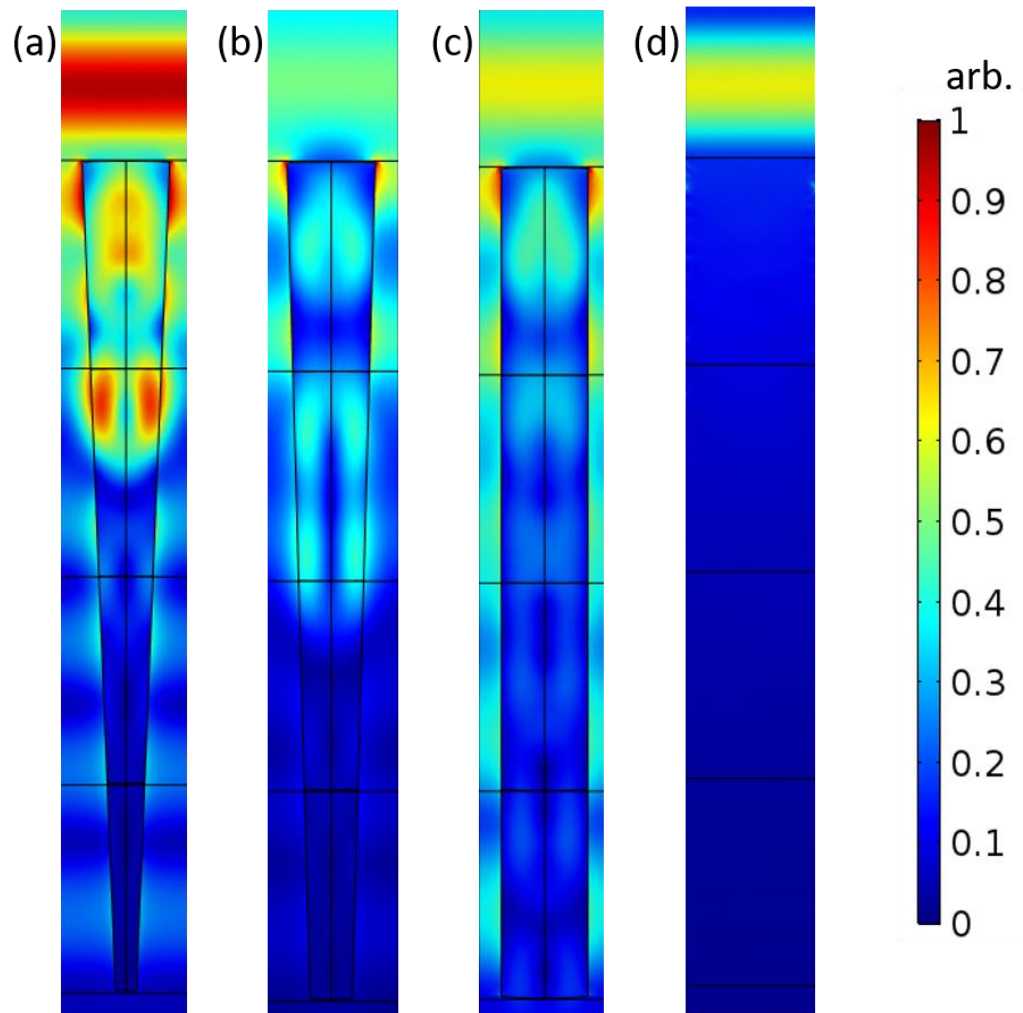


Figure 7.13. The electric field norm at 735 nm for (a) a NW with 210 nm top diameter and 50 nm base diameter, (b) a NW with 210 nm top diameter and 100 nm base diameter, (c) a cylindrical NW of 210 nm diameter, (d) a thin film. In (d) the reflectance is very large resulting in a small field inside the film. No modes are excited in (d). In (a), (b), and (c), various HE_{1n} modes are excited. The fields within the NW change as the diameter changes, concentrating in different locations. The absorptance in the NWs in (a), (b), and (c) are 0.83, 0.98, and 0.81 while the reflectance is 0.14, 0.02, and 0.06, respectively. The thickness is 2000 nm in all cases.

7.7. References

- [7.1] Y. Zhang, J. Wu, M. Aagesen, and H. Liu, “III–V nanowires and nanowire optoelectronic devices,” *J. Phys. D. Appl. Phys.*, vol. 48, no. 46, 2015, Art. no. 463001.
- [7.2] N. I. Goktas, P. Wilson, A. Ghukasyan, D. Wagner, S. McNamee, and R. LaPierre, “Nanowires for energy: A review,” *Appl. Phys. Rev.*, vol. 5, no. 4, 2018, Art. no. 041305.
- [7.3] R. R. LaPierre, M. Robson, K. M. Azizur-Rahman, and P. Kuyanov, “A review of III-V nanowire infrared photodetectors and sensors,” *J. Phys. D. Appl. Phys.*, vol. 50, no. 12, 2017, Art. no. 123001.
- [7.4] R. R. LaPierre et al., “III-V nanowire photovoltaics: Review of design for high efficiency,” *Phys. Status Solidi - Rapid Res. Lett.*, vol. 7, no. 10, pp. 815–830, 2013.
- [7.5] H. Guo, L. Wen, X. Li, Z. Zhao, and Y. Wang, “Analysis of optical absorption in GaAs nanowire arrays,” *Nanoscale Res. Lett.*, vol. 6, 2011, Art. no. 617.
- [7.6] L. Wen, Z. Zhao, X. Li, Y. Shen, H. Guo, and Y. Wang, “Theoretical analysis and modeling of light trapping in high efficiency GaAs nanowire array solar cells,” *Appl. Phys. Lett.*, vol. 99, no. 14, 2011, Art. no. 143116.
- [7.7] Y. Hu, R. R. LaPierre, M. Li, K. Chen, and J. J. He, “Optical characteristics of GaAs nanowire solar cells,” *J. Appl. Phys.*, vol. 112, no. 10, 2012, Art. no. 104311.

- [7.8] K. W. Robertson, R. R. LaPierre, and J. J. Krich, “Efficient wave optics modeling of nanowire solar cells using rigorous coupled-wave analysis,” *Opt. Express*, vol. 27, no. 4, pp. A133–A147, 2019.
- [7.9] A. H. Trojnar, C. E. Valdivia, R. R. LaPierre, K. Hinzer, and J. J. Krich, “Optimizations of GaAs Nanowire Solar Cells,” *IEEE J. Photovoltaics*, vol. 6, no. 6, pp. 1494–1501, 2016.
- [7.10] N. Anttu et al., “Absorption of light in InP nanowire arrays,” *Nano Res.*, vol. 7, no. 6, pp. 816–823, 2014.
- [7.11] P. Kailuweit, M. Peters, J. Leene, K. Mergenthaler, F. Dimroth, and A. W. Bett, “Numerical simulations of absorption properties of InP nanowires for solar cell applications,” *Prog. Photovoltaics Res. Appl.*, vol. 20, no. 8, pp. 945–953, 2012.
- [7.12] J. Kupec, R. L. Stoop, and B. Witzigmann, “Light absorption and emission in nanowire array solar cells,” *Opt. Express*, vol. 18, no. 26, pp. 27589–27605, 2010.
- [7.13] N. Anttu and H. Q. Xu, “Coupling of light into nanowire arrays and subsequent absorption,” *J. Nanosci. Nanotechnol.*, vol. 10, no. 11, pp. 7183–7187, 2010.
- [7.14] K. Zhang and D. Li, *Electromagnetic Theory for Microwaves and Optoelectronics*. Springer, 2008.
- [7.15] A. W. Snyder and J. D. Love, *Optical Waveguide Theory*. New York: Chapman and Hall, 1983.
- [7.16] B. Wang and P. W. Leu, “Tunable and selective resonant absorption in vertical nanowires,” *Opt. Lett.*, vol. 37, no. 18, pp. 3756–3758, 2012.

- [7.17] K. T. Fountaine, W. S. Whitney, and H. A. Atwater, “Resonant absorption in semiconductor nanowires and nanowire arrays: Relating leaky waveguide modes to Bloch photonic crystal modes,” *J. Appl. Phys.*, vol. 116, no. 15, 2014, Art. no. 153106.
- [7.18] V. Dagtė and N. Anttu, “Modal analysis of resonant and non-resonant optical response in semiconductor nanowire arrays,” *Nanotechnology*, vol. 30, no. 2, 2019, Art. no. 025710.
- [7.19] S. Mokkalpati, D. Saxena, H. H. Tan, and C. Jagadish, “Optical design of nanowire absorbers for wavelength selective photodetectors,” *Sci. Rep.*, vol. 5, 2015, Art. no. 15339.
- [7.20] K. M. Azizur-Rahman and R. R. LaPierre, “Wavelength-selective absorptance in GaAs, InP and InAs nanowire arrays,” *Nanotechnology*, vol. 26, no. 29, 2015, Art. no. 295202.
- [7.21] S. Mokkalpati and C. Jagadish, “Review on photonic properties of nanowires for photovoltaics,” *Opt. Express*, vol. 24, no. 15, pp. 17345–17358, 2016.
- [7.22] R. Ren, Y.-X. Guo, and R.-H. Zhu, “Enhanced absorption in elliptical silicon nanowire arrays for solar energy harvesting,” *Opt. Eng.*, vol. 53, no. 2, 2014, Art. no. 027102.
- [7.23] L. Cao et al., “Semiconductor nanowire optical antenna solar absorbers,” *Nano Lett.*, vol. 10, no. 2, pp. 439–445, 2010.

- [7.24] Y. Yu and L. Cao, “Leaky mode engineering: A general design principle for dielectric optical antenna solar absorbers,” *Opt. Commun.*, vol. 314, pp. 79–85, 2014.
- [7.25] Y. Zeng, Q. Ye, and W. Shen, “Design principles for single standing nanowire solar cells: Going beyond the planar efficiency limits,” *Sci. Rep.*, vol. 4, 2014, Art. no. 4915.
- [7.26] B. C. P. Sturmberg et al., “Nanowire array photovoltaics: Radial disorder versus design for optimal efficiency,” *Appl. Phys. Lett.*, vol. 101, no. 17, 2012, Art. no. 173902.
- [7.27] K. T. Fountaine, W. H. Cheng, C. R. Bukowsky, and H. A. Atwater, “Near-unity unselective absorption in sparse InP nanowire arrays,” *ACS Photonics*, vol. 3, no. 10, pp. 1826–1832, 2016.
- [7.28] X. Yan, L. Gong, L. Ai, W. Wei, X. Zhang, and X. Ren, “Enhanced photovoltaic performance of nanowire array solar cells with multiple diameters,” *Opt. Express*, vol. 26, no. 26, pp. A974–A983, 2018.
- [7.29] G. J. Lee et al., “Selective and sensitive photon sieve based on III–V semiconductor nanowire forest fabricated by lithography-free process,” *Adv. Opt. Mater.*, vol. 8, no. 17, 2020, Art. no. 2000198.
- [7.30] F. Adibzadeh and S. Olyaei, “Optical absorption enhancement in vertical InP nanowire random structures for photovoltaic applications,” *Opt. Quantum Electron.*, vol. 52, 2020, Art. no. 6.

- [7.31] M. Ko, S. H. Baek, B. Song, J. W. Kang, S. A. Kim, and C. H. Cho, “Periodically diameter-modulated semiconductor nanowires for enhanced optical absorption,” *Adv. Mater.*, vol. 28, no. 13, pp. 2504–2510, 2016.
- [7.32] S. Kim and J. F. Cahoon, “Geometric nanophotonics: Light management in single nanowires through morphology,” *Acc. Chem. Res.*, vol. 52, pp. 3511–3520, 2019.
- [7.33] Y. Zhan, X. Li, S. Wu, K. Li, Z. Yang, and A. Shang, “Enhanced photoabsorption in front-tapered single-nanowire solar cells,” *Opt. Lett.*, vol. 39, no. 19, pp. 5756–5759, 2014.
- [7.34] B. Wang, E. Stevens, and P. W. Leu, “Strong broadband absorption in GaAs nanocone and nanowire arrays for solar cells,” *Opt. Express*, vol. 22, no. S2, pp. A386–A395, 2014.
- [7.35] Y. Li, P. Gao, Q. Chen, J. Yang, J. Li, and D. He, “Nanostructured semiconductor solar absorbers with near 100% absorption and related light management picture,” *J. Phys. D. Appl. Phys.*, vol. 49, no. 21, 2016, Art. no. 215104.
- [7.36] Z. Kordrostami and A. Yadollahi, “High absorption enhancement of invert funnel and conical nanowire solar cells with forward scattering,” *Opt. Commun.*, vol. 459, 2020, Art. no. 125059.
- [7.37] S. Jeong, M. D. McGehee, and Y. Cui, “All-back-contact ultra-thin silicon nanocone solar cells with 13.7% power conversion efficiency,” *Nat. Commun.*, vol. 4, 2013, Art. no. 3950.
- [7.38] B. Wang and P. W. Leu, “Enhanced absorption in silicon nanocone arrays for photovoltaics,” *Nanotechnology*, vol. 23, no. 19, 2012, Art. no. 194003.

- [7.39] S. L. Diedenhofen, O. T. A. Janssen, G. Grzela, E. P. A. M. Bakkers, and J. Gómez Rivas, “Strong geometrical dependence of the absorption of light in arrays of semiconductor nanowires,” *ACS Nano*, vol. 5, no. 3, pp. 2316–2323, 2011.
- [7.40] S. J. Gibson et al., “Tapered InP nanowire arrays for efficient broadband high-speed single-photon detection,” *Nat. Nanotechnol.*, vol. 14, no. 5, pp. 473–479, 2019.
- [7.41] G. Y. Abdel-Latif, M. F. O. Hameed, M. Hussein, M. A. Razzak, and S. S. A. Obayya, “Electrical characteristics of funnel-shaped silicon nanowire solar cells,” *J. Photonics Energy*, vol. 7, no. 4, 2017, Art. no. 047501.
- [7.42] G. Shalev, S. W. Schmitt, H. Embrechts, G. Brönstrup, and S. Christiansen, “Enhanced photovoltaics inspired by the fovea centralis,” *Sci. Rep.*, vol. 5, 2015, Art. no. 8570.
- [7.43] A. Prajapati, Y. Nissan, T. Gabay, and G. Shalev, “Light trapping with silicon light funnel arrays,” *Materials*, vol. 11, no. 3, 2018, Art. no. 445.
- [7.44] A. Prajapati, Y. Nissan, T. Gabay, and G. Shalev, “Broadband absorption of the solar radiation with surface arrays of subwavelength light funnels,” *Nano Energy*, vol. 54, pp. 447–452, 2018.
- [7.45] M. D. Ko, T. Rim, K. Kim, M. Meyyappan, and C. K. Baek, “High efficiency silicon solar cell based on asymmetric nanowire,” *Sci. Rep.*, vol. 5, pp. 1–8, 2015.
- [7.46] L. Li et al., “Broadband optical absorption enhancement in silicon nanofunnel arrays for photovoltaic applications,” *Appl. Phys. Lett.*, vol. 100, no. 22, 2012, Art. no. 223902.

- [7.47] G. Marko, A. Prajapati, and G. Shalev, “Subwavelength nonimaging light concentrators for the harvesting of the solar radiation,” *Nano Energy*, vol. 61, pp. 275–283, 2019.
- [7.48] A. M. Labin, S. K. Safuri, E. N. Ribak, and I. Perlman, “Müller cells separate between wavelengths to improve day vision with minimal effect upon night vision,” *Nat. Commun.*, vol. 5, 2014, Art. no. 5319.
- [7.49] P. C. McIntyre and A. Fontcuberta i Morral, “Semiconductor nanowires: to grow or not to grow?,” *Mater. Today Nano*, vol. 9, 2020, Art. no. 100058.
- [7.50] N. Dhindsa, A. Chia, J. Boulanger, I. Khodadad, R. LaPierre, and S. S. Saini, “Highly ordered vertical GaAs nanowire arrays with dry etching and their optical properties,” *Nanotechnology*, vol. 25, no. 30, 2014, Art. no. 305303.
- [7.51] A. C. E. Chia et al., “Electrical transport and optical model of GaAs-AlInP core-shell nanowires,” *J. Appl. Phys.*, vol. 111, no. 9, 2012, Art. no. 094319.
- [7.52] D. P. Wilson, A. S. Sokolovskii, N. I. Goktas, V. G. Dubrovskii, and R. R. LaPierre, “Photovoltaic light funnels grown by GaAs nanowire droplet dynamics,” *IEEE J. Photovoltaics*, vol. 9, no. 5, pp. 1225–1231, 2019.
- [7.53] N. Anttu, H. Mäntynen, T. Sadi, A. Matikainen, J. Turunen, and H. Lipsanen, “Comparison of absorption simulation in semiconductor nanowire and nanocone arrays with the Fourier modal method, the finite element method, and the finite-difference time-domain method,” *Nano Express*, vol. 1, no. 3, 2020, Art. no. 030034.

- [7.54] National Renewable Energy Laboratory (NREL), “Reference Air Mass 1.5 Spectra.” [Online]. Available: <https://www.nrel.gov/grid/solar-resource/spectra-am1.5.html>. [Accessed: 01-Jan-2021].
- [7.55] E. D. Palik, Handbook of Optical Constants of Solids. Washington: Academic Press Inc., 1985.
- [7.56] G. E. Cirlin et al., “Critical diameters and temperature domains for MBE growth of III-V nanowires on lattice mismatched substrates,” *Phys. Status Solidi - Rapid Res. Lett.*, vol. 3, no. 4, pp. 112–114, 2009.
- [7.57] K. T. Fountaine, C. G. Kendall, and H. A. Atwater, “Near-unity broadband absorption designs for semiconducting nanowire arrays via localized radial mode excitation,” *Opt. Express*, vol. 22, no. S3, pp. A930-A940, 2014.
- [7.58] N. Anttu, “Absorption of light in a single vertical nanowire and a nanowire array,” *Nanotechnology*, vol. 30, no. 10, 2019, Art. no. 104004.

8. Corrugated Nanowires for Distributed Bragg Reflectors

8.1. Summary

This chapter presents unpublished work on corrugated nanowire (NW) distributed Bragg reflectors (DBRs). NW DBRs are an emerging technology with many potential applications. This chapter presents simulations of corrugated NW arrays to explore and control the reflectance generated by these structures. It is shown that introducing even a small periodic change (5 nm corrugation depth) in the NW diameter produces a significant change in the reflectance compared to cylindrical NWs. The reflectance peaks are tunable by altering the effective refractive index (through changes to the diameter and the pitch) and the periodicity of the corrugated oscillations. The reflectance peaks are caused by interference between forward and backward propagating modes travelling in the NW. However, the field patterns within the corrugated NWs are more complicated than a classical Bragg grating. It is suspected that multiple effects take place in NW arrays including coupling to forward and backward modes within the NW, nearest-neighbour coupling, and coupling to radiation modes. Additionally, the amount of reflectance is dependent on the amount of light which interacts with each individual NW, which will depend on the density of the array and the power loss due to the leaky modes of the NW.

8.2. Introduction

Distributed Bragg reflectors (DBRs) are a grating composed of alternating layers of material with different refractive index, each of quarter wave thickness [8.1]. The grating

reflects incident light over a bandwidth $\Delta\lambda$ centered at the Bragg wavelength, λ_B , defined by [8.1]:

$$\lambda_B = \frac{2n_{eff}\Lambda}{m} \quad (8.1)$$

where n_{eff} is the effective refractive index of the grating and Λ is the grating period. DBRs are used in a wide range of applications, such as optical feedback in single mode semiconductor lasers and fiber-Bragg-grating filters and sensors [8.1]. Recently, there is increasing interest to implement DBRs into nanoscale laser [8.2-8.4], photovoltaic [8.5], and photonic bandgap applications [8.6].

NWs are known for their unique optical and electrical properties with applications in photovoltaics, photodetectors, lasers and LEDs [8.7-8.9]. Their unique optical properties arise from their waveguiding properties due to HE_{1n} leaky mode resonances [8.10]. NWs are grown using a liquid metal droplet as seed particle at the top of the NWs in the vapor-liquid-solid (VLS) growth process [8.11].

Like their thin film counterparts, NW devices can benefit from DBRs implemented along the NW axis [8.2-8.6]. However, the heterostructure formation required for DBRs can be difficult to implement in NWs due to material diffusion, the “reservoir effect” of the droplet seed particle [8.12, 8.13], NW kinking [8.14, 8.15], and other instabilities inherent to the nanoscale growth process. Fortunately, the unique geometry of NWs enables an alternative method of implementing DBRs. Rather than creating a grating as a periodic heterostructure, it is possible to implement a grating by periodically altering the diameter of the NW along its axis, producing a “corrugated” waveguide grating.

In the VLS growth process, the diameter of NWs is directly related to the diameter of the droplet seed particle on the top of the NWs [8.11]. For the often-used gold-seeded NW growth, the volume of Au remains largely unchanged throughout the growth process, resulting in a NW with constant diameter along its length. However, group III-V semiconductor NWs can also be grown by the self-assisted method where the droplet seed particle is an element of the NW itself (e.g., a Ga droplet for GaAs NWs) [8.11]. In this case, the diameter of the NWs can be controlled throughout the NW growth process by altering the flux of the group III and V material (while keeping the NW composition constant) [8.16]. For example, Ga-assisted growth of GaAs NWs allows control of the NW diameter via the V/III (As/Ga) atomic flux ratio. A high V/III flux ratio provides a decreasing Ga flux that shrinks the Ga droplet at the top of the NW and narrows the NW diameter. Conversely, a low V/III flux ratio provides an increasing Ga flux that expands the Ga droplet and widens the NW diameter. This principle can be extended to the self-assisted VLS growth of other III-V materials to control the NW diameter. Detailed theoretical studies have shown that the droplet diameter depends on the overall droplet volume, and whether the NWs form a widening or narrowing facet depends on the contact angle of the droplet [8.17].

Control of NW diameter has been used to make ultrathin NWs [8.18] and tapered NWs [8.16]. More complex NW structures, such as corrugated NWs, have not been extensively demonstrated despite a wide range of applications. Periodic diameter oscillations in Si and Ge whiskers were observed in very early studies of NWs and attributed to surface energy effects [8.19]. In Ref. [8.20], Au-catalyzed Si NWs were grown

where the Au was controllably diffused from the droplet onto the sidewalls of the NW by pressure changes which could resist a wet etchant. In a similar manner, dopants can be added periodically to the NW during growth, which slows the rate of post-growth etching [8.21]. Alternatively, NW diameter oscillations can be formed by twinning superlattices [8.22]. In these structures, periodic zinc-blende twinning, accompanied by NW sidewall micro-faceting, forms due to a droplet seed particle instability in the presence of high dopant concentrations.

Fabry-Perot cavities have been used to produce NW lasers although these are usually rectangular or cylindrical NWs without additional corrugations [8.23, 8.24]. Several studies have been done on the optical behavior of periodically corrugated structures in rectangular waveguides and fibers [8.25], but relatively few have been done on NWs. Vertically standing corrugated NW arrays therefore represent a new class of optical device that could have many applications.

8.3. Methods

A NW array was simulated in COMSOL Multiphysics 5.3a using the RF module. The unit cell consisted of an axially symmetric NW oriented along the z direction. Periodic boundary conditions were implemented in the x and y directions to simulate an infinite square array of NWs of period or pitch, P . A port boundary was placed above the vertically standing NW that generated linearly polarized incoming light. Simulations were performed for incoming wavelengths, λ , between 700 nm and 1100 nm. Perfectly matched layers (PMLs) were placed directly below the NW and above the port boundary to absorb all

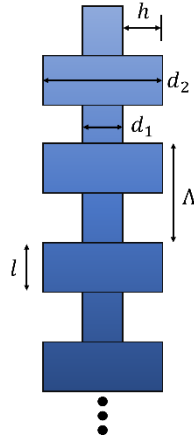


Figure 8.1. Geometry of the corrugated NWs.

transmitted and reflected light. Placing a PML directly below the NW terminates the domain without reflection from that boundary.

The NW material was GaAs, widely applicable in optoelectronic devices. The material was defined by specifying the complex refractive index [8.26]. To examine the reflecting behavior of the Bragg structure near the bandgap, without parasitic absorption in the GaAs, the imaginary part of the complex refractive index was set to zero unless otherwise indicated.

The corrugated NW geometry is shown in Figure 8.1. The NW had circular cross-section with diameter changing stepwise between d_1 and d_2 . The corrugation depth is defined as the difference in the minimum and maximum radii, $h = \frac{1}{2}(d_2 - d_1)$. The period of the diameter variations along the length of the NW was fixed at $\Lambda = 400$ nm, unless otherwise specified. The DBR period was repeated 10 times for a total NW length of 4000

nm, unless otherwise indicated. The axial length of both the narrow inner (d_1) and wide outer (d_2) diameter segments were equal with length $l = \Lambda/2$.

The narrow inner diameter was held constant at $d_1 = 165$ nm, while the wide outer diameter d_2 was varied. Based on our simulations, a NW array with a constant diameter of $d_1 = 165$ nm and pitch of $P = 1600$ nm produces an HE_{11} mode centered at approximately $\lambda = 890$ nm, close to the band gap of GaAs. The influence of P and d_2 on the reflectance and transmittance spectra was examined. Reflectance and transmittance were calculated by integrating the Poynting vector in planes above and below the simulated space.

8.4. Results and Discussion

Reflections are generated by altering the diameter of the NW periodically. Scattering events produce backward travelling waves. When the incoming and reflected waves meet the Bragg condition, given by Equation 8.1, they are said to be in synchronism [8.27]:

$$\frac{2\pi}{\Lambda} = \beta_1 + \beta_2 \quad (8.2)$$

where β_1 and β_2 are the propagation constants of the forward and backward travelling waves.

A NW array consisting of corrugated NWs is a much more complex problem than the quarter-wave stack of thin films. NW arrays consist of the localized HE_{1n} modes in the fiber core as well as the Bloch modes of the array due to near-field coupling of the NWs.

Backward and forward travelling modes can also couple to radiation modes leading to loss from the core. Although mathematically complex, some generalities can still be observed.

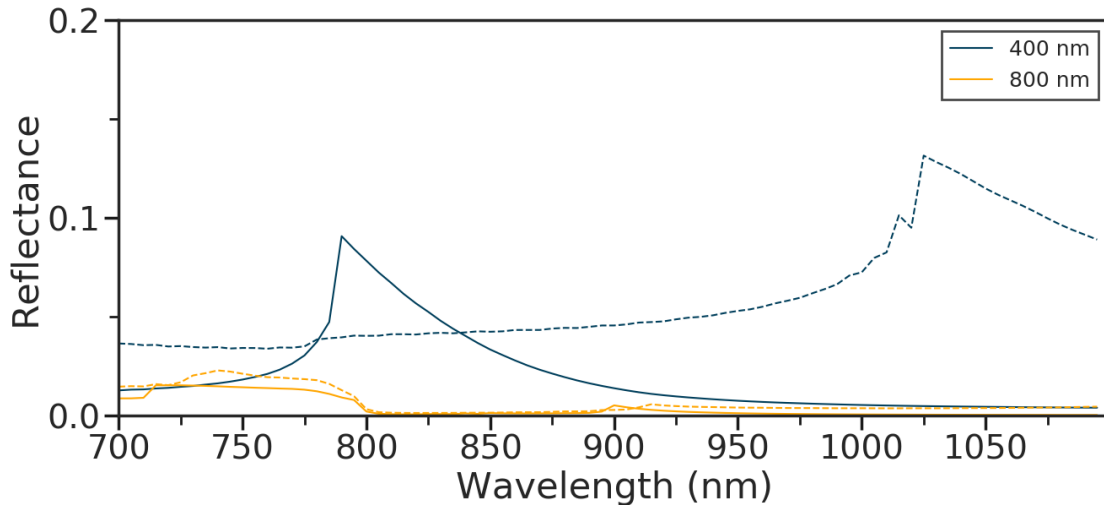


Figure 8.2. Reflectance from arrays of cylindrical NWs with pitches of 400 nm and 800 nm and diameter of 165 nm (solid lines) or 245 nm (dashed lines.)

Firstly, even a slight corrugation produces a significant change in reflectance compared to an array of NWs with vertical sidewalls. Figure 8.2 shows the reflectance from arrays of cylindrical NWs with pitches of 800 nm or 400 nm and constant diameter of either 165 nm or 245 nm (compare with Figure 8.3 which shows corrugated NW arrays). Reflectance from the straight NWs is relatively low for both diameters. The reflectance becomes more noticeable for the denser NW array. The anti-reflective properties of NW arrays are well-known, as discussed previously in this thesis in the context of PV devices.

Figure 8.3 shows that with increasing corrugation depth there is an increase in the overall reflection from the corrugated NWs. The field profiles in shows this effect, where the strength of the electric field is reduced more quickly in the NWs with larger corrugation depths than in the ones with smaller corrugation depths where the field extends deeper into the NW.

Figure 8.5 shows the effect of the number of DBR segments. Reflectance for a shallower grating depth is reduced as the number of DBR segments decreases. The reflectance for the deepest grating depths can still reach close to 1 even for a lower number of DBR segments, although the stopband becomes less sharp and the number of sidelobes decreases. Decreasing the number of periods of oscillation serves to reduce the reflectance due the decrease in the number of scattering events as the number of DBR segments decreases.

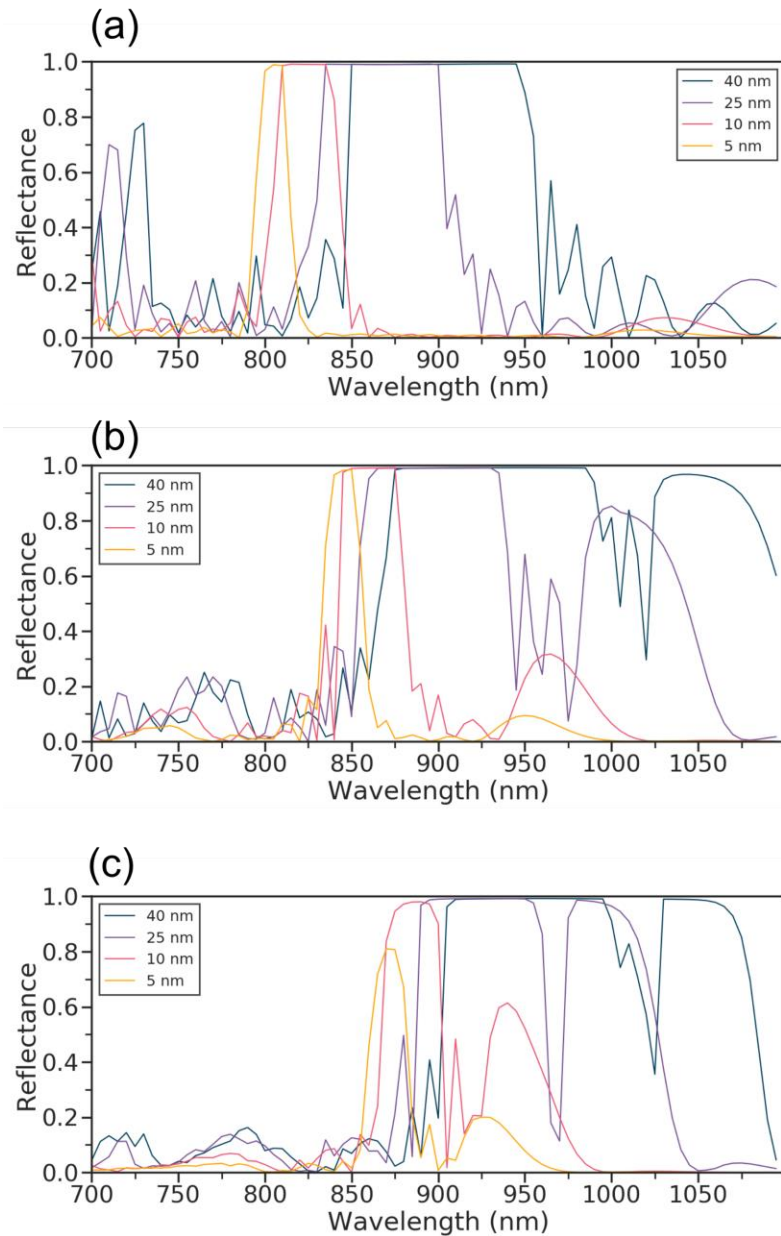


Figure 8.3. Reflectance for corrugated NW DBRs with an inner diameter of 165 nm and corrugation depths of 5 nm, 10 nm, 25 nm and 40 nm. The period, Λ , is 400 nm and repeats 10 times for a total corrugated length of 4000 nm. Three pitches are shown: (a) 400 nm, (b) 600 nm, and (c) 800 nm.

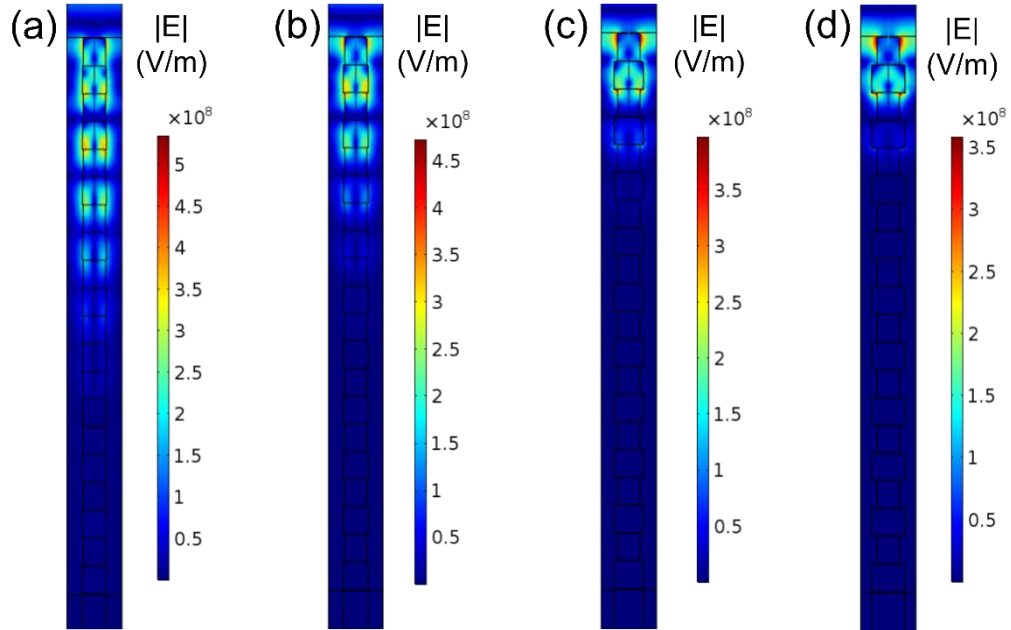


Figure 8.4. Electric field norm for NWs with $P = 400$ nm and wavelength corresponding to maximum reflectance λ_B as shown in Figure 8.3 (a). The corrugation depth is (a) 5 nm, (b) 10 nm, (c) 25 nm, and (d) 40 nm. The incident wavelength is (a) 805 nm, (b) 825 nm, (c) 865 nm, and (d) 900 nm.

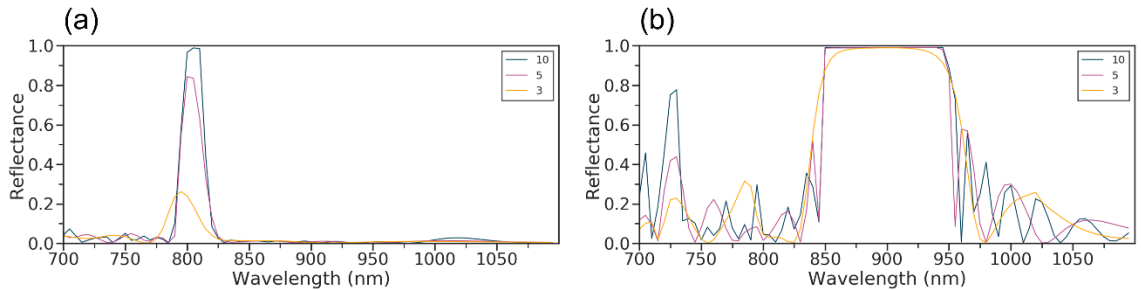


Figure 8.5. The reflectance spectra of a corrugated NW DBR with 3, 5, or 10 periods. The period length is $\Lambda = 400$ nm. The pitch is 400 nm and the corrugation depth is (a) 5 nm and (b) 40 nm.

With the change in corrugation depth, there is also a shift in the reflectance spectrum as shown in Figure 8.3. The red-shift in the peak wavelength can be attributed to an increase in the effective refractive index of the structure. Corrugation depth is increased by increasing the wide outer diameter d_2 of the NW, and a larger diameter increases the effective refractive index of the HE_{11} mode as shown in Figure 2.3.

In contrast, decreasing the pitch of the NW array causes a blue-shift in the peak reflected wavelength as shown in Figure 8.3 (a), (b) and (c). This can also be attributed to a change in the effective refractive index as the near-field coupling between NWs can decrease the local effective refractive index [8.28, 8.29].

According to Eq. (8.1), an increasing period should increase the Bragg wavelength. Figure 8.6 shows that a very sharp reflection peak occurs for $\Lambda = 700$ nm at a wavelength of 915 nm. Plotting the transverse field patterns with the field vectors for this case, as in Figure 8.7, shows that the field within the NW has HE_{11} character. Additionally, observing the field profiles in the yz plane indicates that the transverse field attenuates down the length of the NW as shown in Figure 8.8. Observing the periodicity of the mode in the NW shows that it repeats roughly every Λ which, according to Eq. (8.1), corresponds to $m = 2$, or the 2nd order Bragg grating. This indicates that for this wavelength and geometry the 2nd Bragg order dominates the reflectance.

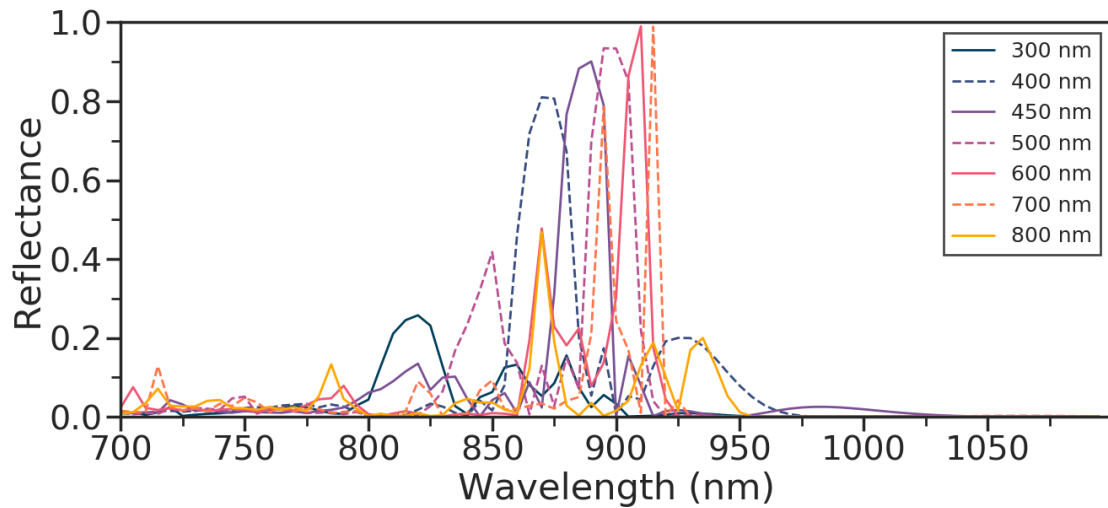


Figure 8.6. Reflectance spectrum for an array of corrugated NWs with 800 nm pitch, 165 nm inner diameter, and 5 nm corrugation depth. The period, Λ , of the corrugation is given in the legend.

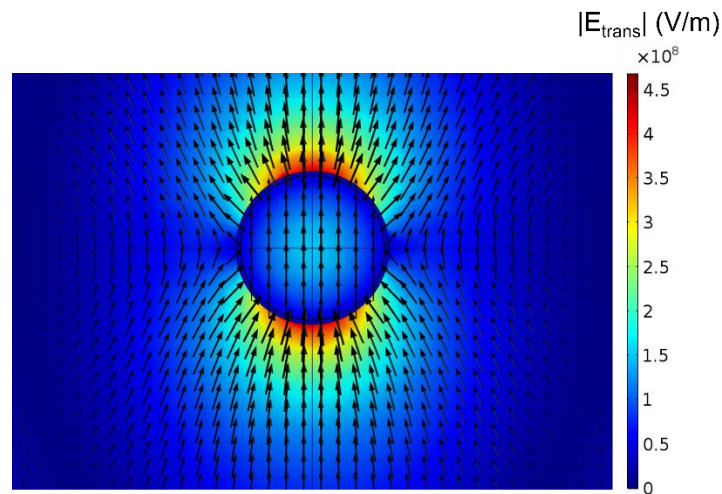


Figure 8.7. The transverse field in a corrugated NW at an incident wavelength of 915 nm with inner diameter $d_1 = 165$ nm, period $\Lambda = 700$ nm, and corrugation depth $h = 5$ nm. Field vectors correspond to the transverse field components E_x and E_y .

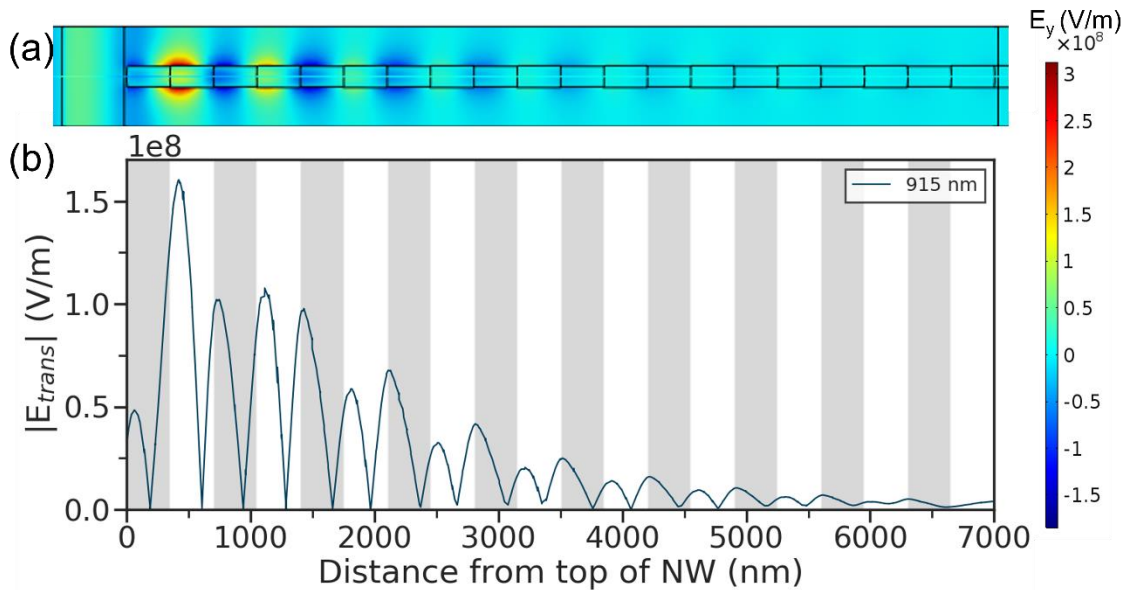


Figure 8.8. (a) The E_y field in the yz plane at an incident wavelength of 915 nm in a corrugated NW with $d_1 = 165$ nm, $\Lambda = 700$ nm, and $h = 5$ nm. (b) The norm of the transverse field down the centre line of the NW.

Lastly, throughout this section the absorptance within the NW has been “turned off” to observe the Bragg reflectance fully. However, wavelengths below the bandgap wavelength of GaAs will be affected by absorption as shown in Figure 8.9. This figure can be compared with Figure 8.3 (a) which shows the same reflectance spectra without absorptance. Below the band-edge, the NWs show a significant drop in reflectance since the light is absorbed before it can exit the end of the NW and contribute to reflection.

Several peaks below the band-edge are no longer visible, which further indicates that they were caused by interaction with the corrugated NW structure.

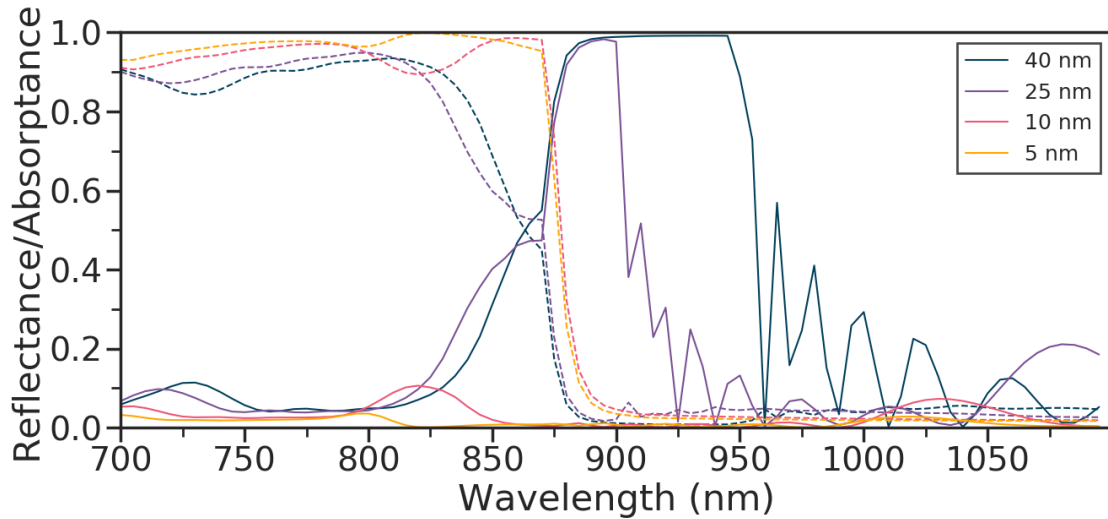


Figure 8.9. The reflectance (solid lines) and absorptance (dashed lines) spectra for corrugated NW arrays with a pitch of 400 nm, inner diameter of 165 nm, period Λ of 400 nm, 10 periods, and non-zero imaginary component of the complex refractive index. Corrugation depth is given in the legend.

8.5. Conclusions

The properties of corrugated NW DBRs were examined. Corrugated NWs show a significant increase in reflectance compared to cylindrical NWs with the same pitch and diameter. The peaks in the reflectance spectra can be controlled by adjusting the effective refractive index of the structure through changes to the diameter and pitch. Reflectance peaks shift to longer wavelengths with increasing diameter. Near-field coupling caused by

a decreasing pitch causes the reflectance peaks to shift to shorter wavelengths. Altering the DBR period causes shifts in accordance with the Bragg condition. Examining the field patterns within the NW shows that multiple peaks cannot be explained by the presence of multiple modes since only the HE_{11} mode is observed and the NWs are interpreted as being single-mode. The exact nature of each of the peaks will depend on coupling between forward and backward modes of the NW, neighbouring NWs, and possibly radiation modes, making NW DBRs a complicated physical problem with great potential for future studies.

8.6. References

- [8.1] H. M. Ng, D. Doppalapudi, E. Iliopoulos, and T. D. Moustakas, “Distributed Bragg reflectors based on AlN/GaN multilayers,” *Appl. Phys. Lett.*, vol. 74, no. 7, pp. 1036–1038, 1999.
- [8.2] L. Chen and E. Towe, “Nanowire lasers with distributed-Bragg-reflector mirrors,” *Appl. Phys. Lett.*, vol. 89, no. 5, 2006, Art. no. 053125.
- [8.3] J. Heo, Z. Zhou, W. Guo, B. S. Ooi, and P. Bhattacharya, “Characteristics of AlN/GaN nanowire Bragg mirror grown on (001) silicon by molecular beam epitaxy,” *Appl. Phys. Lett.*, vol. 103, no. 18, 2013, Art. no. 181102.
- [8.4] X. Zhang, H. Yang, Y. Zhang, and H. Liu, “Design of high-quality reflectors for vertical III-V nanowire lasers on Si,” *Nanotechnology*, vol. 33, no. 3, 2022, Art. no. 035202.

- [8.5] M. Aghaeipour and H. Pettersson, “Enhanced broadband absorption in nanowire arrays with integrated Bragg reflectors,” *Nanophotonics*, vol. 7, no. 5, pp. 819–825, 2018.
- [8.6] A. Fu, H. Gao, P. Petrov, and P. Yang, “Widely tunable distributed Bragg reflectors integrated into nanowire waveguides,” *Nano Lett.*, vol. 15, no. 10, pp. 6909–6913, 2015.
- [8.7] N. I. Goktas, P. Wilson, A. Ghukasyan, D. Wagner, S. McNamee, and R. LaPierre, “Nanowires for Energy: A Review,” *Appl. Phys. Rev.*, vol. 5, no. 4, 2018, Art. no. 041305.
- [8.8] R. R. LaPierre, M. Robson, K. M. Azizur-Rahman, and P. Kuyanov, “A review of III-V nanowire infrared photodetectors and sensors,” *J. Phys. D: Appl. Phys.*, vol. 50, no. 12, 2017, Art. no. 123001.
- [8.9] Y. Zhang, J. Wu, M. Aagesen, and H. Liu, “III–V nanowires and nanowire optoelectronic devices,” *J. Phys. D: Appl. Phys.*, vol. 48, no. 46, 2015, Art. no. 463001.
- [8.10] K. M. Azizur-Rahman and R. R. LaPierre, “Wavelength-selective absorptance in GaAs, InP and InAs nanowire arrays,” *Nanotechnology*, vol. 26, no. 29, 2015, Art. no. 295202.
- [8.11] P. C. McIntyre and A. Fontcuberta i Morral, “Semiconductor nanowires: to grow or not to grow?,” *Mater. Today Nano*, vol. 9, 2020, Art. no. 100058.
- [8.12] J. D. Christesen, C. W. Pinion, X. Zhang, J. R. McBride, and J. F. Cahoon, “Encoding abrupt and uniform dopant profiles in vapor-liquid-solid nanowires by

- suppressing the reservoir effect of the liquid catalyst,” *ACS Nano*, vol. 8, no. 11, pp. 11790–11798, 2014.
- [8.13] K. A. Dick, J. Bolinsson, B. M. Borg, and J. Johansson, “Controlling the abruptness of axial heterojunctions in III-V nanowires: Beyond the reservoir effect,” *Nano Lett.*, vol. 12, no. 6, pp. 3200–3206, 2012.
- [8.14] V. Zannier, F. Rossi, V. G. Dubrovskii, D. Ercolani, S. Battiato, and L. Sorba, “Nanoparticle stability in axial InAs-InP nanowire heterostructures with atomically sharp interfaces,” *Nano Lett.*, vol. 18, no. 1, pp. 167–174, 2018.
- [8.15] T. Frolov, W. C. Carter, and M. Asta, “Capillary instability in nanowire geometries,” *Nano Lett.*, vol. 14, no. 6, pp. 3577–3581, 2014.
- [8.16] D. P. Wilson, A. S. Sokolovskii, N. I. Goktas, V. G. Dubrovskii, and R. R. LaPierre, “Photovoltaic light funnels grown by GaAs nanowire droplet dynamics,” *IEEE J. Photovoltaics*, vol. 9, no. 5, pp. 1225–1231, 2019.
- [8.17] D. P. Wilson, A. S. Sokolovskii, R. R. LaPierre, F. Panciera, F. Glas, and V. G. Dubrovskii, “Modeling the dynamics of interface morphology and crystal phase change in self-catalyzed GaAs nanowires,” *Nanotechnology*, vol. 31, no. 48, 2020, Art. no. 485602.
- [8.18] W. Kim et al., “Bistability of Contact Angle and Its Role in Achieving Quantum-Thin Self-Assisted GaAs nanowires,” *Nano Lett.*, vol. 18, no. 1, pp. 49–57, 2018.
- [8.19] E. I. Givargizov, “Periodic instability in whisker growth,” *J. Cryst. Growth*, vol. 20, no. 3, pp. 217–226, 1973.

- [8.20] Z. Luo et al., “Atomic gold-enabled three-dimensional lithography for silicon mesostructures,” *Science* (80-.), vol. 348, no. 6242, pp. 1451–1455, 2015.
- [8.21] S. Kim and J. F. Cahoon, “Geometric nanophotonics: Light management in single nanowires through morphology,” *Acc. Chem. Res.*, vol. 52, no. 12, pp. 3511–3520, 2019.
- [8.22] N. Isik Goktas, A. Sokolovskii, V. G. Dubrovskii, and R. R. LaPierre, “Formation mechanism of twinning superlattices in doped GaAs nanowires,” *Nano Lett.*, vol. 20, no. 5, pp. 3344–3351, 2020.
- [8.23] B. Hua, J. Motohisa, Y. Ding, S. Hara, and T. Fukui, “Characterization of Fabry-Pérot microcavity modes in GaAs nanowires fabricated by selective-area metal organic vapor phase epitaxy,” *Appl. Phys. Lett.*, vol. 91, no. 13, 2007, Art. no. 131112.
- [8.24] P. E. Landreman, H. Chalabi, J. Park, and M. L. Brongersma, “Fabry-Perot description for Mie resonances of rectangular dielectric nanowire optical resonators,” *Opt. Express*, vol. 24, no. 26, 2016, Art. no. 29760.
- [8.25] D. Kwong et al., “Corrugated waveguide-based optical phased array with crosstalk suppression,” *IEEE Photonics Technol. Lett.*, vol. 26, no. 10, pp. 991–994, 2014.
- [8.26] E. D. Palik, *Handbook of Optical Constants of Solids*. Washington: Academic Press Inc., 1985.
- [8.27] D. Marcuse, *Theory of Dielectric Optical Waveguides*, 2nd ed. San Diego: Academic Press Inc., 1991.

- [8.28] B. C. P. Sturmberg et al., “Optimizing photovoltaic charge generation of nanowire arrays: A simple semi-analytic approach,” *ACS Photonics*, vol. 1, no. 8, pp. 683–689, 2014.
- [8.29] K. T. Fountaine, W. S. Whitney, and H. A. Atwater, “Resonant absorption in semiconductor nanowires and nanowire arrays: Relating leaky waveguide modes to Bloch photonic crystal modes,” *J. Appl. Phys.*, vol. 116, no. 15, 2014, Art. no. 153106.
- [8.30] B. C. P. Sturmberg et al., “Modal analysis of enhanced absorption in silicon nanowire arrays,” *Opt. Express*, vol. 19, no. S5, pp. A1067–A1081, 2011.

9. Conclusions and Future Work

9.1. Thesis Summary

This thesis examined the droplet dynamics of self-catalyzed GaAs NWs and its effect on NW yield and diameter as well as applications in photovoltaics and novel NW structures such as corrugated NW DBRs.

The impact of a Ga pre-deposition stage at the beginning of growth was first examined and the following conclusions were drawn:

- a) Self-catalyzed GaAs NWs were grown by MBE. The substrate was prepared by growing a SiO_x layer on a Si(111) substrate and then patterning it using EBL and etching holes in the oxide layer using RIE. A pre-deposition step is effective for increasing the NW yield. Yield was increased to nearly 100% with a pre-deposition time of 250 s. The effect of the pre-deposition on the overall yield was dependent on the diameter of the holes etched in the Si oxide layer.
- b) The optimal volume of the Ga droplet is equal to the volume of the hole itself, but the collection of this Ga in the holes can be impeded by some remaining oxide in the holes. A mathematical model shows that this nucleation suppression in smaller holes requires longer pre-deposition times than in the larger holes, which can account for the difference between the yields with different hole diameters.
- c) Pre-deposition alone has no influence on the diameter of the resulting NWs. Radial growth of GaAs occurs by the VS mechanism. This radial growth was observed by

TEM where a radial GaAs layer can be observed surrounding GaAsP marker layers in the NW core.

It is important to understand the nature of self-catalyzed NW growth as it relates to the NW diameter. A mathematical model was developed and fit to experimental data collected by in-situ TEM during MBE growth. The study resulted in the following:

- a) NW diameter is dependent on the volume of the droplet on top of the NW. The droplet volume changes with the collection of group III and V adatoms from the direct flux provided from the MBE system as well as by diffusion along the sidewalls of the NW. The droplet may also lose adatoms by diffusion.
- b) The contact angle, β , of the droplet on top of the NW determines the nature of the faceting as new layers grow. NWs form narrowing facets for $\beta \leq 100^\circ$ and widening facets for $\beta \geq 137^\circ$. The contact angle can also be used to determine the crystal phase of the NW which is WZ for $100^\circ < \beta < 125^\circ$ and is ZB otherwise.
- c) The mathematical model was fit to experimental data of NW radius and contact angle and reasonable agreement was achieved between the two. This model could be used to design NWs where both crystal phase and diameter are important.

Control of the NW diameter was shown by adjusting the flux of group III and V materials experimentally. Inverse conical NWs were produced with a large top and small base. The following conclusions were drawn:

- a) Control over the NW diameter was demonstrated. The inverted conical design of the NW allowed for large diameters at the top of the NW. These large diameters are needed for optimal absorption of the AM1.5D solar spectrum for photovoltaic

applications. By allowing the base to be narrower, high yields can be obtained using the pre-deposition techniques described earlier.

- b) A model was developed to describe the diameter evolution of the NW as the V/III flux ratio was altered. This model varied slightly from the one presented earlier. While it still considered the droplet volume, it assumed a constant contact angle. The model was able to show the increase in NW diameter as the V/III flux ratio was reduced due to inflation of the Ga droplet. This model could be useful for NW design where the contact angle and crystal phase are less important.
- c) Optical simulations were performed using COMSOL Multiphysics and the RF module. An optimized array of NWs with vertical sidewalls was compared to an array of linearly tapered inverse conical NWs. The optimized straight NW array and the inverse conical array showed similar photocurrent with a difference of 0.9 mAcm^{-2} between the two. This suggests that the inverted conical NW design is a good choice for NW photovoltaic applications.

To expand on the use of linearly tapering the NW sidewalls for photovoltaic applications, further simulations were performed. The following conclusions were drawn:

- a) A range of NW morphologies were simulated including conical, straight, and inverse conical NWs. The photocurrent under the AM1.5D solar spectrum were calculated for each, as well as the reflectance, transmittance and absorptance coefficients. Both the HE_{11} and the HE_{12} modes were found to be supported in these conical structures and demonstrated through transverse field patterns. The NW was

broken into segments to show explicitly where absorption was occurring within the NW.

- b) Conical NWs were shown to have superior anti-reflection properties; however, when top diameters were properly optimized, both NW morphologies (conical and inverse conical) performed equally well in terms of the photocurrent produced.

Finally, another application of self-catalyzed NW droplet dynamics was examined. This study examined periodic modulation of the NW diameter (corrugated NWs) and its impact on the optical reflectance. The following conclusions were drawn:

- a) Periodic corrugated NW arrays show a significant increase in reflectance over non-corrugated NWs. The NW arrays behave like a Bragg reflector. The Bragg peak can be shifted by adjusting any of the following: the corrugation period, the NW diameter, or the array pitch. The shift occurred due to a change in the effective refractive index of the NW.
- b) Corrugated NW structures represent an emerging type of NW and suggested applications include vertical cavity surface emitting lasers (VCSELs).

9.2. Future Work

9.2.1. Conical NW Photovoltaics

Future work on NWs for photovoltaic applications should focus on the incorporation of dopants into the NW to create p-n junctions. Further simulations could be of benefit to determine the dopant concentration and NW dimensions needed to achieve

optimal device performance. The parameters will be dependent on the diameter of the NW and will change based on the degree of tapering. Similar simulations have been performed, and models using COMSOL's semiconductor module already exist and could be applied to this problem [9.1]. The simulation work would be greatly enhanced by comparison with fabricated devices, which will present their own set of challenges.

The NWs will also need to be passivated due to the high surface recombination velocity of GaAs. Passivation on tapered GaAs NWs has been accomplished by growing an AlGaAs shell by VS growth. A comparison of tapered NWs without a passivating shell and with a passivating shell are shown in Figure 9.1. The thickness will need to be determined, particularly due to the influence of shadowing by neighboring NWs, which can result in a thinner passivation layer near the base of the NW and a larger layer near the top [9.2]. The impact of this shadowing may increase due to the inversely tapered nature of the NWs.

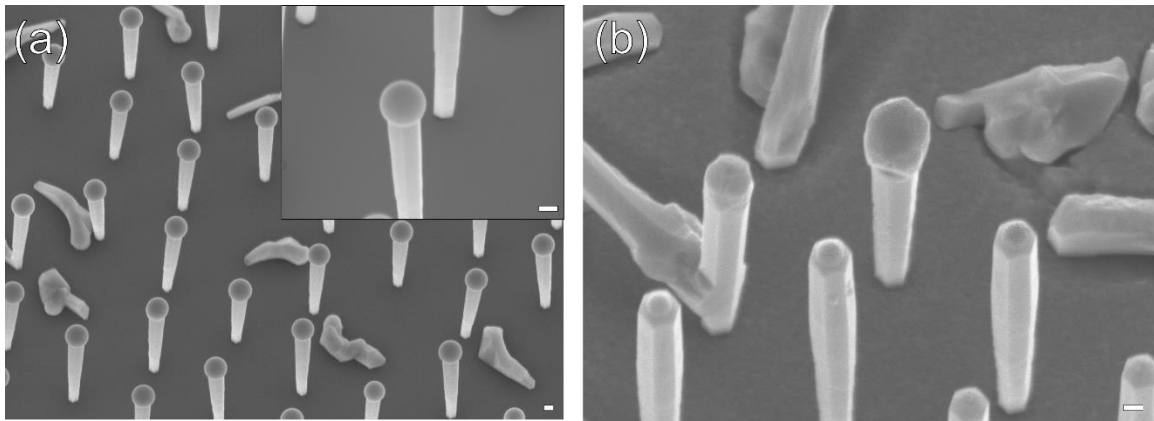


Figure 9.1. (a) 20° tilted SEM images of tapered NW arrays grown without a shell layer. Inset shows a higher magnification and is tilted 30°. (b) 20° tilted SEM images of NW arrays grown with the same core parameters as (a) but with the addition of 15 min of VS

$\text{Al}_{0.8}\text{Ga}_{0.2}\text{As}$ shell growth after the core has been grown. Pitch is 1000 nm. Scale bars are 100 nm.

One interesting question is whether altering the NW geometry during growth could be used to produce multi-junction NW solar cells. As shown previously, absorption in NWs is dependent on the wavelength and the diameter of the NW. Multi-junction cells increase broadband absorption across the entire solar spectrum. Wide bandgap materials are placed on top to absorb the shortest wavelengths of light followed by smaller bandgap materials to progressively absorb the longer wavelengths. In a NW multi-junction cell, the absorption in each material will be optimized by a certain diameter and morphology [9.3]. Multi-junction NW solar cells can be difficult to test since they are current-limited by the worst performing junction. Good control of a single p-n junction NW solar cell should be accomplished first.

9.2.2. NW Modelling and Databases

Two models for NW diameter evolution during MBE growth were presented in this thesis. In conjunction with a well-kept database of NW diameters and MBE growth parameters, these models could be used to decide the parameters required for future NW growths using numerical regression techniques. This could take some of the trial and error out of NW growths, particularly if a complicated or exact geometry is needed (for example a periodically corrugated NW of a specific inner and outer diameter.) If only the diameter is important, the simple model presented in Chapter 6 could be sufficient. If knowledge of the contact angle and crystal phase is needed, then the model presented in Chapter 5 could

be used. Since our MBE system does not have the ability to measure the contact angle throughout the growth, one would be limited to the angle the droplet possesses at the end of growth. The equations could still be solved with this information.

9.2.3. Corrugated NWs for DBRs, FP Cavities, and VCSELs

Chapter 8 introduced corrugated NW arrays that act as distributed Bragg reflectors. This section has significant potential for new work. While the reflectance of these structures is impressive in simulations, they have not been fabricated and demonstrated yet.

The fabrication of corrugated NW structures presents numerous challenges. The fabrication of the corrugations can be achieved in two different ways. Droplet dynamics can be used as described in this thesis, changing the diameter periodically through adjusting the V/III ratio during MBE growth. Alternatively, the diameter can be controlled by introducing twinning superlattices which requires the introduction of dopants into the droplet [9.4]. In either case, the NWs will have to be evaluated for consistency of the periodic layers. The number of corrugations needed and the corrugation depth which can be achievably fabricated will also need to be determined.

Once control over the periodic structures has been demonstrated to create reproducible DBRs, this base structure can be built upon. A Fabry-Perot cavity can be placed between two DBRs at the base and top of the NW to create a laser cavity [9.5]. Other gain materials could also be introduced to this cavity; for example, quantum dots may also be an interesting avenue to explore [9.6]. While VCSELs are one possible

application for this structure, another could be sensors since both temperature and strain can affect the position of the Bragg peak of the DBR [9.7].

9.3. References

- [9.1] D. L. Wagner, D. R. Novog, and R. R. LaPierre, “Genetic Algorithm Optimization of Core-Shell Nanowire Betavoltaic Generators,” *Nanotechnology*, vol. 31, no. 45, 2020, Art. no. 455403.
- [9.2] J. P. Boulanger et al., “Characterization of a Ga-Assisted GaAs Nanowire Array Solar Cell on Si Substrate,” *IEEE J. Photovoltaics*, vol. 6, no. 3, pp. 661–667, 2016.
- [9.3] Y. Chen, M.-E. Pistol, and N. Anttu, “Design for strong absorption in a nanowire array tandem solar cell,” *Sci. Rep.*, vol. 6, 2016, Art. no. 32349.
- [9.4] N. Isik Goktas, A. Sokolovskii, V. G. Dubrovskii, and R. R. LaPierre, “Formation mechanism of twinning superlattices in doped GaAs nanowires,” *Nano Lett.*, vol. 20, no. 5, pp. 3344–3351, 2020.
- [9.5] C. Couteau, A. Larrue, C. Wilhelm, and C. Soci, “Nanowire lasers,” *Nanophotonics*, vol. 4, no. 1, pp. 90–107, 2015.
- [9.6] P. Kuyanov, S. A. McNamee, and R. R. LaPierre, “GaAs quantum dots in a GaP nanowire photodetector,” *Nanotechnology*, vol. 29, no. 12, 2018, Art. no. 124003.
- [9.7] B. Lee, “Review of the present status of optical fiber sensors,” *Opt. Fiber Technol.*, vol. 9, no. 2, pp. 57–79, 2003.

10. Appendix

10.1. Setting Up COMSOL 5.3A Optical Models for Periodic NW Arrays

This section details how to set up the optical simulations in COMSOL Multiphysics 5.3A. It does not give a “recipe” but a general set of steps and explanations that should allow future models to be created and understood. This model is similar to that developed in [10.1]. The following details how to create and run the model (with some tips) using the COMSOL GUI:

- 1) **Create a new model.** When COMSOL opens choose “Model Wizard”, select 3D space dimensions. From the physics interfaces, add “Electromagnetic Waves, Frequency Domain” from under the Radio Frequency option. Select the “Frequency Domain” study.
- 2) **Add parameters.** Right click on “Global Definitions” and add a “Parameters” tab. This allows you set variable names and values that can be called throughout the rest of the model. Some examples of parameters that might be useful include P, pitch; D (or R), diameter (or radius); and L, NW length. These are mainly used for defining the geometry, so that changes to the geometry can be made quickly and easily.
- 3) **Import the refractive indices.** Expand the “Components” tab and right click on “Definitions.” Add an interpolation function. Under Data Source select “File” to import a file containing the refractive indices at different wavelengths. The number of arguments is set to 1. This is the number of independent arguments in the file and is usually either the frequency or the wavelength. The independent arguments should be

the first columns in the file. In the “Functions” table give each of the dependent arguments names. These are callable (for example as: $n_{\text{GaAs}}(\text{wavelength})$) at other points in the setup. The position in the file specifies which columns after the independent argument’s columns the function values are in (usually 1, or 1 and 2 if you have both n and k data in the same file). Under interpolation, “piecewise cubic” is a good choice. Set the extrapolation to “constant” or “specific value”, which allows you to choose a constant value. The extrapolation will only matter if you are solving outside of the range of the interpolation data. If you need to solve outside this range, then you will have to choose the extrapolation more carefully. Under “Units”, give the units of the independent arguments and the functions (for example: “m” for meters and “1” for the unitless refractive index). If you have more than one function in the file, comma separate the units for each one.

- a) **Refractive index files.** Some of these refractive index files are already saved and can be found in the “.../Optical_Simulations_FEM/n_k_vals/” folder. This data largely comes from [10.2], although a few other sources have also been acquired. It is good practice to include the author of the data or reference in the file name.
- 4) **Build the geometry.** Right click on “Geometry” to see a number of built-in shapes that can be used to build the desired simulation domain. Fill in the details using the Parameters defined earlier. An example of a final geometry is shown in Figure 10.1 (a).
 - a) **Tapered NWs.** To create a smoothly varying NW sidewall, create an extrusion. Right click “Geometry” and select “Work Plane.” Choose the xy plane type and set the z-coordinate so that it is built at the top of the substrate’s geometry. Expand the

work plane tab and right click on “Plane Geometry.” Define a circle at the centre of the work plane. This is the base of your NW. Right click on Work Plane and add an “Extrusion.” Select “Extrude from” and choose “Work Plane.” Under “Distances” specify “Distance from plane” and input the length of the extruded section. Under “Scales” input the scaling of the shape that will be performed in the x (“Scales xw”) and y (“Scales yw”) directions. Use the ratio of the radius at the top of the NW to the radius at the bottom of the NW for each.

- i) **Extruding from a face.** If you want to create an extrusion in multiple stages you can extrude from the face of a previous section rather than the original work plane. Under “Extrude From”, select “Faces”. Make sure the Input Faces is set to “Active” and select the face you want to extrude. Proceed as before.
- b) **Periodic NWs with abrupt changes in diameter.** To create very long periodic NWs, it is best to create an array. Start off by creating the basic unit cell of the period section. This will look like two cylinders stacked on top of each other with different diameters. Right click on “Geometry”, go to “Transforms” and select “Array.” Activate the “Input Objects” box and select the geometry you want to duplicate (the two cylinders). Under “Size”, select “Linear” array type. This will duplicate the objects along a single axis. In “Size”, write the number of periods you want (≥ 2). Under “Displacements”, indicate how far away you want the next period to be created. To create a single NW object along the \hat{z} -direction with no space in between segments, set “z” to the height of the two original cylinders.

- 5) **Defining the physics.** Click on the “Electromagnetic Waves, Frequency Domain” tab and set the formulation to “Full Field.” Expand this tab. By default it already has some conditions defined. These can be changed or overwritten by adding new definitions. The original tabs can’t be deleted.
- a) **Domains.** A “Wave Equation, Electric” is needed for each material. Activate the “Domain Selection” and choose all geometric entities corresponding to a certain material (i.e. select all of the substrate, NW, or surrounding air.) Under “Electric Displacement Field Model” choose “Refractive Index.” For the real and imaginary parts of the refractive index, choose “User Defined” and input the value directly (example: set n : 1 and k : 0 for air) or by calling a function defined earlier.
- i) **Calling functions.** To call the wavelength dependent values of the refractive index defined in (3), write the function name followed by the argument in round brackets. The argument in the round brackets should correspond to the frequency of the solver. The built-in call for this value is “`emw.freq`”. The frequency solver only takes value in Hz, so if the argument is expected in meters convert the frequency using the built-in “`c_const`” (i.e. `n_GaAs(c_const/emw.freq)`.)
- b) **Perfectly matched layers.** PMLs are placed at the top and bottom of the geometry to reduce reflection at the top and bottom boundaries. Go back to the “Definitions” tab. Right click and add a “Perfectly Matched Layer.” PMLs that are separated in space and do not touch need their own tab. A separate tab should be created for domains that correspond to a different material (such as if you had a NW without a

substrate that needed to be backed by a PML). Select “Cartesian” under Geometry type.

- c) **Port boundary.** Right click the Frequency Domain tab and add a “Port” boundary condition. This will be used to simulate an incident E-field on our NW array. The first port created will have the name set as “1”. Do not change this as it must be a number and is used for calculations of S-parameters. Under type of port, choose “Periodic” and set the “Wave excitation at this port” to On. You can also set up Ports with the condition set to Off. These are known as listening ports and are useful for S-parameter calculations. The port input power defines the power of the light coming from the port. For general simulations this might be set to 1[W] (units are specified using square brackets). For simulations weighted to the solar spectrum see the note below this. Check the box to “Activate slit condition on interior port” and a normal vector will appear pointing in the positive z-direction. Choose a “Domain backed” slit type because of the PML layer used as backing and “Reverse” port orientation since you want power to be incident in the opposite direction to that normal vector (i.e., downwards onto the NW.) Under the Port Mode Settings, define the incident electric field by defining the x, y, and z components of E_0 . For a y-polarized plane wave type “1” into the y-component. Keep the elevation angle and azimuth angle set to 0 unless you want to change the angle of the incident light.
- i) **Weighting incident power to the solar spectrum.** To weight the port based on the incident frequency, create a function under the Definitions tab as in (3). The AM1.5D solar spectrum from NREL [10.3] is given as solar irradiance in

$\text{Wm}^{-2}\text{nm}^{-1}$. A power in W is required for the port boundary. The total power density of the AM1.5D spectrum is 900 Wm^{-2} when integrated. When performing a sweep a discrete number of wavelengths are solved for. Since we would still like to account for all the power for each of the steps we integrate the solar irradiance over a small region with the wavelength we will solve for at the centre. This assigns a power density to each wavelength step. Call the power density function in the P_{in} box (i.e. `pow_dens(c_const/freq)`) and multiply by the area of the port to define the quantity in W instead of Wm^{-2} . The Python program used to create the integrated power densities is in Section 10.3

- d) **Periodic boundaries.** The NW array is periodic in x and y. Add four “Periodic Conditions:”, two for x and y in the PML layers and two for x and y in the normal domain. Activate the “Boundary Selection” and select all boundaries along one side of the domain as well as the opposing faces. The source (“src”) and destination (“dst”) faces which controls the mapping from one face to the other are assigned automatically. Under “Periodicity Settings” choose “Floquet periodicity” for the type and “From periodic port” for the k-vector. Do the same for the all the other Periodic Conditions.
- e) **Remaining Boundaries.** All that remains is the boundaries at the top and bottom of the domain which are normally assigned PML domains. These likely have the default Perfect Electric Conductor (PEC) boundary still attached. It is fine to leave it this way.

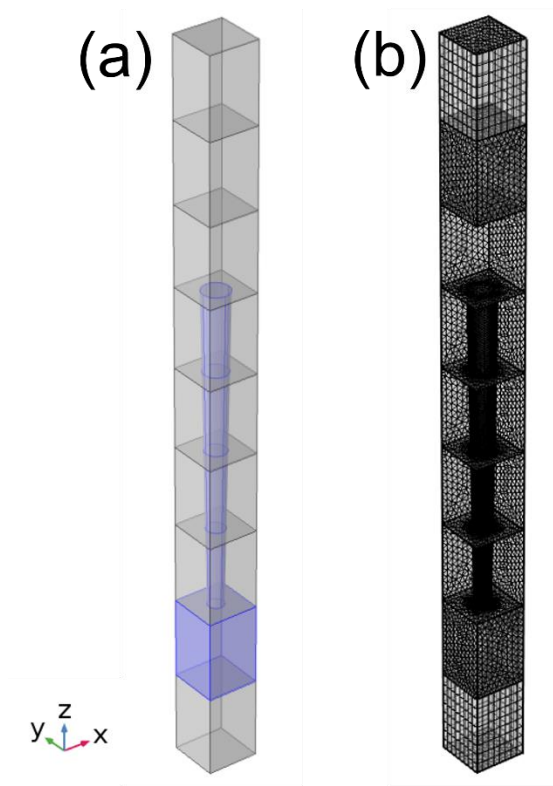


Figure 10.1. The (a) unit cell geometry and (b) mesh used to simulate an array of tapered NWs in COMSOL Multiphysics 5.3A. The NW and substrate have been highlighted in (a). Certain faces have been hidden in (b) in order to see the dense mesh on the NW domain more clearly.

- f) **Initial conditions.** The initial conditions set the values for the electric field to 0 by default. It is fine to leave it this way. Defining it based on the field generated from the periodic port would also be an acceptable choice but is not necessary.
- 7) **Mesh.** Meshing is particularly important for the FEM. Click on “Mesh” and “Build All.” A default mesh will be generated which include tetrahedral elements on the NW

domain, mapped elements on the periodic boundary conditions, and swept elements in the PML layers. It will resemble Figure 10.1 and should suffice for most purposes.

- a) **Mesh fineness.** Computation increases quickly with the number of degrees of freedom which increases with the number of elements. However, the mesh must be fine enough to produce an accurate solution. A convergence test should be done to ensure the mesh is fine enough by comparing the solution at the shortest wavelength you want to simulate for several meshes of increasing fineness to make sure the solution does not change. The rule of thumb for maximum mesh element size is at least $0.2 \times \textit{shortest wavelength}$. I suggest a maximum element size of 42 nm and a minimum element size of 0.9 nm. For larger geometries where the computation time becomes too long, the mesh can be increased slowly by increasing the max element size and growth rate in regions where you don't expect much variation in electric field.
- 8) **Solver.** Expand the “Study” tab. In “Step 1: Frequency Domain” input the unit of frequency that will be used (ex. Hz, THz). Type in the frequencies you want to solve for into the “Frequencies” field or import them from a file. Click “Compute” to run the simulation! (See (8a) before you start.)
- 9) **Results.** Some results such as graphs of the electric field will be generated automatically. Add more graphs by right clicking the “Results” tab. Create subsections of the data by right clicking “Data Sets.”
 - a) **Probes.** Probes can be set on boundaries, domains, or even globally and are automatically updated as the solver runs.

- i) **Reflectance and transmittance.** Go back to the “Definitions” tab. Right click and add a “Boundary Probe”. The variable name of the probe can be called in other probes. Set the probe type to “Integral.” Make sure the Source Selection is Active and choose the boundary (above the NW for reflectance and below the NW for transmittance). Type “ emw.nPoav ” into the “Expression” field to perform the integration over the time averaged power flow through the boundary.
- ii) **Absorption.** Add a “Global Variable Probe”. In the expression field write “1-R-T” where R and T refer back to variable names for the Boundary Probes for the reflectance and transmittance.
- iii) **Photocurrent.** If the simulation has been weighted to the solar spectrum, then add a “Domain Probe” to calculate it. Again, select “Integral” as the type and select the appropriate domains. To calculate the photocurrent in a GaAs NW, in the expression field write: “ $\text{e_const}*\text{epsilon0_const}*\text{emw.normE}^2*\text{n_GaAs}(\text{freq})*\text{k_GaAs}(\text{freq})/\text{hbar_const}/\text{area}$ ”.
- In this expression the “_const” are built in and n_GaAs and k_GaAs are the refractive index functions defined as (3), and area is the area of the port. Double check “Table and plot unit”. It should read A/m^2 .

10.2. Setting up a batch file

To speed up the process, model files can be solved continuously, one after another by using a batch file. Before saving and exiting the GUI, right click on “Get Initial Condition.” This will create results for the initial condition and will make the final results immediately available after you finish running the batch file and open up the GUI again. For some basics of batch files, refer to Ref. [10.4]. For a list of batch commands, refer to the COMSOL Multiphysics Reference Manual. On Linux, create a new text file and write: “comsol batch -inputfile input_file_name.mph -outputfile output_file_name.mph -study std1 -batchlog logfile_name.log”

Write one of these lines for each of the input files you want to solve. The input file will remain unchanged from when you started. The output file will contain your results. The logfile is updated throughout the simulation and can be opened to check progress.

Save the file as a .sh or shell file. You then need to make it executable. Open a terminal and run the command: `chmod +x filename.sh`. You should now be able to run the shell file from the terminal.

10.3. Setting power

To perform the integration of the solar irradiance as described in Chapter 10.1 section

(c)(i):

```

1. import pandas as pd
2. import numpy as np
3. from scipy import interpolate, integrate
4.
5. ### Import spectra and wavelengths -----
6.
7. excelfile = 'C:/Users/dpaig/Documents/COMSOL/astmg173.xls'
8. spectra = pd.read_excel(excelfile, header = 1)
9.
10. ## Linear Interpolation -----
11.
12. x = np.arange(280, 4000.5, 0.5)          # 0.5 nm spacing
13.
14. AM_D = interpolate.interp1d(spectra['Wvlngth nm'], spectra['Direct+circumsolar W*m-
    2*nm-1']) # spectral irradiance in [W m^-2 nm^-1]
15.
16. ### Integration around given points -----
17.
18. wavelength = np.arange(285, 1110, 10)   # List of wavelengths in steps of 10 nm
19. dl = 5                                   # 5 nm to be taken on either side
20. power_dens = np.ones(len(wavelength))   # power density in [W/m^2]
21.
22. for i in range(len(wavelength)):
23.     power_dens[i] = integrate.quad(AM_D, wavelength[i] - dl, wavelength[i] + dl)[0]

```

10.4. References

- [10.1] K. M. Azizur-Rahman, “Simulation of III-V nanowires for infrared photodetection,” McMaster University, 2016.
- [10.2] E. D. Palik, Handbook of Optical Constants of Solids. Washington: Academic Press Inc., 1985.

- [10.3] National Renewable Energy Laboratory (NREL), “Reference Air Mass 1.5 Spectra.” [Online]. Available: <https://www.nrel.gov/grid/solar-resource/spectra-am1.5.html>. [Accessed: 01-Jan-2021].
- [10.4] J. Hiller, “How to run simulations in batch mode from the command line,” COMSOL Blog, 2016. [Online]. Available: <https://www.comsol.com/blogs/how-to-run-simulations-in-batch-mode-from-the-command-line/>. [Accessed: 08-Apr-2022].